2015

III-V Nitride Based Microcantilever Heaters for Unique Multimodal Detection of Volatile Organic Compounds at Low Temperature

Ifat Jahangir
University of South Carolina

III-V Nitride based microcantilever heaters for unique multimodal detection of volatile organic compounds at low temperature

by

Ifat Jahangir

Bachelor of Science in Engineering
Bangladesh University of Engineering and Technology, 2011

Submitted in Partial Fulfillment of the Requirements

For the Degree of Master of Science in

Electrical Engineering

College of Engineering and Computing

University of South Carolina

2015

Accepted by:

Goutam Koley, Director of Thesis

MVS Chandrashekhar, Reader

Lacy Ford, Senior Vice Provost and Dean of Graduate Studies

Dedication

To my parents Sayeda Sultana and Sikder Jahangir Rashid

Acknowledgements

I would like to thank my Supervisor Dr. Goutam Koley for supporting me during these three years. Working with Dr. Koley, in my opinion, is the best thing that a MS student can wish for. He perfectly translates the character of his students and provides the best conditions for the development of intellectual qualities and creative thinking. I am very grateful to him for his scientific advice and knowledge and many insightful discussions and suggestions he provided me and beyond all his guidance in my tough times.

I owe my gratitude to Dr. MVS Chandrashekhar, member of my thesis defense committee, for his guidance and support during the last one year. Although I am currently a PhD student in his group working in a different area, he still managed time to help me with my MS research project whenever needed.

The Microfabrication part was done using the class 10/100 cleanroom facilities at the IEN at Georgia Institute of Technology. I worked there from April to July, 2014 and met really nice, helpful and knowledgable people and stuff. I would like to express my gratitude to Prof. David Gottfried, Dr. Gary Spinner, Dr. Mikkel Thomas, Thomas Johnson Averette, Charlie Suh, Charlie Turgeon and Tran-Vinh Nguyen for their help in troubleshooting various problems that I faced there.

I would like to acknowledge the financial support from NSF grant that funded part of the research for this thesis. I thank to all the present members of Dr. Koley's group. I would like to thank Dr. Abdul Hafiz Ibne Talukdar and his wife Dr. Mahbuba

Sultana specially, for their help with fabrication. Hafiz and I worked together in IEN facilities and shared a process flow that we both developed during our stay there. Without his direct help and the guidance from his wife, who had great experience in III-V Nitride device fabrication, it would not be possible to complete the mammoth task that I took on. I would also like to thank our alumni Dr. Ehtesham Bin Quddus, Dr. Md. Qazi, Dr. Md. Waliullah Khan Nomani and Dr. Jie Liu for sharing their valuable experience of working in IEN with me to make better devices than the previous attempts. I would also like to thank Dr. Amol Singh, Dr. Md. Ahsan Uddin, Dr. Yihao Zhu, Dr. Alina Wilson, Nick DeRoller, Rina Patel and James Tolson for their constant support throughout the last three years.

I wish to express my heartfelt gratitude to my family – my parents and my brother, for always having faith in me and for bringing me this far. I would also like to thank all my friends who were very supportive during the entire duration of my stay here in Columbia, South Carolina. Finally and most importantly, I would like to express my deep gratitude towoards the Almighty for giving me the ability to finish this work smoothly, I could not have achieved anything without His blessings.

Abstract

Detection of volatile organic compounds (VOCs), which are widely used in industrial processes and household products, is very important due to significant health hazards associated with them. VOCs are commonly detected using photo-ionization detectors (PIDs), suspended hot bead pellistors, or heated metal oxide semiconductor functionalization layers. However, these techniques used for detecting VOCs often suffer from one or more of the following issues - high power consumption, limited selectivity, complicated functionalization technique and expensive characterization tools. On the other hand, microcantilevers offer excellent avenues for molecular sensing that arises out of their high sensitivity to various physical parameter changes induced by the analyte molecules. Microcantilever heaters, which are extremely sensitive to changes in thermal parameters, have been widely utilized for calorimetry, thermal nanotopography and thermal conductivity measurements. Due to the small area of the microcantilever that needs to be heated (i.e. the tip of a triangular microcantilever), they also offer the possibility of reduced power consumption for high temperature operation. The present study reports the multimodal VOC detection capability of unfunctionalized microcantilever heaters made of AlGaN/GaN heterostructure, which can address many of the limitations observed in other techniques.

The microcantilevers, fabricated on an AlGaN/GaN on Si wafer, were found to be excellent heating elements with high degree of localization and low power consumption (<1 mW for a temperature as high as 700 K). While most of the microcantilevers had a

single conducting channel along the arms, some were specially designed to have two parallel channels, isolated by semi-insulating GaN or air. The single channel microcantilevers exhibited a dc response to different VOCs above particular threshold voltages, which were found out to be strongly correlated to the latent heat of evaporation for those analytes. At a constant dc bias which is above that threshold voltage, the magnitude of the response for any VOC is a function of concentration and molecular dipole moment of the VOC, which is another metric that can be easily determined and calibrated. While threshold voltage is a reliable indicator for uniquely identifying a VOC, the response magnitude can be used to estimate the concentration of the analyte also, down to low ppm range with a response time less than 40 s. The microcantilevers with two parallel channels are suitable for thermal conductivity based detection of any vapor or gas, therefore it helps pinpointing the VOCs even better in an event where two different VOCs have very close threshold voltages but significantly different thermal conductivities. A numerical model, based on three dimensional heat transfer and Joule heating equations, has also been developed for these microcantilevers. This model has been employed to explain the physical phenomena associated with the sensor under different bias conditions, and also to predict the response time of the heater alone, which is much smaller than the response time of the overall system. The noise limited resolution from the theoretical model is in the range of parts per billion and shows excellent promise for the future application of this kind of sensor in detecting VOCs with very low power consumption.

Table of Contents

List of Figures

List of Tables

Chapter 1

Introduction

1.1 Overview

Detection of small quantities of molecules is of significant interest for numerous numbers of applications, ranging from gas sensing and environmental monitoring to biological and medical diagnostics. These require the sensors to be inexpensive, power efficient, easily deployable and miniaturized, yet sensitive enough to detect molecules down to the single-molecule level. With the advancement of miniaturization technologies molecular sensors are getting smaller and smaller in dimensions. Miniaturization is also essential for *in vivo* physiological monitoring, sensor portability and minimized sample volumes. Conventional molecular sensors suffer from extensive packaging, complex electronic interfacing and regular maintenance, the use of novel Microlectromechanical systems (MEMS) devices that integrate electronics and micro-mechanical structures on chip could address all those drawbacks.

Microcantilevers are the most simplified MEMS based devices. Diverse applications of microcantilevers in the field of sensors have been explored by many researchers. These sensors have several advantages over the conventional techniques in terms of high sensitivity, low cost, simple procedure, non-hazardous procedures and quick response. A molecular sensor is usually evaluated with respect to three major aspects: 1) sensitivity, 2) selectivity, and 3) miniaturization. An ideal sensor should have

high sensitivity towards targeting chemicals, excellent selectivity to a specific signal of interest, and a very small dimension.

In this work we are proposing molecular sensors that will be made of novel V-shaped micro-cantilevers, in the form of arrays in a chip. Due to their reduced dimension, many of the individual cantilevers can be integrated together in a chip, thus the final device is ***miniaturized***.

Particles that are smaller than the characteristic lengths associated with the specific phenomena often display new chemistry and new physics that lead to new properties that depend on size. The analyte molecules and the sensing elements are of comparable size for microcantilever based sensing which promotes better sensitivity. Again in the case of nanoscale sensors the size of the structure is reduced further, surface to volume ratio increases considerably and the surface phenomena predominate over the chemistry and physics in the bulk. This enhances the ***sensitivity*** even more since the molecular interaction or sensing occurs at the surface.

The careful selection of superior material quality confirms the fast response. ***AlGaN/GaN heterostructures*** contain a highly conductive two-dimensional electron gas (2DEG) at the interface, which is sensitive to mechanical load, as well as to chemical modification of the surface, and can be used for novel sensing principles and as transducers for MEMS applications. The ***selectivity*** of the sensor is improved by the ***multimodal detection*** technique apart from the nature of the gas molecules themselves. In multimodal detection technique independent parameters can be independently measured and while they are combined together a unique signature for any particular molecule is obtained.

1.2 Chemical sensor arrays

A chemical sensor is a device that transforms chemical information, ranging from the concentration of a specific sample component to total composition analysis, into an analytically useful signal. The chemical information, mentioned above, may originate from a chemical reaction of the analyte or from a physical property of the system investigated.

A physical sensor is a device that provides information about a physical property of the system. A chemical sensor is an essential component of an ***analyzer.*** In addition to the sensor, the analyzer may contain devices that perform the following functions: sampling, sample transport, signal processing, data processing. An analyzer may be an essential part of an automated system. The analyzer working according to a sampling plan as a function of time acts as a monitor.

Chemical sensors contain two basic functional units: a receptor part and a transducer part. Some sensors may include a separator which is, for example, a membrane. In the ***recepror*** part of a sensor the chemical information is transformed into a form of energy which may be measured by the transducer.

The ***transducer*** part is a device capable of transforming the energy carrying the chemical information about the sample into a useful analytical signal. The transducer as such does not show selectivity.

The receptor part of chemical sensors may be based upon various principles:

- Physical, where no chemical reaction takes place. Typical examples are those based upon measurement of absorbance, refractive index, conductivity, temperature or mass change.

- Chemical, in which a chemical reaction with participation of the analyte gives rise to the analytical signal.

- Biochemical, in which a biochemical process is the source of the analytical signal. Typical examples are microbial potentiometric sensors or immunosensors. They may be regarded as a subgroup of the chemical ones. Such sensors are called ***biosensors.***

In some cases it is not possible to decide unequivocally whether a sensor operates on a chemical or on a physical principle. This is, for example, the case when the signal is due to an adsorption process.

Sensors are normally designed to operate under well-defined conditions for specified analytes in certain sample types. Therefore, it is not always necessary that a sensor responds specifically to a certain analyte. Under carefully controlled operating conditions, the analyte signal may be independent of other sample components, thus allowing the determination of the analyte without any major preliminary treatment of the sample. Otherwise unspecific but satisfactory reproducible sensors can be used in series for multicomponent analysis using multivariate calibration software and signal processing. Such systems for multicomponent analysis are called sensor arrays.

1.3 Classification of sensors

The development of instrumentation, microelectronics and computers makes it possible to design sensors utilizing most of the known chemical, physical and biological

principles that have been used in chemistry.

Chemical sensors may be classified according to the operating principle of the transducer:

1. ***Optical devices*** transform changes of optical phenomena, which are the result of an interaction of the analyte with the receptor part. This group may be further subdivided according to the type of optical properties which have been applied in chemical sensors:

a) Absorbance, measured in a transparent medium, caused by the absorptivity of the analyte itself or by a reaction with some suitable indicator.

b**)** Reflectance is measured in non-transparent media, usually using an immobilized indicator.

c) Luminescence, based on the measurement of the intensity of light emitted by a chemical reaction in the receptor system.

d) Fluorescence, measured as the positive emission effect caused by irradiation. Also, selective quenching of fluorescence may be the basis of such devices.

e) Refractive index, measured as the result of a change in solution composition. This may include also a surface plasmon resonance effect.

f) Optothermal effect, based on a measurement of the thermal effect caused by light absorption.

g) Light scattering, based on effects caused by particles of definite size present in the sample.

2. ***Electrochemical devices*** transform the effect of the electrochemical interaction analyte – electrode into a useful signal. Such effects may be stimulated electrically or may result in a spontaneous interaction at the zero-current condition. The following subgroups may be distinguished:

a) Voltammetric sensors, including amperometric devices, in which current is measured in the d.c. or a.c. mode. This subgroup may include sensors based on chemically inert electrodes, chemically active electrodes and modified electrodes. In this group are included sensors with and without (galvanic sensors) external current source.

b) Potentiometric sensors, in which the potential of the indicator electrode (ion-selective electrode, redox electrode, metaVmeta1 oxide electrode) is measured against a reference electrode.

c) Chemically sensitized field effect transistor (CHEMFET) in which the effect of the interaction between the analyte and the active coating is transformed into a change of the source-drain current. The interactions between the analyte and the coating are, from the chemical point of view, similar to those found in potentiometric ion-selective sensors.

d) Potentiometric solid electrolyte gas sensors, differing from class 2(b) because they work in high temperature solid electrolytes and are usually applied for gas sensing measurements.

3. ***Electrical devices*** based on measurements, where no electrochemical processes take place, but the signal arises from the change of electrical properties caused by the interaction of the analyte.

a) Metal oxide semiconductor sensors used principally as gas phase detectors, based on reversible redox processes of analyte gas components.

b) Organic semiconductor sensors, based on the formation of charge transfer complexes, which modify the charge carrier density.

c) Electrolytic conductivity sensors.

d) Electric permittivity sensors.

4. ***Mass sensitive devices*** transform the mass change at a specially modified surface into a change of a property of the support material. The mass change is caused by accumulation of the analyte.

a) Piezoelectric devices used mainly in gaseous phase, but also in solutions, are based on the measurement the frequency change of the quartz oscillator plate caused by adsorption of a mass of the analyte at the oscillator.

b) Surface acoustic wave devices depend on the modification of the propagation velocity of a generated acoustical wave affected by the deposition of a definite mass of the analyte.

5. ***Magnetic devices*** based on the change of paramagnetic properties of a gas being analysed. These are represented by certain types of oxygen monitors.

6. ***Thermometric devices*** based on the measurement of the heat effects of a specific chemical reaction or adsorption which involve the analyte. In this group the heat

effects may be measured in various ways, for example in the so called catalytic sensors the heat of a combustion reaction or an enzymatic reaction is measured by use of a thermistor. The devices based on measuring optothermal effects can alternatively be included in this group.

This classification represents one of the possible alternatives. Sensors have, for example, been classified not according to the primary effect but to the method used for measuring the effect. As an example can be given the so-called catalytic devices in which the heat effect evolved in the primary process is measured by the change in the conductivity of a thermistor. Also, the electrical devices are often put into one category together with the electrochemical devices.

Sensors have also been classified according to the application to detect or determine a given analyte. Examples are sensors for pH, for metal ions or for determining oxygen or other gases. Another basis for the classification of chemical sensors may be according to the mode of application, for example sensors intended for use in vivo, or sensors for process monitoring and so on. It is, of course, possible to use various classifications as long as they are based on clearly defined and logically arranged principles.

The biosensors are not presented as a special class because the process on which they are based is, in general, common to chemical sensors. They may be also differentiated according to the biological elements used in the receptor. Those may be: organisms, tissues, cells, organelles, membranes, enzymes, antibodies, etc. The biosensors may have several enzymatic systems coupled which serve for amplification of the signal.

1.4 Chemical sensors for environmental monitoring

Figure 1.1 shows various applications of chemical sensors including monitoring automobile emission gasses, medical diagnosis, industrial control, national security, indoor air quality control, and environmental evaluation.

The regulation on ***automobile emission*** usually involves toxic gases such as nitrogen oxide (NOx), carbon monoxide (CO), or volatile hydrocarbons.

A ***general medical*** examination requires measuring these substances in human body such as glucose, blood oxygen, and cholesterol, which lead to determine possible disease or disorder of a patient.

In a research lab or industrial factory, it is extremely important to prevent accidents from leakage of ***flammable gases such as H_2***, thus the concentration of H_2 on working sites needs to be monitored in real-time.

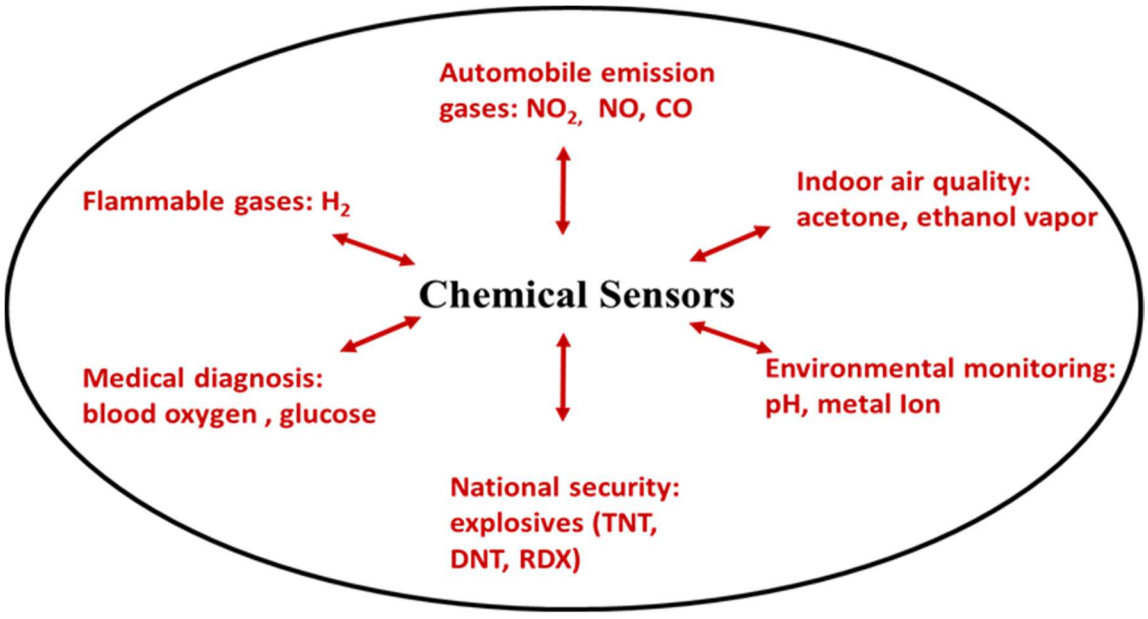

Figure 1.1 Various applications of chemical sensors

There are ***indoor air pollutants*** such as ***volatile organic compounds*** (VOCs) including acetone, ethanol and isopropanol. These organic compounds are widely used as ingredients in household products and extensive exposure to these VOCs can lead to disorder, sickness or even death [1].

Particularly, there have been significant increasing technical demands on indentifying ***explosive chemicals*** due to challenges of anti-terrorism worldwide. Sensors are required to be deployed at public transport station, plaza, schools, and commercial buildings to detect trace amount of explosive molecule such as TNT, DNT, and RDX [2]. Apart from explosive chemicals, recently in last few decades there have been several incidents of the use of ***CWAs*** (mustard gas, sarin, etc.) around the world that killed thousands of lives and threatened the whole civilization [3]. These incidents worldwide highlight the importance of having a continuous detection and monitoring of these kinds of chemical agents and explosives for both defense and homeland security.

Chemical sensors are expected to play a critical role in environmental monitoring (both indoor and outdoor) and environmental control (air, water), facilitating a better quality of life. The projected increase in global energy usage and unwanted release of pollutants has led to a serious focus on advanced monitoring technologies for environmental protection, remediation, and restoration. In a recent study, the World Health Organization (WHO) reported that over 3 million people die each year from the effects of air pollution. Furthermore, reports from World Energy Congress (WEC) suggest that if the world continues to use fuels reserves at the current rate, the environmental pollution in 2025 will create irreversible environmental damage. Long-term exposure to air pollution provokes inflammation, accelerates atherosclerosis, and

alters cardiac function. Within the general population, medical studies suggest that inhaling particulate matter (PM) is associated with increased mortality rates which are further magnified for people suffering from diabetes, chronic pulmonary diseases, and inflammatory diseases. Pollution, in general is contamination that renders part of the environment unfit for intended or desired use. Natural processes release toxic chemicals into the environment as a result of ongoing industrialization and urbanization. Major contributors to large-scale pollution crisis are deforestation, polluted rivers, and contaminated soils. Other sources of pollution include emissions from iron and steel mills; zinc, lead, and copper smelters; municipal incinerators; oil refineries; cement plants; and nitric and sulphuric acid producing industries. Of the group of pollutants that contaminate urban air, nitrous oxide (NO_x), fine suspended PM, sulphur dioxide (SO_2), and ozone pose the most widespread and acute risks. Recent studies on the effects of chronic exposure to air pollution have singled out PM suspended in smog (NO_x) and volatile organic compounds (VOCs) as the pollutant most responsible for life-shortening respiratory and associated health disorders. Since the Clean Air Act was adopted in 1970, great strides have been made in the U.S. in reducing many harmful pollutants from air, such as SO_2. Levels of NO_x, however, have increased by 20% over the last 30 years. Sources of NO_x include passenger vehicles, industrial facilities, construction equipment and railroads, but of the 25 million tons of NO_x discharged annually in the U.S., 21% of that amount is generated by power plants alone, resulting in rising threats to the health of the general population. Furthermore, the SCanning Imaging Absorption SpectroMeter for Atmospheric CHartographY (SCIAMACHY), shows rapid increase in NO_x columns worldwide, especially since 2003.

Rapid detection of contaminants in the environment by emerging technologies is of paramount significance. Environmental pollution in developing countries has reached an alarming level thus necessitating deployment of real-time pollution monitoring sensors, sensor networks, and real-time monitoring devices and stations to gain a thorough understanding of cause and effect. A tool providing interactive qualitative and quantitative information about pollution is essential for policy makers to protect massive populations, especially in developing countries.

1.5 Microcantilever heater based environmental sensors

Detection of volatile organic compounds (VOCs), which are widely used in industrial processes and household products, is very important due to significant health hazards associated with them.[1] VOCs are commonly detected using photo-ionization detectors (PIDs),[2] suspended hot bead pellistors,[3] or heated metal oxide semiconductor functionalization layers.[4]-[7] The detection methodology using PIDs is based on high-energy photon (typically > 10.5 eV) induced ion generation, while that using hot bead pellistors takes advantage of the exothermic reaction (from auto-ignition of VOCs) to produce a change in resistance. Heated metal oxide (i.e. TiO2 or SnO2) based sensing also relies upon a change is resistance, but at a temperature below the auto-ignition temperature of the VOCs. However, all the above techniques suffer from the problem of high power requirement as well as poor selectivity among VOCs, which is often important for proper identification of the source of a problem. Although the last method requires somewhat lower operational power, it involves complicated functionalization process with metal oxides.

Microcantilevers offer excellent avenues for molecular sensing that arises out of their high sensitivity to various physical parameter changes induced by the analyte molecules.[8]-[15] Microcantilever heaters, which are extremely sensitive to changes in thermal parameters,[16]-[21] have been widely utilized for calorimetry,[16] thermal nanotopography[17] and thermal conductivity measurements.[18] Due to the small area of the microcantilever that needs to be heated (i.e. the tip of a triangular microcantilever), they also offer the possibility of reduced power consumption for high temperature operation. However, achieving repeatable and reliable functionalization of a microcantilever, especially over a small area, is a challenge that has thwarted practical applications of microcantilever based sensors. On the other hand, unfunctionalized microcantilevers (typically made of Si) are not particularly sensitive toward a specific analyte, and are generally accepted to be incapable of performing selective detection. Thus, only a handful of studies utilizing uncoated microcantilevers to perform unique molecular detection have been reported so far.[13], [22], [23] In these studies, detection is generally based on changes in physical properties of the media surrounding the cantilever (i.e. viscosity,[23] thermal conductivity,[22] or the analyte (i.e. deflagration temperature[22]). However, these techniques are applicable only to a few specific analytes, and selective detection still remains a major challenge, especially when the analytes are diluted (or present in minute quantities) or have similar physical properties i.e. VOCs.

III-Nitride heterojunction (especially AlGaN/GaN) based microcantilevers offers a unique opportunity for realizing these microscale heaters, taking advantage of presence of high carrier (electron) density in close proximity to the surface,[24] which allows for

highly efficient surface heating. In addition, strong spontaneous polarization of III-Nitride surfaces allows these heaters to interact better with VOCs, which are typically strongly polar in nature. Finally, AlGaN/GaN heterojuntion based heaters are capable of operating at high temperature and harsh environment due to chemical inertness and wide bandgap of III-Nitrides. With commercial availability of high quality III-Nitride heterojunciton epilayers on Si, the fabrication of these heaters is also quite straightforward. Although, III-Nitride based microcantilevers have been demonstrated earlier,[11], [25], [26] there is no report so far on triangular microcantilever heaters and their sensing applications.

Chapter 2

Fabrication of AlGaN/GaN Microcantilever Heaters

Microcantilevers, as we have discussed previously, offer outstanding opportunities for bio/ chemical sensors, as they can be highly sensitive to specific bio/chemical analytes. In addition, micro heated cantilevers have been shown to be extremely useful for calorimetry [3,4] and chemical sensing [5]. While several studies have shown that microcantilevers can be fabricated with internal resistive heaters [6,7], little work has been done to converge microcantilevers with microhotplates for sensing applications. Microfabricated hotplates have previously been used for various sensing applications, including as a Pirani gauge [8], gas sensor [9], and a flow-rate sensor [10]. In some cases, the method or materials of microsensor fabrication limit its performance. The main design considerations for microhotplates are thermal isolation and temperature uniformity that can be achieved through free standing heatable microstructures, which are either bridges or cantilevers. King *et al.* fabricated micro hotplates which were made of Silicon microcantilevers. Figure 2.1 (a) Scanning electron microscope (SEM) and (b) infrared (IR) microscope images of the fabricated heated cantilever, indicating heating only near the free end of the cantilever [7]. shows (a) scanning electron microscope (SEM) image and (b) infrared (IR) microscope image of the heated cantilever during steady electrical excitation. The IR image is approximately 0.5 mm^2. The doped silicon

cantilever is fabricated in a “U” shape such that it forms a continuous electrical path. The region near the cantilever free end is a highly resistive heater and the legs have lower electrical resistance. The IR image confirms substantial heating only near the free end of the cantilever.

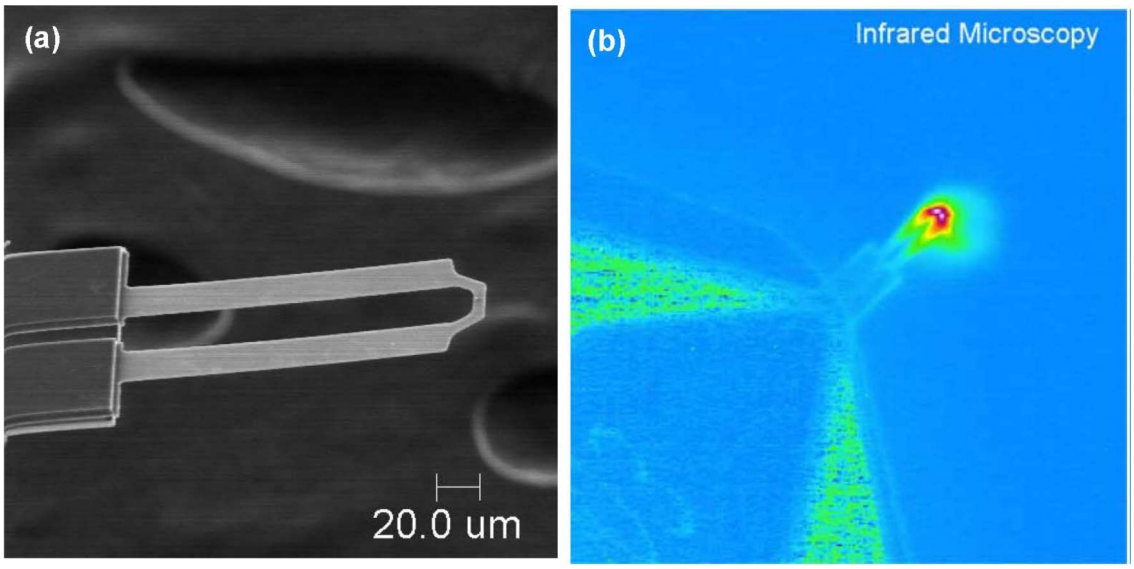

Figure 2.1 (a) Scanning electron microscope (SEM) and (b) infrared (IR) microscope images of the fabricated heated cantilever, indicating heating only near the free end of the cantilever [7].

In this chapter we will describe the different process for a representative device and scanning electron micrograph images of various MEMS devices. All the fabrication processes were carried out in the Microelectronic Research Center (MiRC) in Georgia Institute of Technology, Atlanta, GA.

2.1 Wafer information

A six inch AlGaN/GaN wafer grown on Silicon (111) substrate was purchased from *NTT Advanced Technology Corporation, Japan* for this work. The wafer was diced into ~ 44 (1.8 cm by 1.8 cm) square pieces. Before dicing, the wafer was coated with

photoresist (Microposit SC1827) and then baked for 5 mins at 110°C. This was solely to protect the top surface from any damage that could happen during wafer dicing. The different layers of the wafer are shown in Figure 2.2.

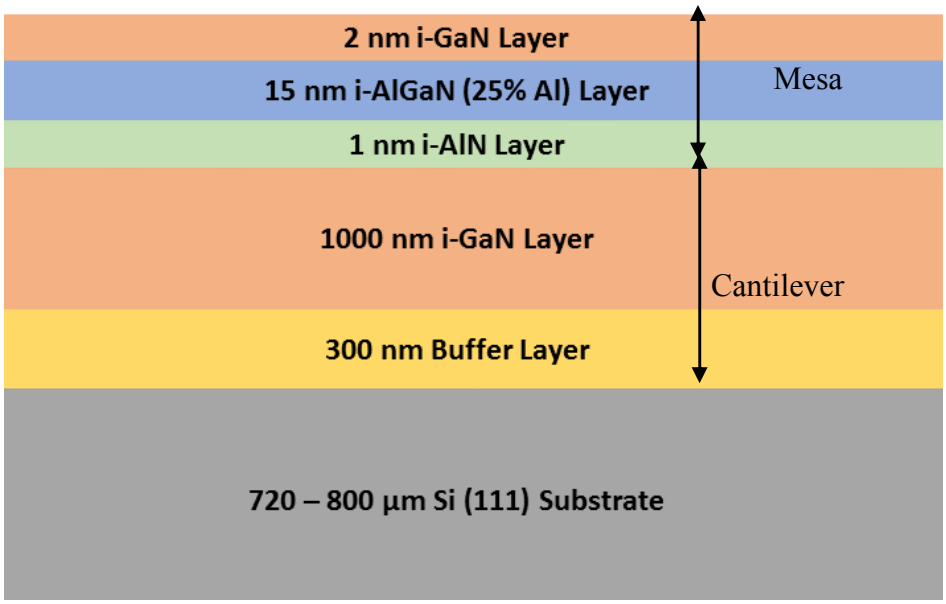

Figure 2.2 Different layers of the AlGaN/GaN wafer grown on Si (111) substrate with mesa and cantilever layer as shown.

Silicon substrate (111) of ~ 720-800 µm thickness was used to grow the AlGaN/GaN layer [211]. A 300 nm buffer layer (not disclosed by the company) was used as a transition layer before growing 1 µm undoped GaN layer. This transition layer along with the undoped GaN form the thickness of our microcantilevers, although the overetching of Si from the bottom of the wafer also reduced the cantilever thickness to 600-800 nm. On the top of the GaN layer, a thin layer of 1 nm AlN was used to form abrupt junction and better electron confinement in 2DEG by tuning the bandgap. Above that layer we have our active layer of AlGaN of 15 nm and 2 nm of GaN cap layer.

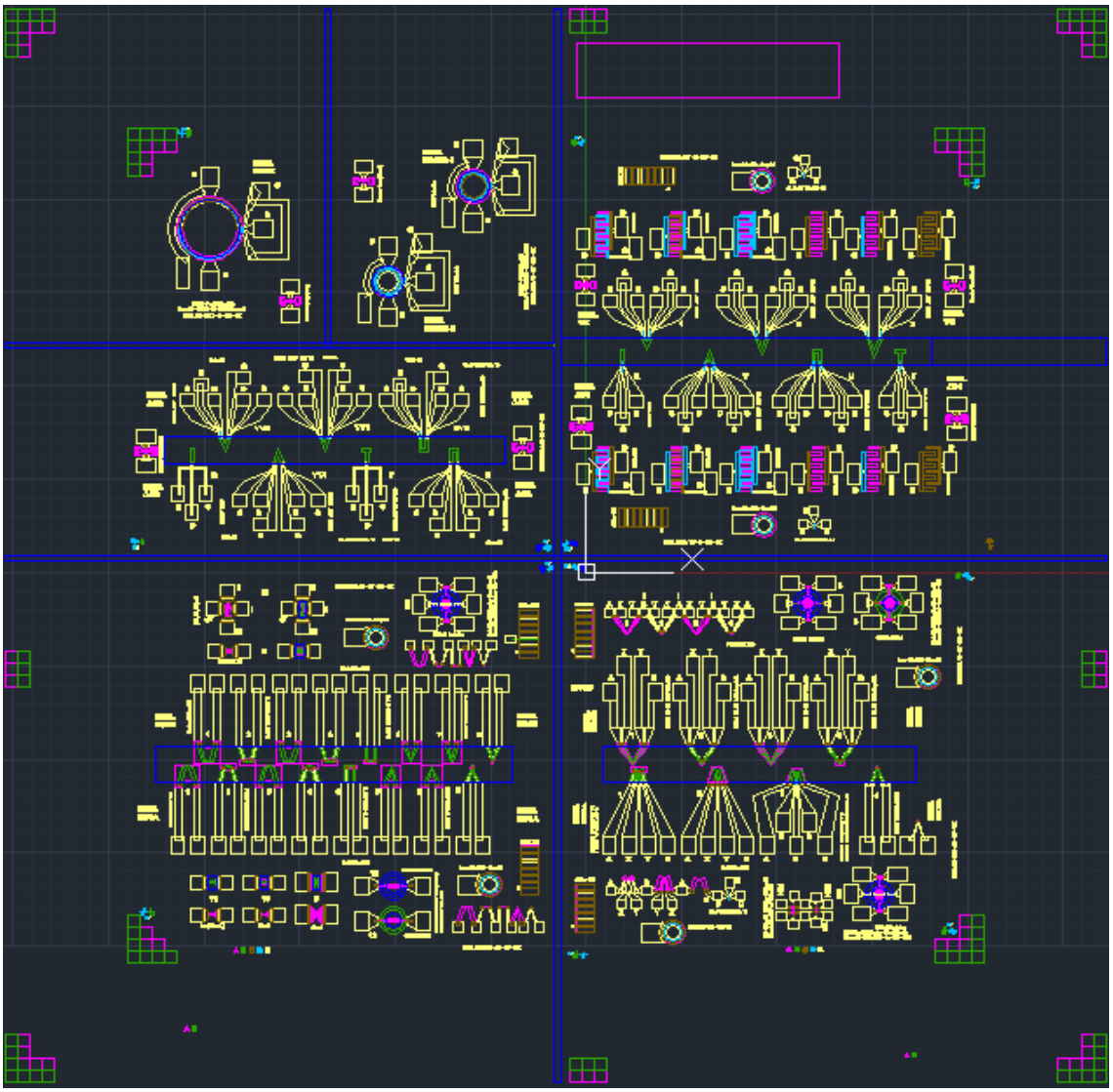

Figure 2.3 Mask layout - the final design including all the layers superimposed showing the schematic of the final outcome of the fabricated devices. The mask design has the provision for auto dicing each sample into several chips.

2.2 Mask design

Two 5”×5”×0.09” bright field masks (material: chrome, substrate: quartz) were ordered from *Photo Sciences Inc., USA* after designing in *AutoCAD 2013*. There were 7 lithographic layers in the fabrication process (described in details in the next section),

Figure 2.3 shows all these layers superimposed on each other. Three layers (Mesa isolation, GaN cantilever outline, and Backside Si etch) were of 1.8 cm by 1.8 cm size and other three layers were of 1.4 cm by 1.4 cm size. The back side alignment layer for through wafer Si etching was mirrored with respect to the first two top layers since the design was asymmetrical. The wafer was diced in 1.8 cm by 1.8 cm square pieces, though the active device area was of 1.4 cm by 1.4 cm size. The additional free space around the active area was to facilitate sample handling and to avoid using the relatively thicker photoresist film near the edge of the sample.

2.3 Details of the fabrication steps

In this section the fabrication related issues, problems and solutions are discussed in two subsections covering the top cantilever outline followed by through wafer Si etching from backside. The first sub-section is segmented into six sub-sections where each lithography step and associated process steps are discussed (process flow shown in Figure 2.4). For further details readers are advised to refer to the appendix. Positive photo resist (Microposit SC 1827) was used for the first process step, whereas negative photo resist (NR71-3000P) was used for the rest and NR5-8000 was used in Bosch process for releasing cantilevers.

2.3.1 Top GaN microcantilever outline

2.3.1.1 Step 1-Mesa outline:

Mesa is the active region on which the AlGaN/GaN heterostructure channel is fabricated. This is because AlGaN/GaN layer has 2DEG throughout the wafer, therefore it is conductive all over and needs to be isolated from other patterns on the sample. Only in this layer SC1827 was used (the litho parameters are given in appendix).

PECVD SiO_2 (300 - 400 nm) was deposited using Unaxis PECVD tool (deposition rate is 50 nm/min) at the beginning. The oxide was patterned and then etched in Plasma Therm Inductively Coupled Plasma (ICP) tool (etch rate is 180 nm/min, CHF_3/O_2 gas). Then BCl_3/Cl_2 based dry etching recipe of GaN was used in Plasma Therm ICP to etch 180-200 nm thick AlGaN/GaN to isolate the mesa. After the etching, the PR was completely removed from top oxide layer using resist remover, oxygen plasma cleaning in Reactive Ion Etcher (RIE), and if necessary dipping in hot sulphuric acid (H_2SO_4) for 5-10 minutes. The resist got crosslinked in ICP and it became literally impossible to remove with just resist remover or acetone. However, bare AlGaN/GaN mesa should never be exposed to oxygen plasma, otherwise 2DEG would be completely damaged. Once resist is removed, Buffered Oxide Etchant (BOE) should be used to remove the SiO_2 off the mesa.

2.3.1.2 Step 2-GaN cantilever outline:

In this step, GaN was etched down to make an outline for the cantilever. GaN was etched down in the pocket area up to the substrate where silicon got exposed. This process was exactly same as step 1. Only difference is the deposited oxide was 1.2 µm thick. Over etching (assuming 2 µm thick GaN) was performed as the etched down GaN had other layers. BCl_3/Cl_2 plasma, used for etching GaN, also etched exposed Si (verified using Tencor Profilometer) with same etch rate of 340 nm/min, but this did not affect any fabrication process as ultimately the exposed Si was etched from backside completely. In this step and the next ones in this sub-section, negative photo resist (NPR) NR71 was used (see appendix for details). After the etching of oxide similarly as step 1, resist was

removed. After resist removal, wet chemical etching of the oxide was done using Buffered Oxide Etchant (BOE).

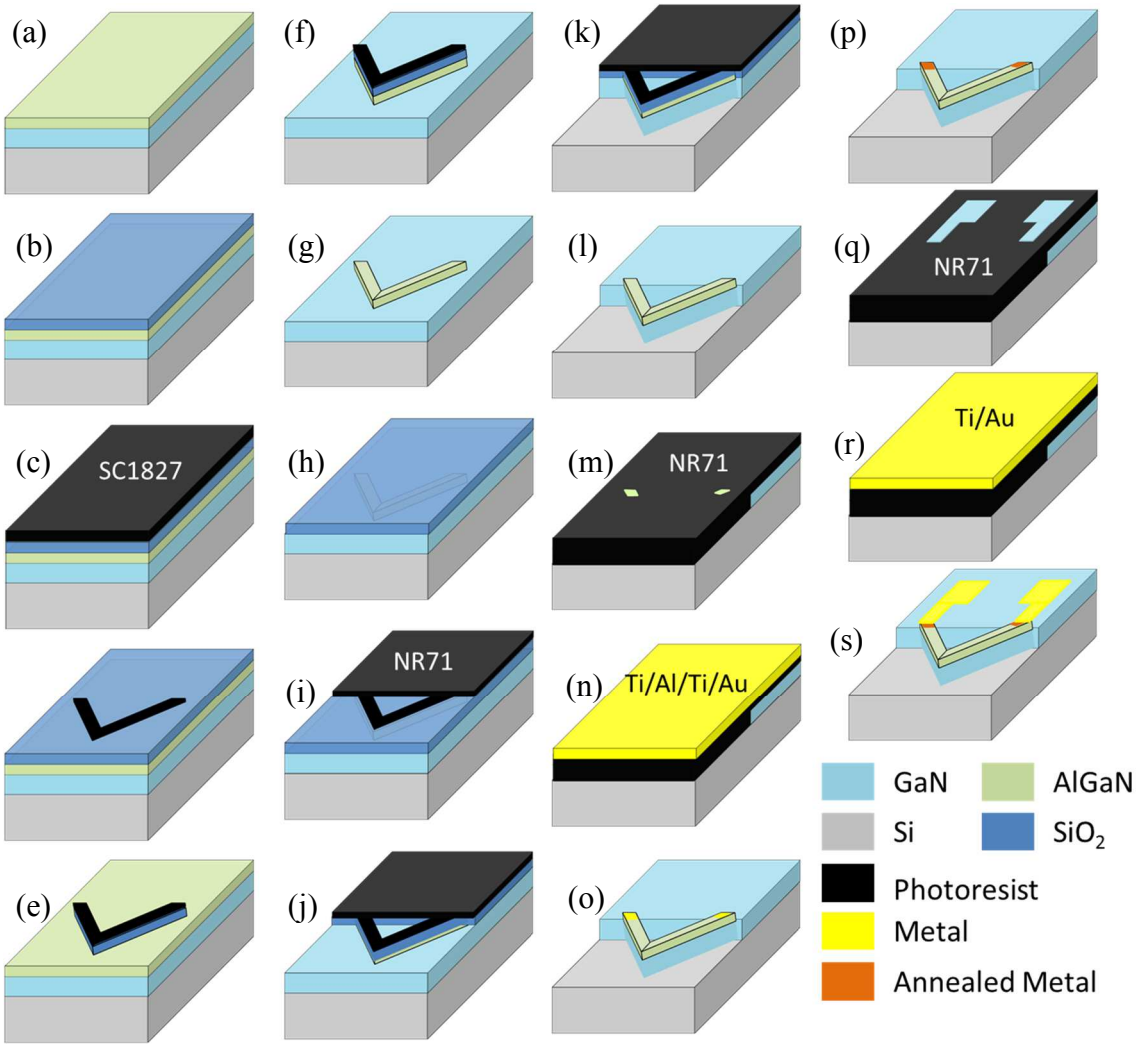

Figure 2.4 Process flow diagram of top GaN microcantilever. (a) A diced AlGaN/GaN on Si sample; (b) PECVD SiO_2 (300 - 400 nm) deposition; (c) Coat sample with SC1827 photoresist; (d) Pattern photoresist; (e) Pattern the mesa layer with ICP etching of oxide; (f) ICP etching of AlGaN; (g) Remove oxide using BOE; (h) PECVD SiO_2 (1.2 µm) deposition; (i) Pattern cantilever outline with NR71 photoresist; (j) ICP etching of oxide; (k) ICP etching of GaN; (l) Oxide etching with BOE; (m) Pattern Ohmic Contact using NR71; (n) E-beam deposition of Ti/Al/Ti/Au metal stack; (o) Lift-off of ohmic layer; (p) Rapid thermal annealing of ohmic contacts; (q) Pattern probe contact using NR71; (r) E-beam deposition of Ti/Au metal stack; (m) Lift-off of probe contact layer.

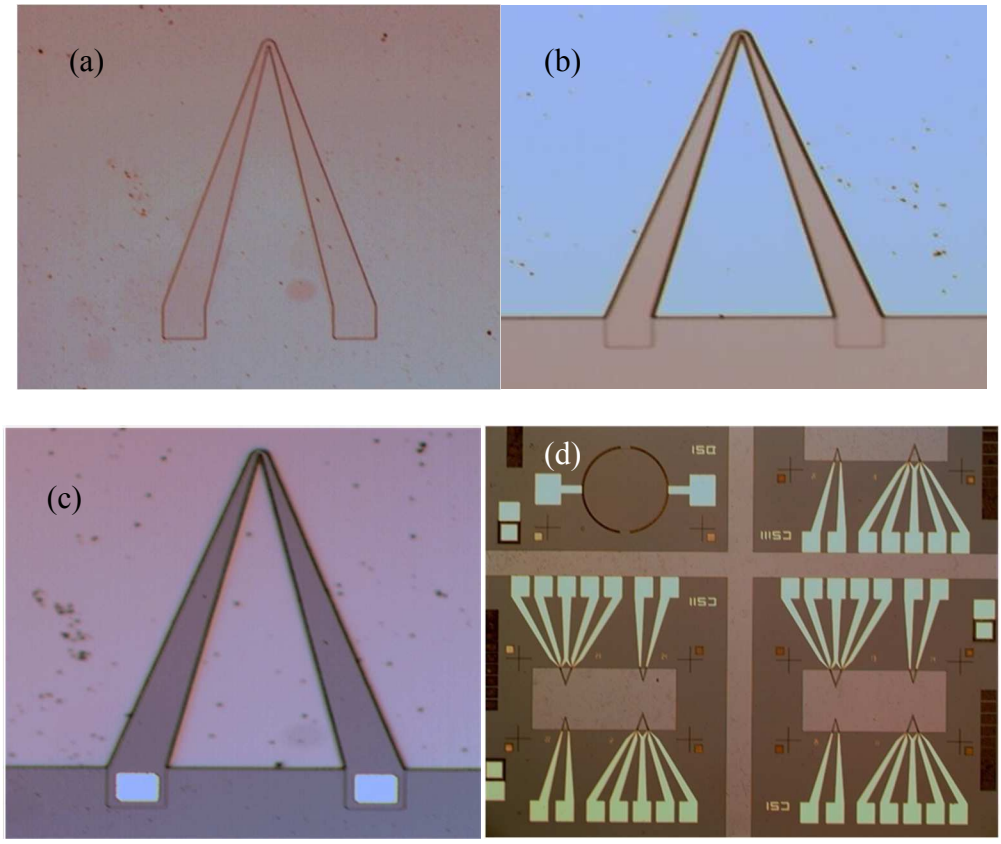

Figure 2.5 Optical images taken at various stages of fabrication: (a) Mesa outline; (b) Cantilever outline; (c) Ohmic contact deposition; (d) Probe contact deposition.

2.3.1.3 Step 3-Ohmic contact:

For ohmic contact multilayer metal stack of Ti (20 nm)/Al (100 nm)/Ti (45 nm)/Au (55 nm) was used. Getting a good ohmic has always been a challenge [252] and multilayer metal stack gives low contact resistance [253]. The reason for choosing this metal stack is well explained in [252, 254]. For a good and easy metal liftoff process, overdevelopment is suggested after post bake of resist as very thin layer of resist would be always present.

The metal liftoff was done in warm resist remover (RR41), then the sample was put in fresh warm resist remover for 10-15 minutes, followed by cleaning with

isopropanol. No oxygen plasma cleaning was done on the sample with bare AlGaN/GaN mesa. After lift-off was done, the contact was annealed in SSI RTP at 825 °C.

2.3.1.4 Step 4-Probe contact:

Large metal pads (250 µm by 250 µm) were deposited for characterization which were connected to the ohmic contacts. Gold (250 nm) with adhesion layer of Ti (20 nm) was used for this metal deposition step. The lift off process remains the same as mentioned in step 3. Optical images at different stages of cantilever top outline fabrication is given in Figure 2.5.

2.3.2 **Through wafer Si etch from backside using Bosch process**

The cantilevers were released by through wafer etching of Si using STS ICP etcher. We used 'Bosch process' where the etcher alternates between an 'etch' cycle and 'passivation' cycle (Figure 2.6). During the etch cycle, Si was isotropically etched using SF_6 for 10 seconds, then the etched region was passivated with a polymer (C_4F_8) for 7 seconds in the passivation cycle. The whole process continued alternatively as long as the cantilever was not released, resulting in a high aspect ratio Si etch with vertical side walls.

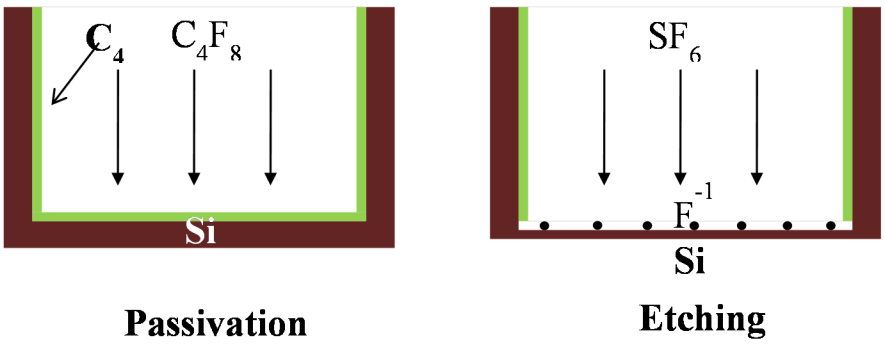

Figure 2.6 Working principle of Bosch process: passivation cycle and etch cycle.

2.3.2.1 *Existing problems with previous process:*

The usual practice of processing this particular layer involves depositing thick SiO_2 on the back side which acts as the hard mask for Si etching. Then patterning with NR 71 resist (4 µm thick), the oxide is wet chemically etched using BOE. The resist is then removed from the backside and also from the top side (which acts as a protecting layer of the devices on the top side from spinner and BOE). After that the sample is put into ICP to etch Si for releasing the cantilevers. This process is faster and easier; however there are several key factors that affect the final outcome. In ICP the selectivity is about 90:1 between Si and SiO_2. For a wafer of 500 µm thick (our first generation wafer from Nitronex Inc), the oxide needs to be 7-8 µm thick on the backside of the sample and also in the carrier wafer. The carrier wafer is needed for mounting small samples with cool grease before loading in the ICP chamber. Now if the pocket (where the Si will be etched) is big enough and the layer has symmetric design with moderately thick Si substrate, the above mentioned process works fine but will have lot of undesirable undercut of Si, resulting in over hung cantilevers. This process becomes totally inapplicable and impractical if:

(a) The thickness of Si wafer is above 600 µm, as the thickness of oxide would be more than 8 µm which would require longer tool time. Like our recent wafer which is 720-800 µm, the oxide thickness should be more than 10 µm. The PECVD tool in MiRC allows 3 µm thick film deposition at a time, but the quality becomes bad. So it is advised to deposit 2 µm thick oxide (50 nm/min deposition rate needs 40 minutes), then run clean process for 2 hours and

deposit again. That means more than 14 hours of total processing time is required from that tool.

(b) If the design has asymmetry with pocket size varying from 50 µm to 800 µm, the etch rate of Si in ICP will vary significantly as bigger pocket gets etched faster. Eventually it will take almost double the theoretical time (400 nm/cycle, each cycle is 17 seconds long) to completely release suspended structures from all the pockets. Most importantly BOE etching of that thick oxide with a large variety in pocket size is literally impossible to control, resulting in under-etched or over-etched SiO_2 mask and eventually a totally deformed structure after etching Si with that hard mask. The fabrication yield would be very low with this process.

(c) The tool time required for the ICP would be ~ 12 hours for releasing all the structures, assuming 1000 µm thick (taking into account for the different pocket sizes) Si and etch rate of 400 nm/cycle. That much deep Si etching would obviously result in a lot of undercut.

2.3.2.2 New process development to release suspended structure:

To account the above mentioned problems and to ensure higher fabrication yield with zero undercut in the microcantilevers, new process was designed. The process flow is shown in details in Figure 2.7. The details of this new process are described below:

(a) *Thinning down of bare Si substrate*: To deal with ~800 µm thick Si, the samples were first thinned down in STS ICP using the Bosch recipe to make the thickness about 400 µm. The other recipe can be used just with SF_6 etch cycle with no passivation cycle which would be faster. However, selectivity

ratio would be lower with SiO_2 (measured to be 40:1 instead of 90:1). But this does not affect anything at all as long as the carrier wafer has enough oxide (in this case the thickness was 9 µm). To mount the sample cool grease was used carefully on the top side, at the corners and open area outside 1.4 cm square box. As there will be no resist removal step in this whole process, unfortunately the top surface was not protected with any resist coating. Also the resist may get cross linked for this long duration of Si etching, so if possible the resist coating on the top surface should be avoided. Another important thing is, if the cool grease is not applied enough, the samples get very hot and metal layers get peeled off from the surface (see appendix). So this step was done in intervals with 260 cycles runtime with 10 minutes pause. Total 760 cycles of the Bosch recipe was run to etch ~350 – 400 µm Si with an etch rate of ~500 nm/cycle (the etch rate is higher as bare Si was etched). The tool time was ~4 hours.

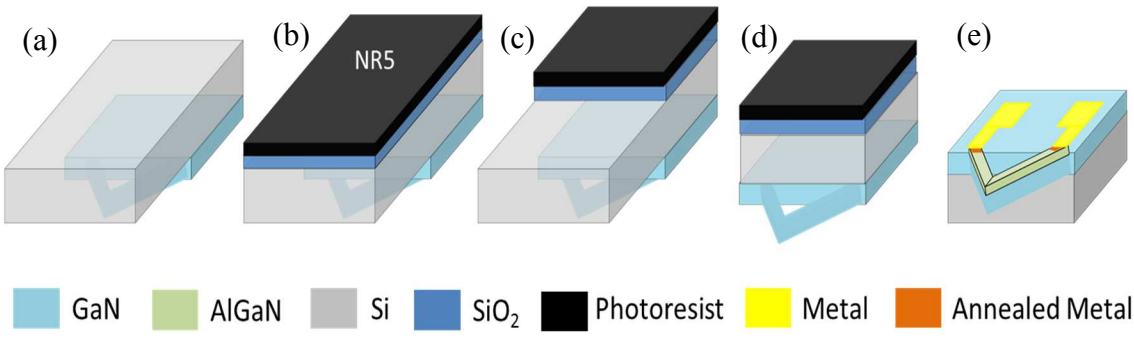

Figure 2.7 Process flow diagram of through wafer Si etching from backside using Bosch process. (a) A flipped sample - thinning down the Si substrate (~ 400 µm) in ICP ; (b) PECVD SiO_2 (4 µm thick) deposition; (c) Photoresist NR5-8000 (8 µm thick) coating; (d) Pattern the resist layer and etch SiO_2 in RIE; (e) Through wafer Si etching in ICP using Bosch process; (f) Schematics of the released GaN.

(b) *Oxide deposition*: As the thinned down sample has become ~400 µm thick, so a total of 4 µm thick oxide was deposited in Unaxis PECVD tool in two slots. After 2 µm deposition (50nm/min) a clean process was run for 2 hours and the final 2 µm was deposited. Though from the selectivity 5 µm thick oxide seems necessary, but the photo resist would support the extra etching cycles. Also, even if the oxide gets etched down at one point, the pattern would be already there, and the Si substrate would only get thinned down without any harm. It is a good practice to prepare carrier wafer which could be low quality clean Si wafers with at least 8 µm thick oxide. Each wafer should be used only once in the ICP. The tool time was 2 hours and 40 minutes in Unaxis PECVD and it was same in STS PECVD 2. But the later had better quality oxide than the former with only drawback being less number of samples to be loaded inside it. If time permits, it is better to use the later tool to deposit oxide following the same procedure.

(c) *Photolithography*: The thinned down and oxide deposited sample was patterned with NR5 photoresist. The litho parameters are given in the appendix (similar to NR71). The reason for using NR5 was its thickness, minimum being 8 µm (at 3000 rpm) and maximum being 100 µm (at 500 rpm). The resist acts as a mask not only for etching oxide but also during Si etching. The selectivity was found to be 1:1 with oxide in RIE and 40:1 with Si in ICP. So there should about 4 µm resist left after etching oxide to cushion against etching the first 140 – 160 µm Si. That also helped in depositing

thinner oxide film. However care should be taken to choose the thickness of the resist; as for higher thicknesses, resist thickness was not uniform and after development there was a broadening in the narrow areas of the profile. The optimized thickness was found to be 8 µm which gave good results. Up to 15 - 20 µm thickness would be fine with NR5. Both NR5 and NR71 are good etch resist but NR71 offers maximum thickness of 12-14 µm but is less reliable. The litho step was same as before, but after the development, oxygen plasma cleaning was run for 1-2 minutes to ensure no resist film was remaining in the pockets.

(d) *Dry etching of oxide*: The 4 µm thick oxide was etched down using NR5 as the mask in two slots with 2 µm film being etched every time and running a complete clean process for 3 hours in between in Plasma Therm RIE. The etch rate was 50 nm/min but over etching was done (assuming 5 µm thickness) to ensure complete etching of the oxide from the pocket. As the backside was rough, it became harder to justify if a thin film of oxide was remaining or not. However it would again not affect the process due to longer etching of Si. It is to be noted that, as the etching was done assuming 5 µm thick oxide, the remaining resist would be 3 µm, which would be good enough to provide additional support during Si etch. Before optimizing the process, two samples were simultaneously processed but one was used in RIE to etch oxide and the other one was etched with BOE to compare the results. After the etching, the damages due to BOE was visible but still it was processed further. The total tool time was ~4 hours.

(e) *Deep Si etching with Bosch process*: The samples (~400 µm thick Si substrate) were mounted on carrier wafer with sufficient cool grease. While applying grease with swab on the top surface, the nearby area surrounding the top pocket (where the GaN was etched) was avoided as the exposed cool grease (after etching Si) would be sputtered and re-deposited all over the sample. The standard Bosch recipe was used and the samples were processed for 1000 – 1200 cycles in slots of 250 cycles and 10 min pause in between, so that the samples did not get over heated. Over etching did not affect as GaN was barely etched with SF_6 (about 200 – 300 nm). However in the new wafer the cantilever thickness was 1.1 µm after mesa etching. So care should be taken or this can aid in thinning down GaN slowly if different thickness of cantilever is required. Visual inspection would be enough to ensure complete etching and also the samples would be auto diced as per design. The total tool time in STS ICP was ~6 hours. The SEM images of some of the many different released structures are shown in the next section. While Figure 2.8 through Figure 2.11 show some photographs taken at various steps of the Bosch process, Figure 2.11 compares the final results with previous process and the new process.

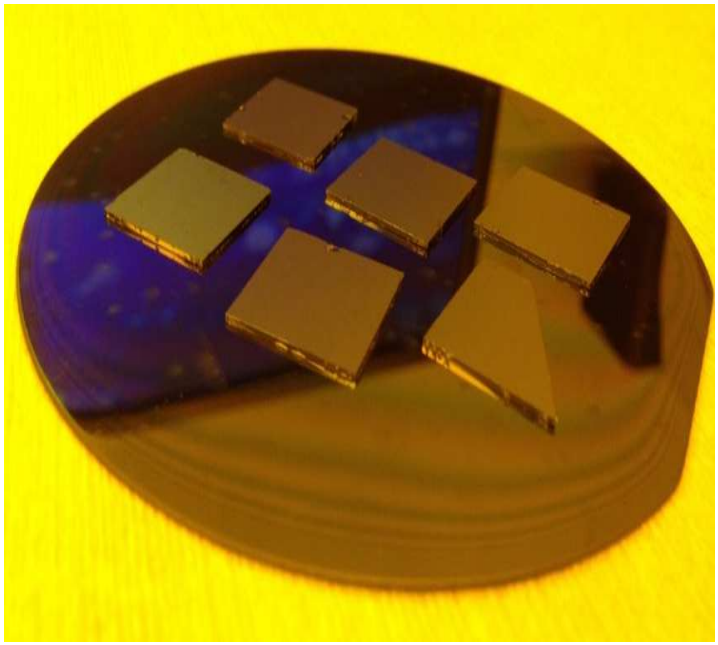

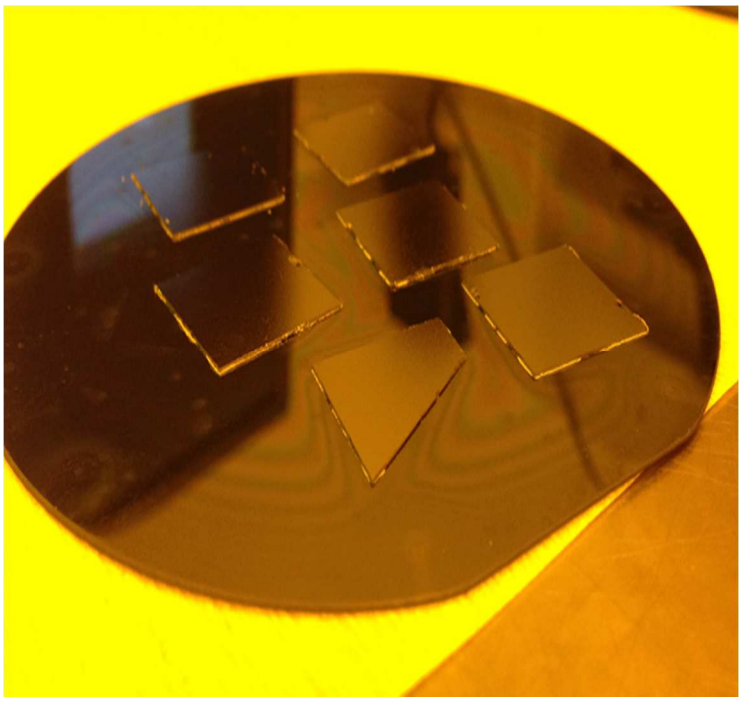

Figure 2.8 Photograph of samples (top) before thinning down the Si substrate (bottom) after thinning down. The samples were dismounted carefully from the wafer with very thin syringe/niddle and sharp tweezers not to damage the devices on the top surface.

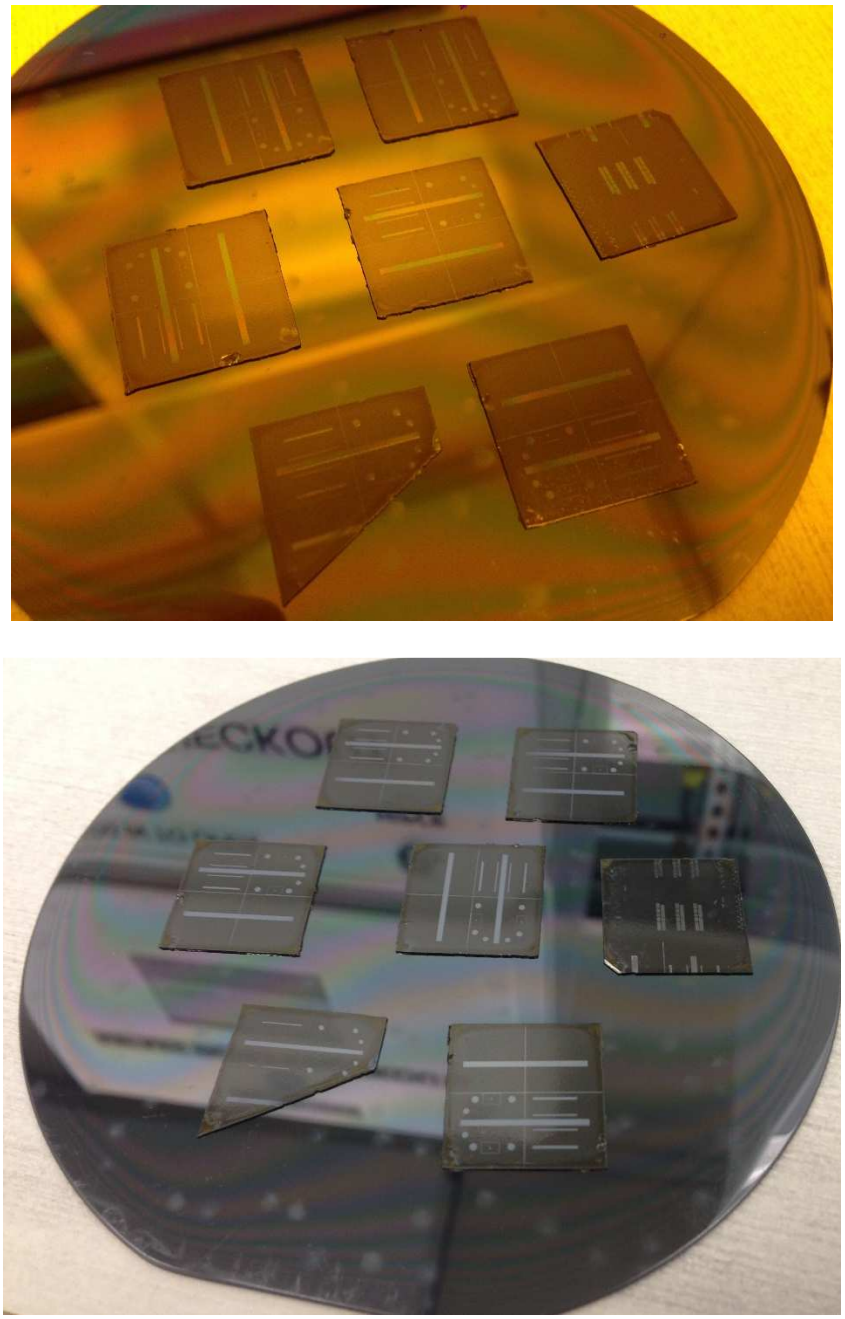

Figure 2.9 Photograph of samples (top) after patterning resist on the PECVD oxide (bottom) after etching the oxide in RIE.

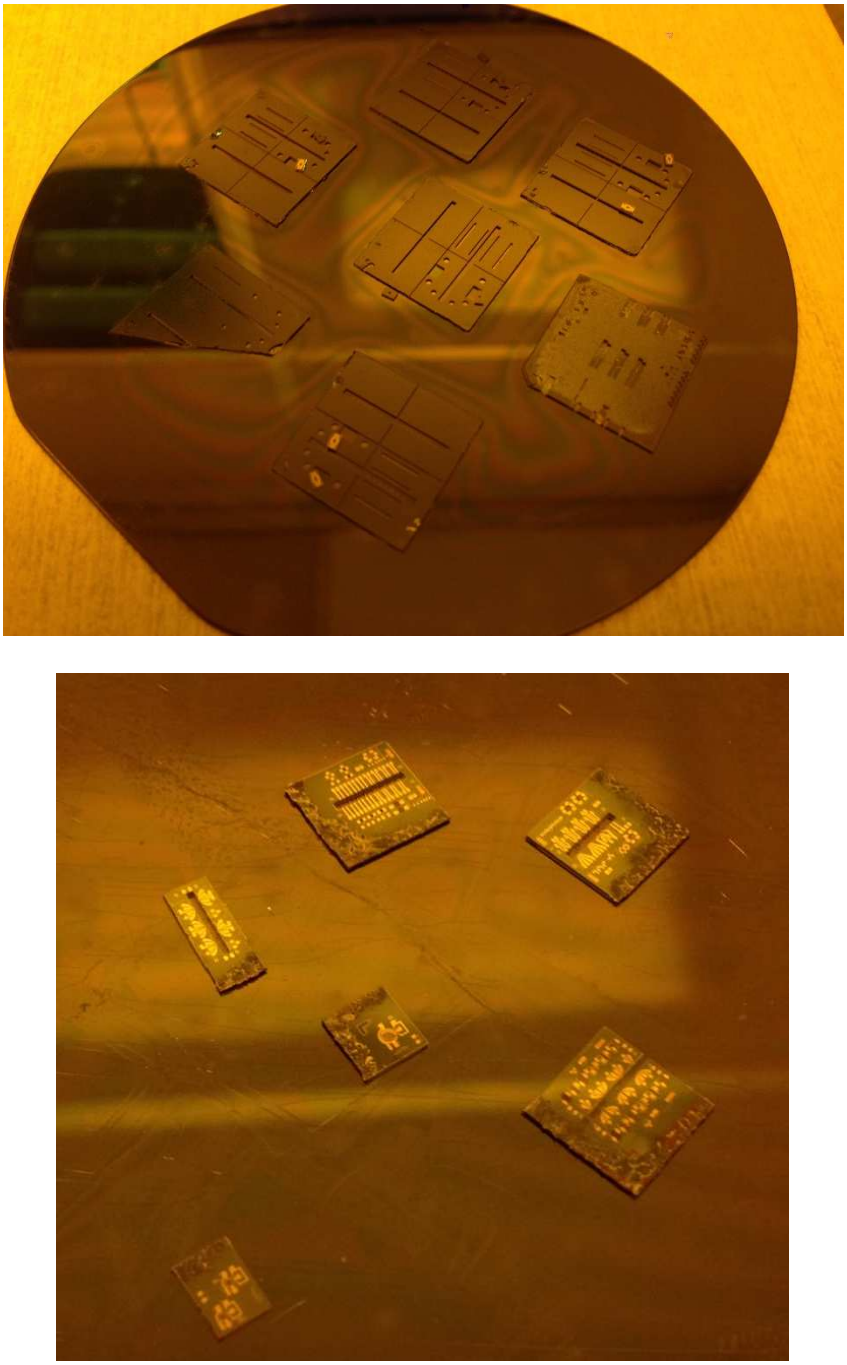

Figure 2.10 Photograph of samples (top) after through wafer Si etching; (bottom) auto-diced into smaller chips.

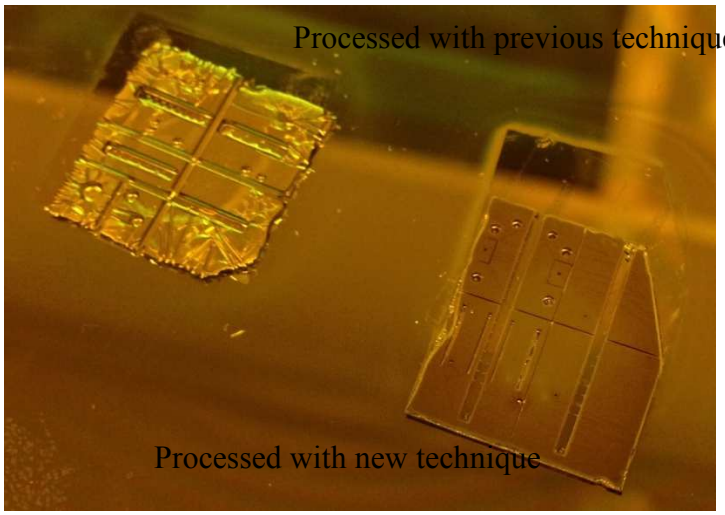

Figure 2.11 Photograph of samples comparing the releasing of microcantilevers with two different techniques which shows the incompatibility and inapplicability of the old technique for processing sophisticated designs.

2.4 Image Gallery: Optical and Scanning Electron Microscopy (SEM)

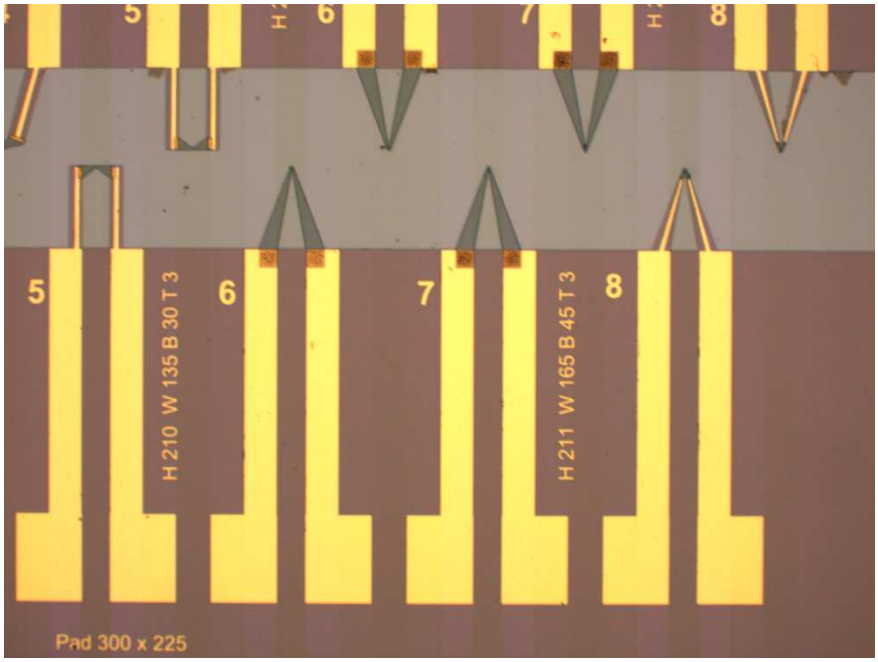

Figure 2.12 Optical image of the top outline showing the single channel microcantilever heaters.

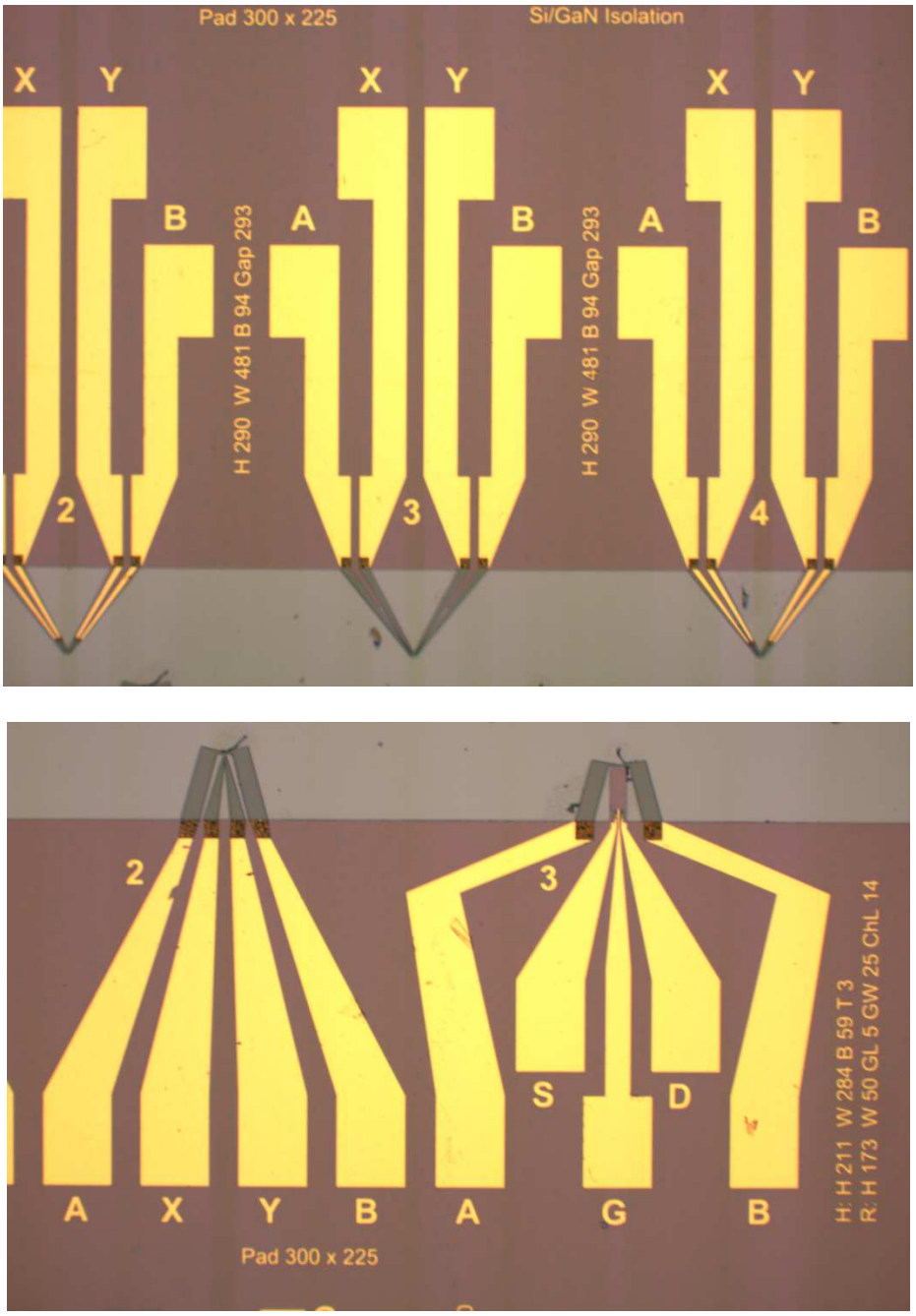

Figure 2.13 Optical image of the top outline showing the (top) dual channel microcantilever heaters and (bottom) compound microheater structures.

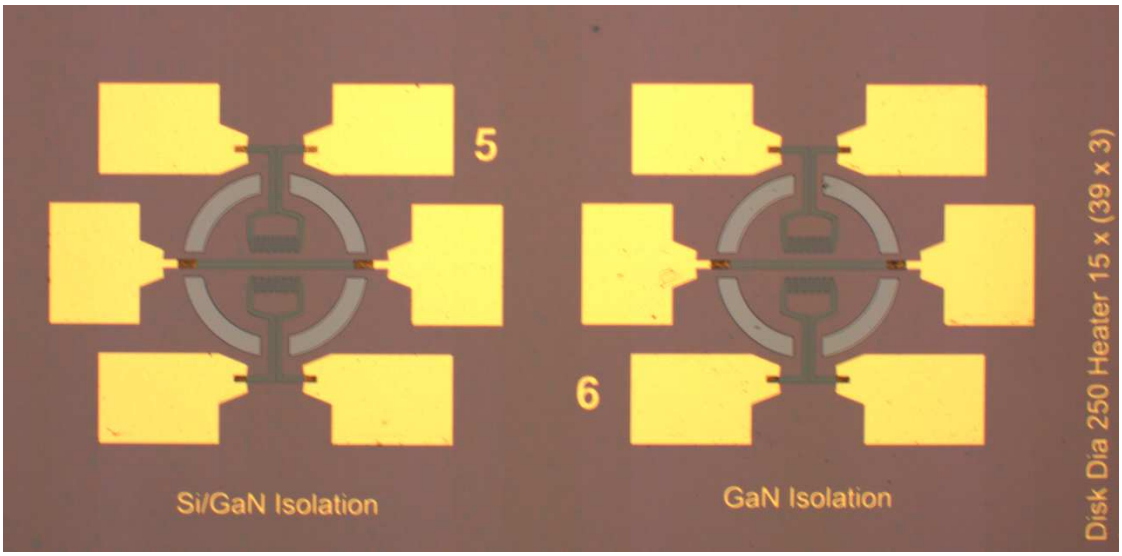

Figure 2.14 Optical image of the top outline showing the micro hotplates.

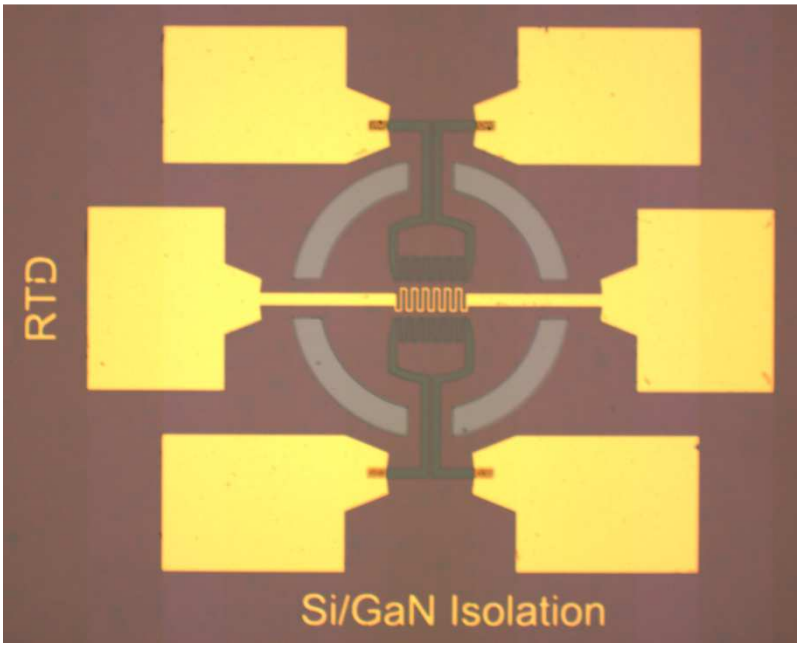

Figure 2.15 Optical image of the microhotplate with resistance temperature detector (RTD).

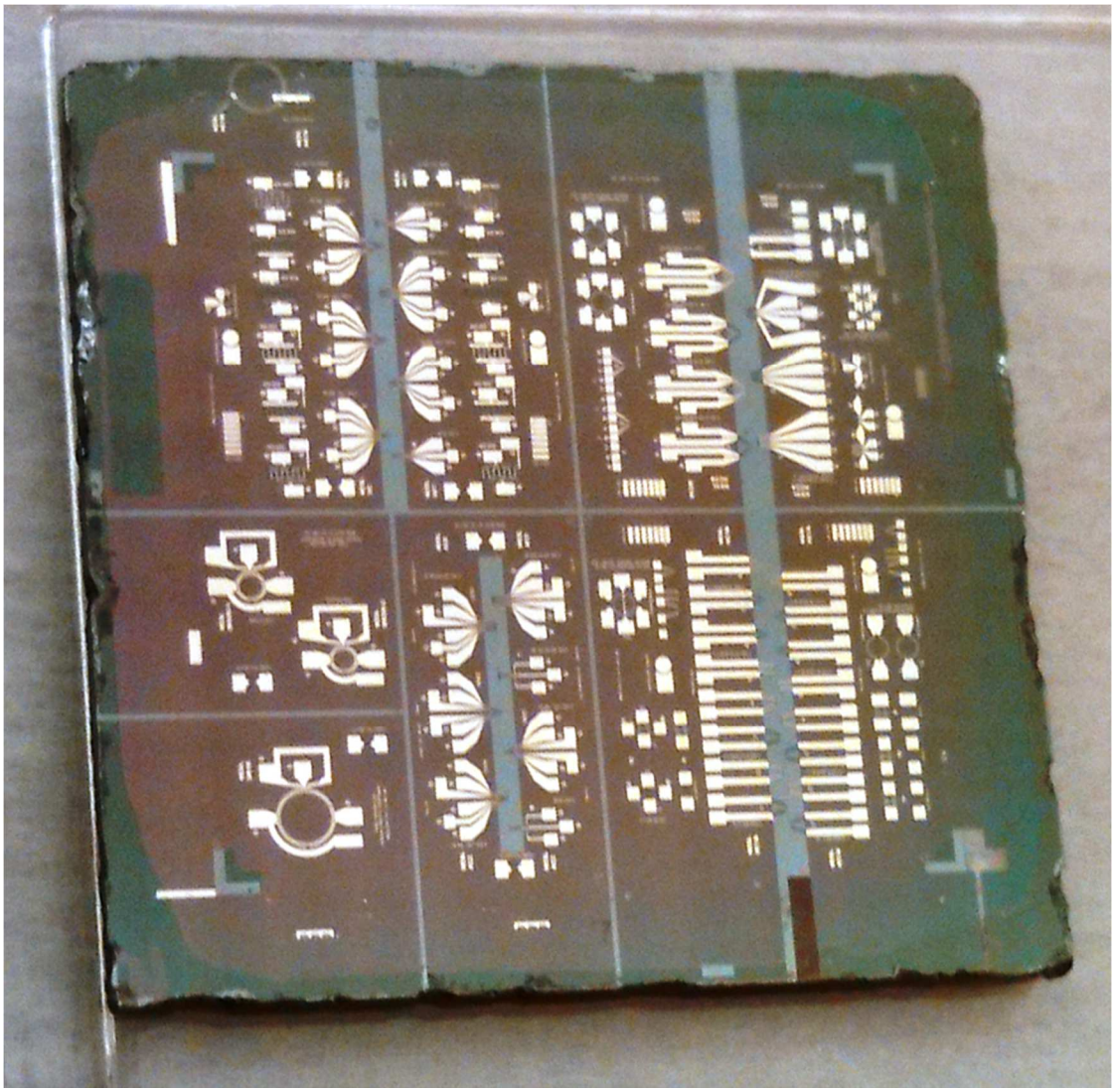

Figure 2.16 Optical image of the entire top outline

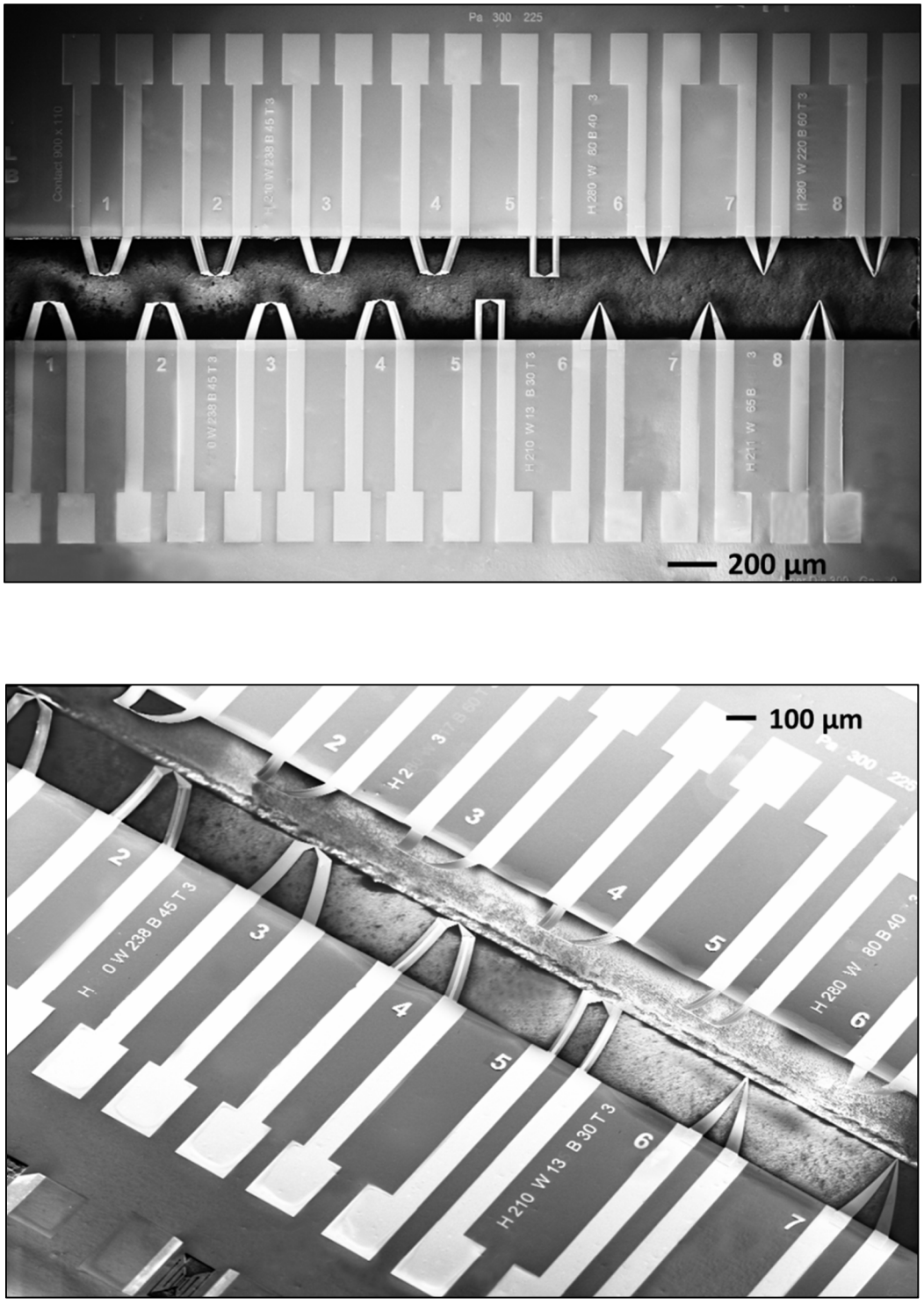

Figure 2.17 SEM image of single channel microcantilever heaters, (top) from top; (bottom) from an angle.

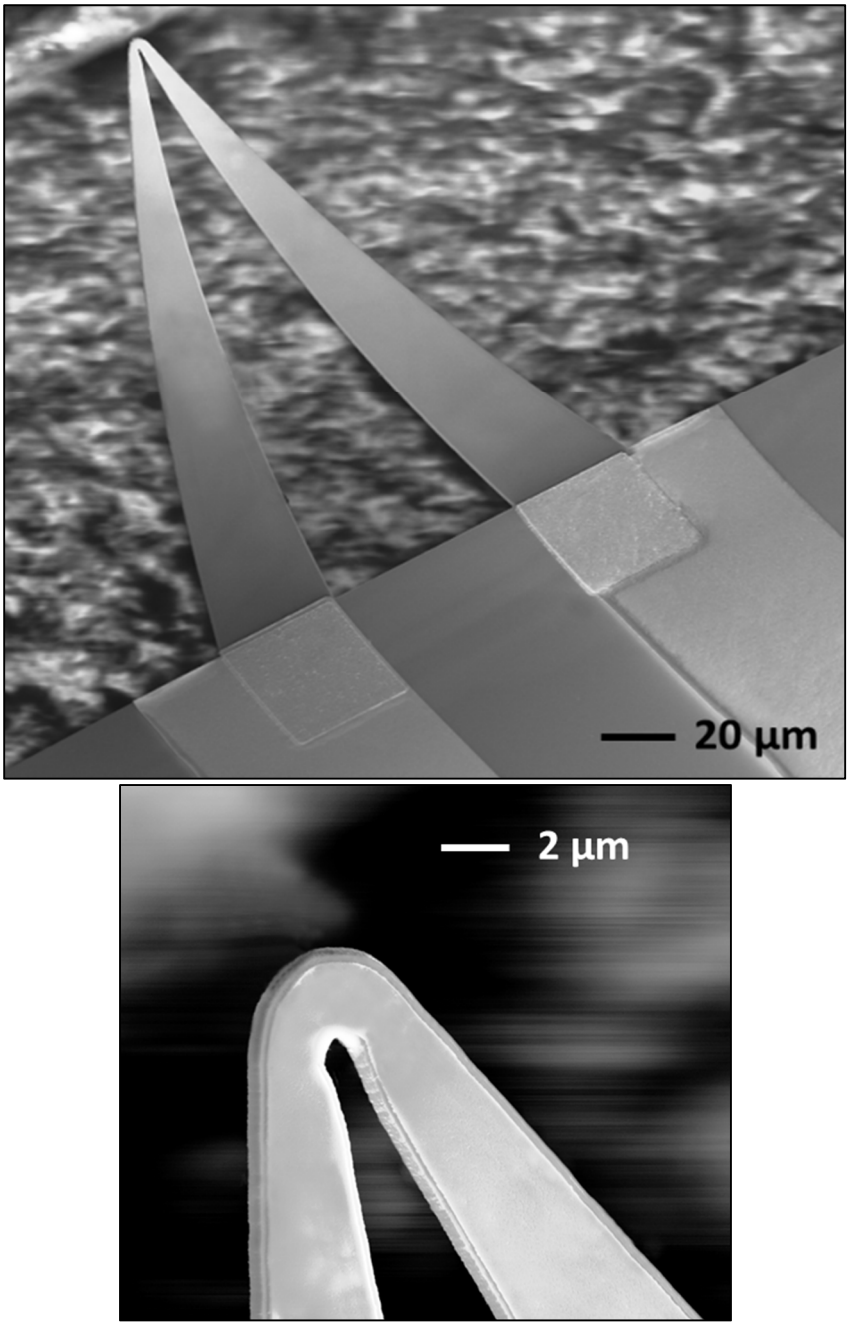

Figure 2.18 SEM image of (top) single channel triangular microcantilever heater (SC-TMH); (bottom) close-up of the tip.

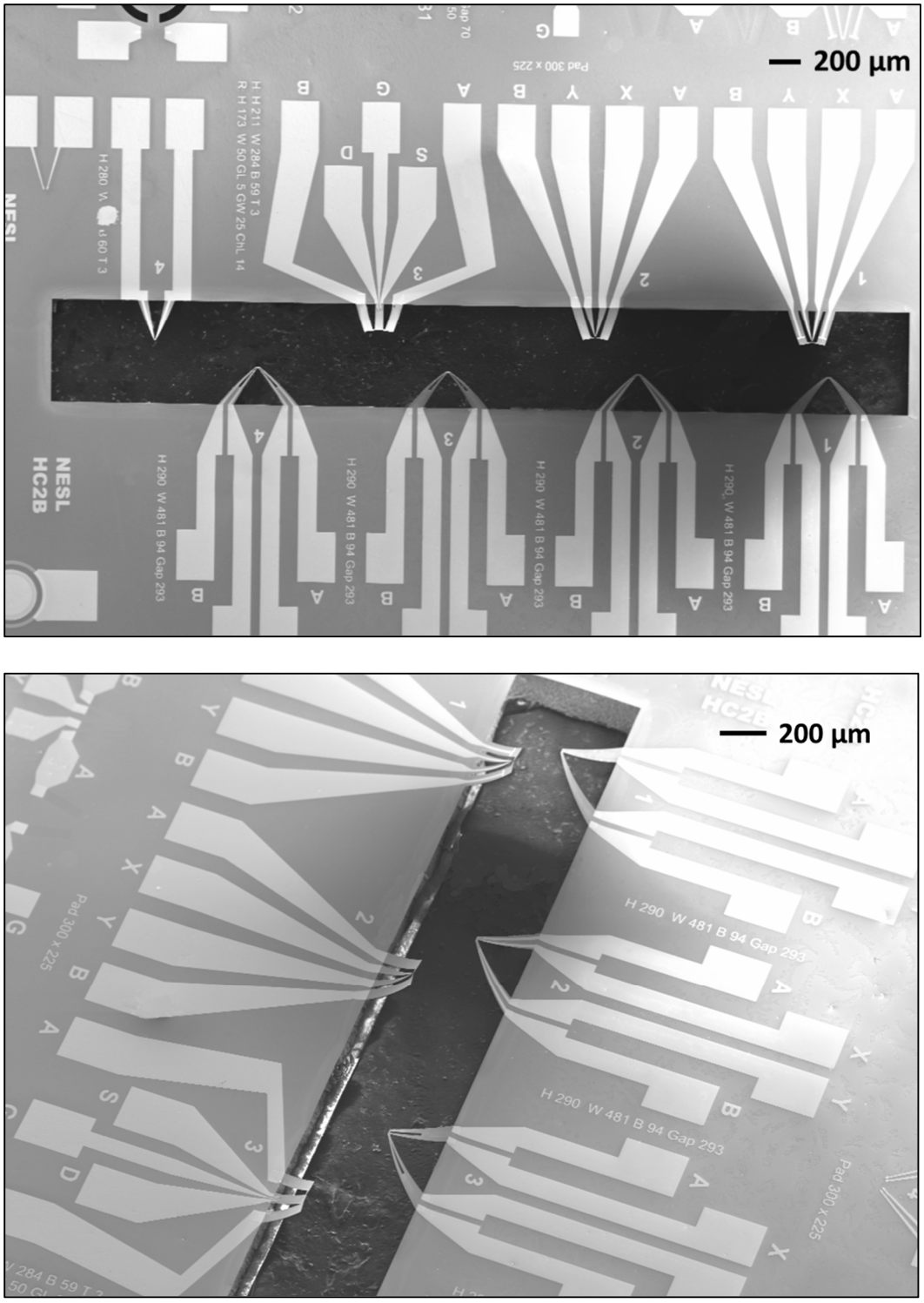

Figure 2.19 SEM image of dual channel and compound microcantilever heaters, (top) from top; (bottom) from an angle.

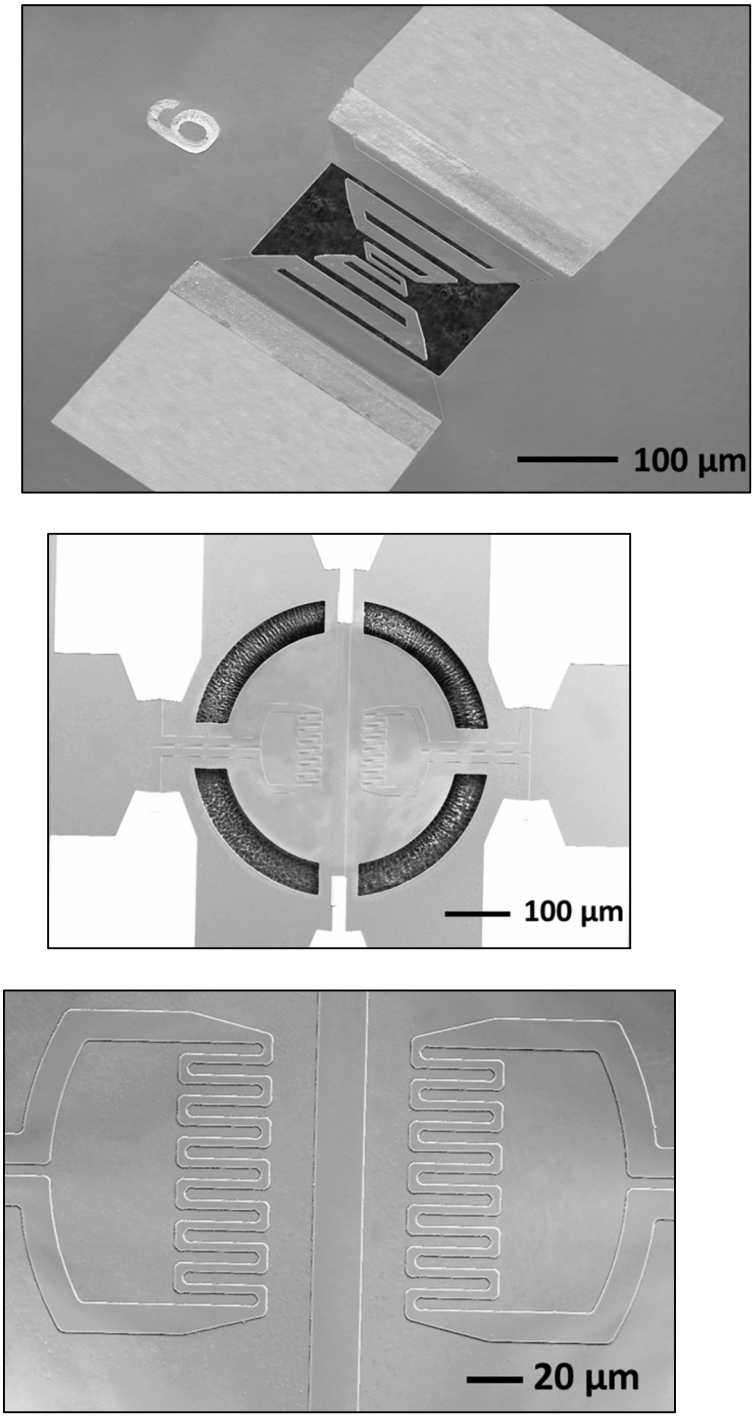

Figure 2.20 SEM image miscellaneous microheater elements: (top) zigzag microheater; (middle) Microhotplate; (bottom) close-up of the heating elements shown above.

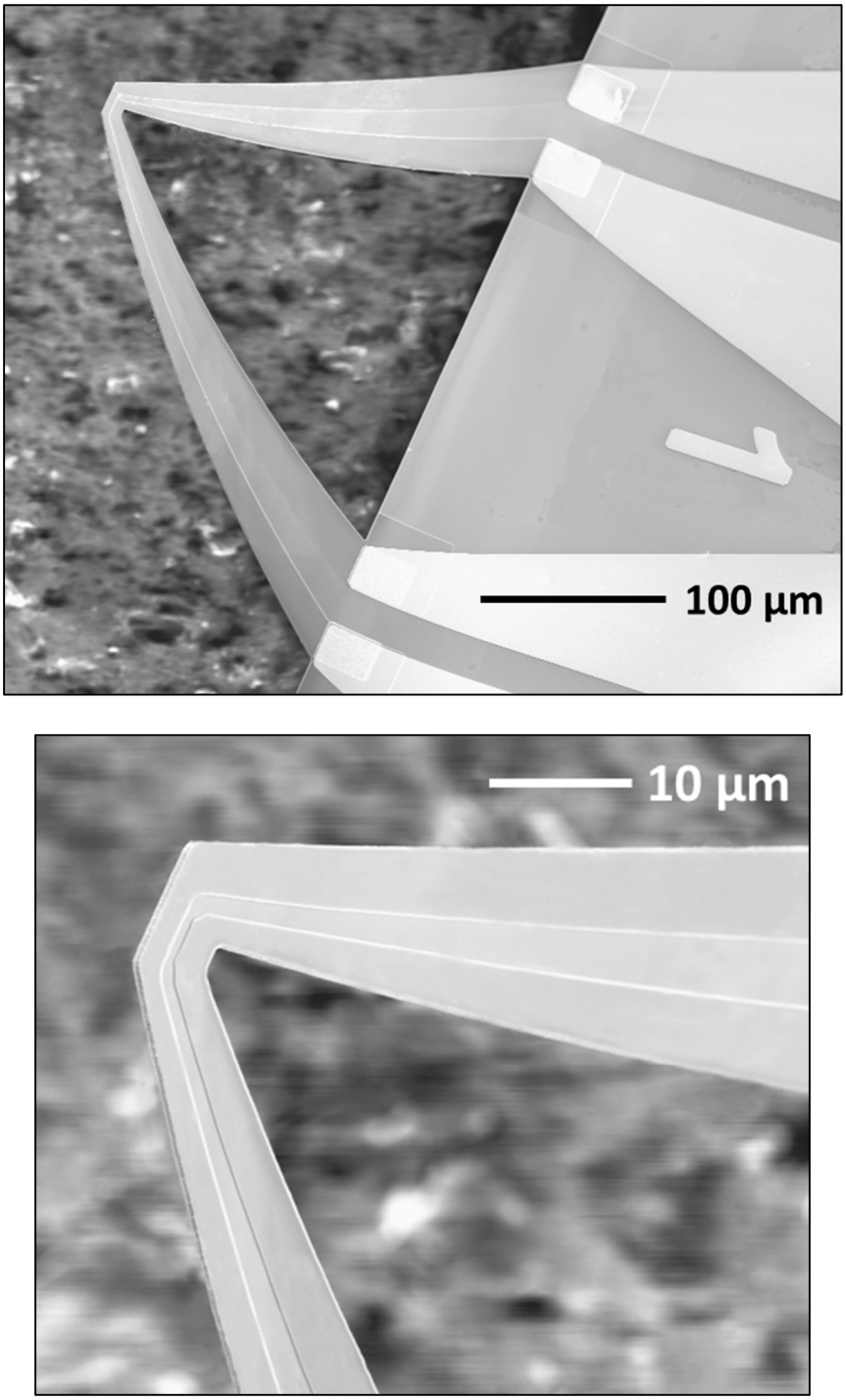

Figure 2.21 SEM image of (top) continuous tip dual channel microcantilever heater (CTDC-TMH); (bottom) close-up of the tip.

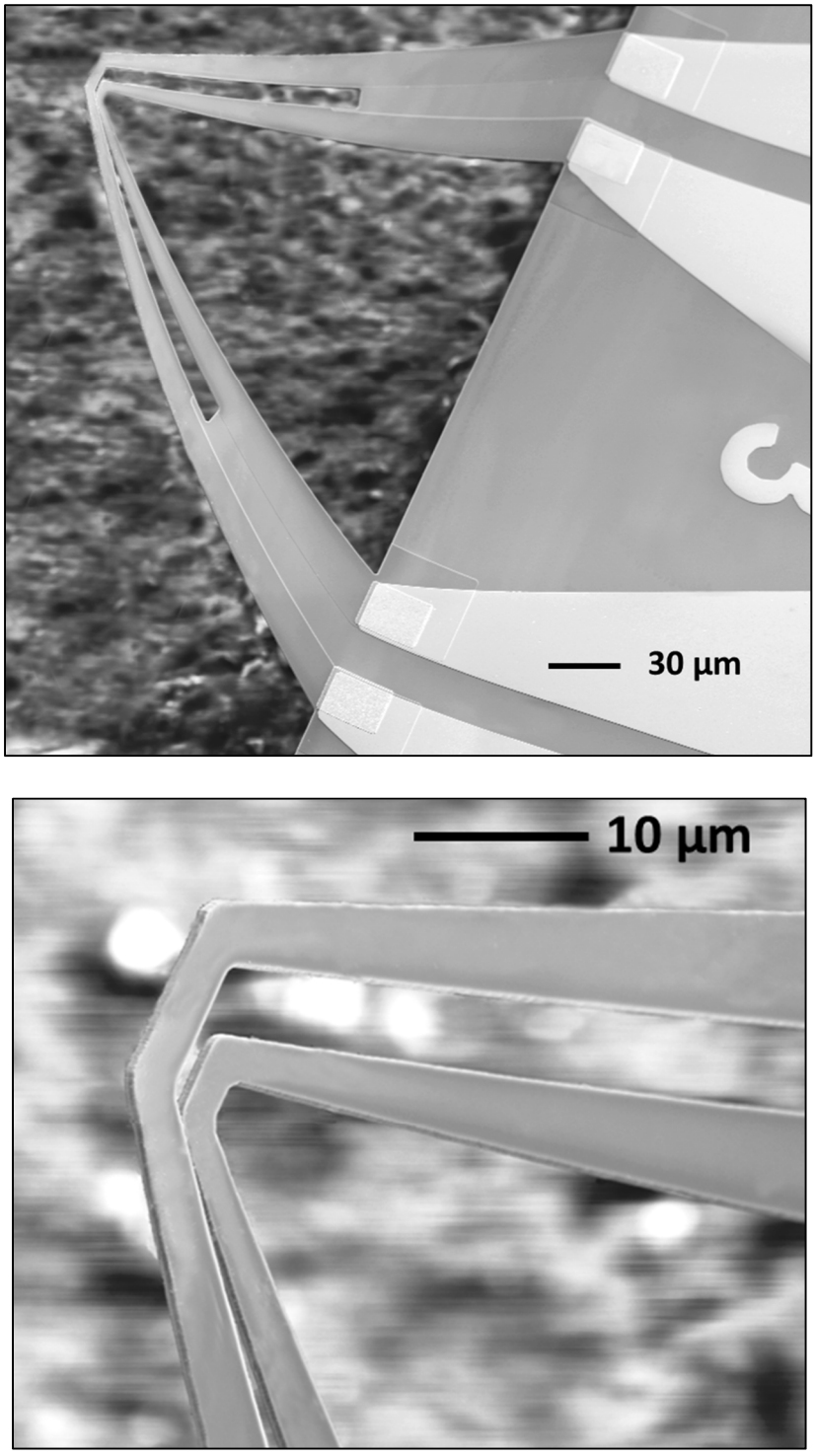

Figure 2.22 SEM image of (top) split tip dual channel microcantilever heater (CTDC-TMH); (bottom) close-up of the tip.

Chapter 3

Experimental Setup and Modeling

3.1 Electrical characterization and sensing setup

For electrical characterization, both Agilent B2902 and Keithley 2612A source measuring units (SMU) were used. While transmission line matrix (TLM) measurements were performed using a probe station, regular I-V characterization was performed on wire-bonded devices.

3.1.1 Sensing setup

Sensing experiments were done in a small chamber, which housed the wire-bonded sample. The chamber had an inlet and an outlet; wires from the device were taken out through a small opening near the outlet, which was stuffed with Teflon tape. A roughing pump along with a valve (V_3 in Figure 3.1) was connected to the outlet to quickly remove the analyte vapor out of the chamber whenever necessary. The inlet side of the chamber had a mixer assembly – consisting of a mixer junction with valves, a bubbler and two mass flow controllers. One mass flow controller was used to flow ultra-high purity (UHP) N_2, the other one was used to flow UHP N_2 into the bubbler to produce saturated vapor at room temperature. Both N_2 and vapor lines had two valves (V_1 and V_2, respectively) connected to them to control the flow of the gas/vapor and eventually merged into the mixer junction, which directed the vapor mixture into the inlet of the chamber. The purpose of using the mixer was to dilute saturated vapor with UHP N_2 to

obtain different concentrations, hence the flow rate of both MFCs were adjusted to get the desired ratio of N_2 and vapor. However, for low concentration (below 200 ppm), the N_2-vapor ratio could become extremely large, creating a backflow of N_2 from the mixer towards the bubbler. In order to avoid that, for such low concentrations, vapor flow rate was kept 5-20 times higher than its calculated value; but the flow valve V_2 was opened and closed in a pulsed manner to maintain a duty cycle less than 1. The higher flow rate with lower duty cycle effectively kept the average flow rate very low with reducing the probability of any backflow. After each sensing experiment, V_2 (vapor flow valve) was closed, but V_1 and V_3 were kept open. As a result, UHP N_2 flushed the chamber while the pump connected to V_3 quickly took out the residual vapor mixture from the chamber.

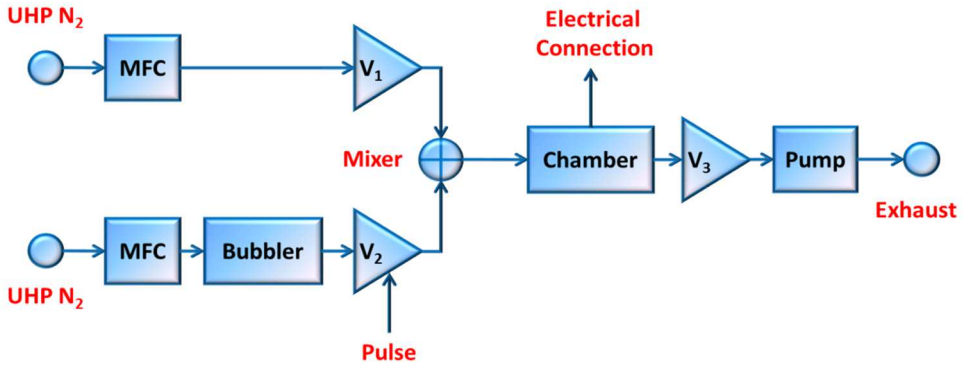

Figure 3.1 VOC sensing setup.

3.1.2 **Sensing Modes for SC-TMH**

Sensing characterization for single channel triangular microcantilever heater (SC-TMH) was done in two different biasing modes. In the first mode (steady-state mode), applied voltage bias was swept as a staircase function, where a fix dc bias was maintained for 20-30 s before changing the bias to the next level. During this time, current through the device was measured at a sampling frequency of 5-10 Hz. The whole process was run twice; first time in UHP N_2 environment to obtain the reference, and then the second time

in presence of the analyte vapor. The vapor flow was started right after the first run and sufficient time (up to 2 min) was given for the vapor concentration to reach the steady state before the second run was started.

The second mode (transient mode) used the same staircase function, but sampling frequency was higher (up to 25 Hz) to observe sharp changes in current. Also each step was of 90-120 seconds duration. Each bias step had three stages – UHP N_2 flow to obtain reference flow, vapor mixture flow to obtain time-resolved response of the device and finally, again UHP N_2 to observe recovery time. Since a single sweep was used to obtain the reference, sensor response and sensor recovery, second sweep was not necessary.

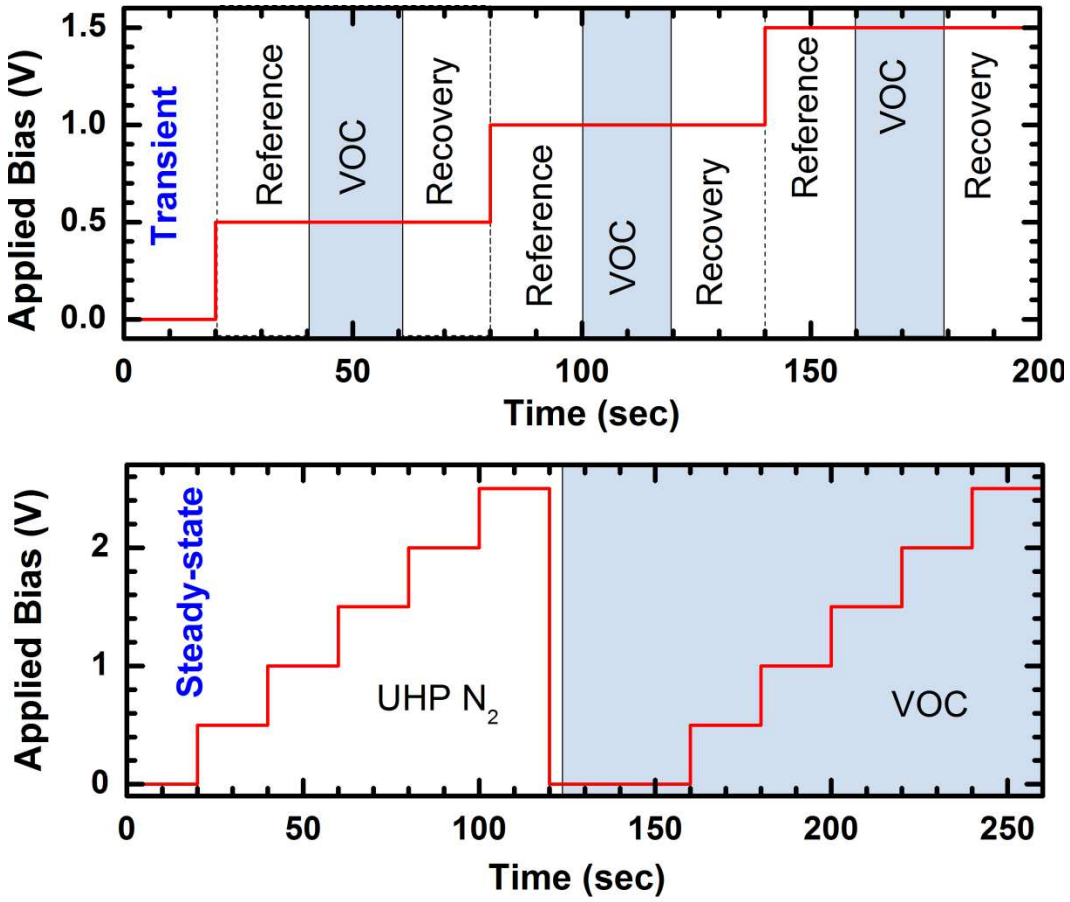

Figure 3.2 Bias and exposure configuration for SC-TMH sensing experiments: (top) Transient mode; (bottom) Steady-state mode.

3.1.3 **Sensing Modes for DC-TMH**

For dual channel triangular microcantilever heaters (DC-TMH), the inner arm (channel) was designated as the heater arm (channel) and the outer arm (channel) was designated as the sensor arm (channel). Only steady-state mode characterization was done for these devices, as transient response was expected to be of similar nature. Besides, since the response of DC-TMH comes from a combined contribution of both channels, time response may not be of great physical significance due to the uncertainty associated with the contributing factors.

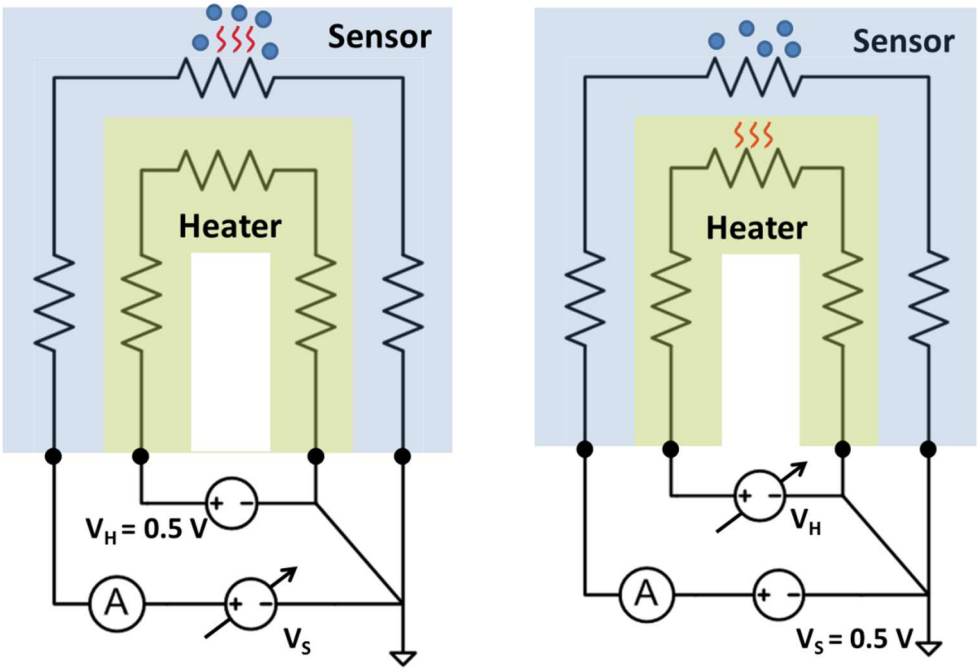

Figure 3.3 Steady-state operating modes of the DC-TMH: (left) Self-heating mode; (right) Secondary heating mode.

For any DC-TMH based sensing experiments, the sensor channel was used as the transducer. In other words, the response was recorded from the sensor channel only. However, either channel can be used as the source of heating; this results in two different

modes of steady-state operation (Figure 3.3). In the first mode, namely "self-heating mode", the sensor arm is biased at variable dc bias, just like SC-TMH devices. The heater arm is biased at a fixed low dc bias (~0.5 V), although it does not affect the response of the sensor channel.

In the second mode, called "secondary heating mode", the sensor arm is kept at a fixed low dc bias (~0.5 V) while the heater arm is biased at variable higher dc voltages. Here the sensor channel does not experience any significant self-heating, but still becomes hot due to the Joule heating on the heater arm. Therefore, the behavior of the sensor arm is thermally modulated by the heater arm, making it analogous to a three-terminal electronic device.

3.2 Thermal characterization setup

The temperature of the micro cantilever heater under a voltage bias was determined using Raman spectroscopy and infrared thermal microscopy. Raman spectroscopy was performed to measure the local temperature of the cantilever with electrical excitation.

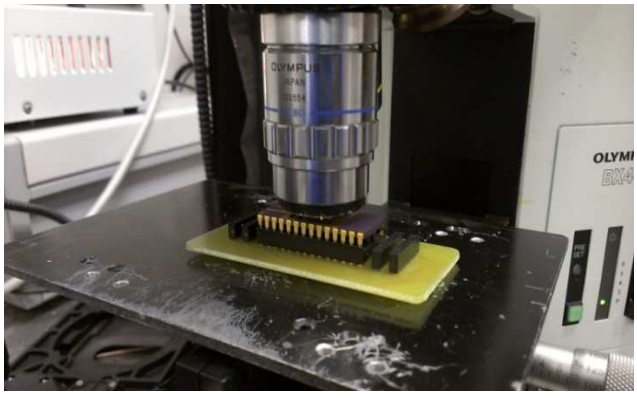

Figure 3.4 Experimental setup of Raman spectroscopy for measuring the temperature of tapered V shaped heated cantilever.

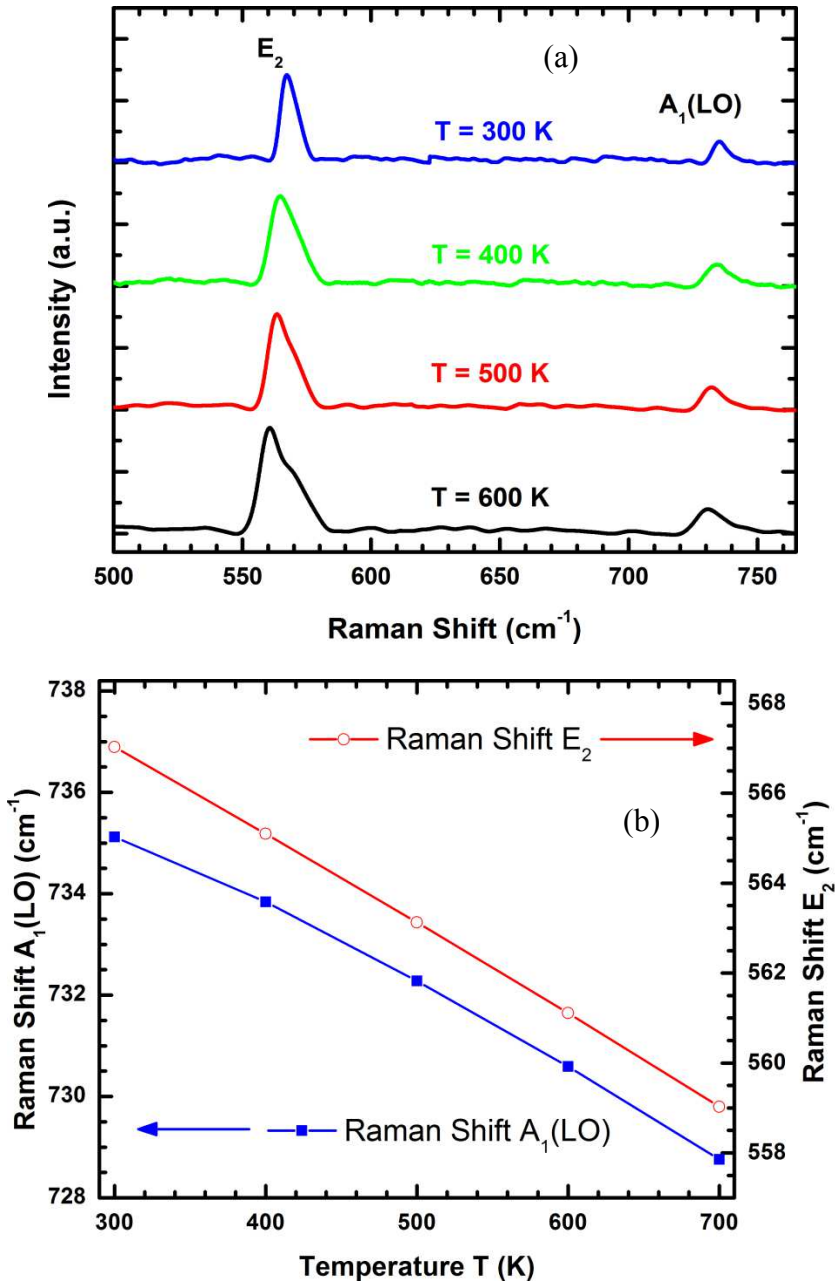

Figure 3.5 (a) Raman spectra of the heated cantilever for 300, 400, 500 and 600 K temperature on the hot plate. E_2 Peak becomes wider as temperature increases. (b) Shift in E_2 and A_1(LO) peaks towards lower wave number as temperature goes up.

3.2.1 **Raman characterization setup**

In this work a micro-Raman setup by Olympus was used. The sample excitation utilized a 632 nm HeNe laser while the collection was performed with an 800 cm^{-1}

spectrometer and an 1800 mm^{-1} grating. The slit was set at 200 μm to maximize the spectral resolution. An 80x objective was used to collect the Raman signature of the devices which provided a focal spot of 2 μm.

The effects of temperature on the phonon energy measured by Raman scattering are primarily due to the thermal expansion of the lattice, thus a downshift of phonon frequency with temperature is observed. In our experiments, a micro cantilever chip was mounted on a temperature calibrated miniature hotplate and heated up to different temperatures. Raman spectroscopy was used on different areas of the cantilever to obtain the E_2 and A_1(LO) peaks at those temperatures. Multiple readings were taken at different regions of the cantilever to check the uniformity of the data and the average peak values were taken for each temperature. Figure 3.5(a) shows the Raman spectra of the micro cantilever for four different temperatures. Here we see that as the temperature increases, E_2 peak becomes wider and both E_2 and A_1(LO) peaks shift towards lower wave number. Figure 3.5(b) shows the peak shift for E_2 and A_1(LO) with change in temperature.

3.2.2 **IR microscopy setup**

An Inframetrics PM280 Ultra Cam infrared camera (Figure 3.6), fitted with microscopic lens, was used to read the apparent temperature of the cantilever surface. The emissivity of the camera was then adjusted to match the temperature of the camera readout with the hotplate temperature. It was found out that an emissivity of 0.43-0.56 gave the best match within a temperature range of 300-700 K. The emissivity could be approximated as a linear function of temperature, so we took all IR readings at a constant emissivity of 0.5 and then corrected the resulting data using an interpolation function that

correlated the apparent temperature with actual temperature, taking the variation of emissivity into account.

Figure 3.6 Infrared (IR) thermal microscopy setup.

3.3 Simulation model

In order to explain various experimental results, a theoretical model based on heat transfer and Joule heating was developed. The framework of the model was based on the following equations for heat transfer (Equation (1) and Equation (3))[27] and Joule heating (Equation (2)) which were solved simultaneously and iteratively using finite difference method in MATLAB.

$$\rho_d C_p \frac{\partial T}{\partial t} + \boldsymbol{\nabla} \cdot (-K_c \boldsymbol{\nabla} T + \mathbf{u}\rho_d C_p T) + Q_{vap} = \frac{1}{\rho(T)} |\boldsymbol{\nabla} V|^2 \quad (1)$$

$$-\boldsymbol{\nabla} \cdot d\left(\frac{1}{\rho(T)} \boldsymbol{\nabla} V - J_e\right) = 0 \quad (2)$$

$$\mathbf{n} \cdot (K_c \boldsymbol{\nabla} T) = q_0 + h(T_{inf} - T) + \varepsilon\sigma(T_{inf}^4 - T^4) \quad (3)$$

Equations (1) and (2) were solved for different domains of the system, whereas (3) was used as a boundary condition at the interface of the solid and surrounding air

domains. Here, ρ_d = material density, C_p = heat capacity, T = absolute temperature, K_c = thermal conductivity, Q_{vap} = heat loss due to evaporation of analyte molecules (when applicable), J_e = electrical current density, V = potential profile, $\rho(T)$ = electrical resistivity as a function of temperature, **n** = unit vector normal to the interface, d = thickness of the domain, q_0 = heat source inside the domain, h = temperature dependent coefficient of convection for air,[26] T_{inf} = temperature far away from the cantilever, ε = emissivity of the solid surface, σ = Stefan-Boltzmann constant.

The temperature dependence of the electrical resistivity was modeled using I-V characteristics. At a given low voltage bias (~0.1 V), total resistance R was obtained. Then the entire device was divided into small segments of length Δx along the path of current conduction. At any given position x, the width of the channel W(x) was obtained from the SEM image of the cantilever. If the thickness is given by d, then resistivity ρ is given by,

$$\rho = \frac{R}{\sum \frac{W(x)d}{\Delta x}} = \frac{R\Delta x}{d\sum W(x)} \tag{4}$$

A chip, not bonded to a chip carrier, was mounted on a temperature calibrated hotplate and micro positioner probes were used to make electrical contact. The hotplate was heated to different temperatures up to ~450 ºC and resistivity was obtained for each temperature. Since the whole device was heated uniformly, resistivity was same everywhere. Then the following empirical relation was obtained (Figure 3.7) –

$$\rho(T) = -1.44 \times 10^{-4} T^2 + 0.144\,T + 1.037 \tag{5}$$

If the temperature profile along the cantilever arms is known (from Raman or IR imaging), that can be used to obtain the local resistivity profile. This profile can also be calculated theoretically using the heat transfer and Joule heating.

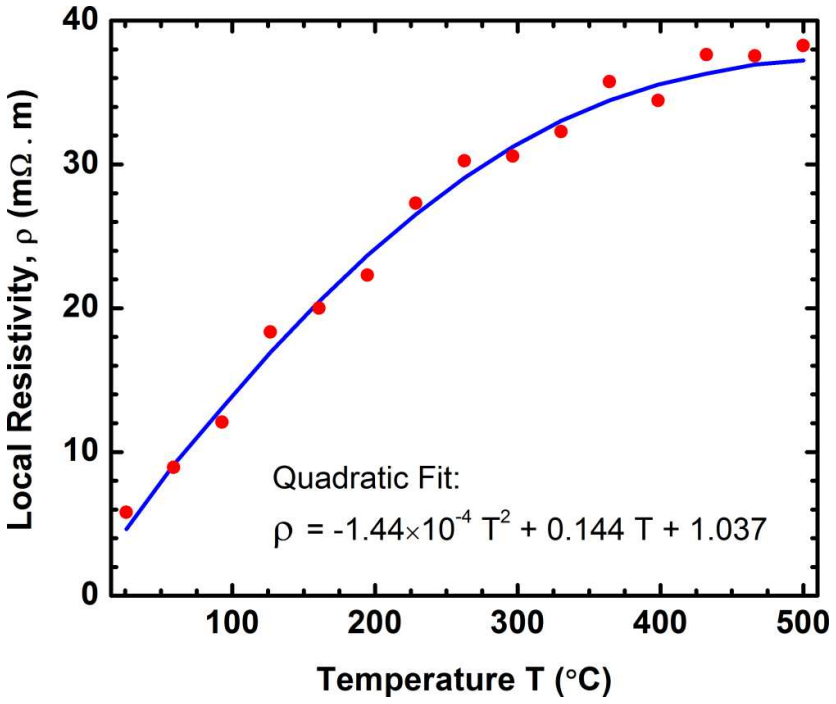

Figure 3.7 Variation of local resistivity as a function of temperature.

Since at very low concentration (in parts per million range or below) partial pressure of analyte molecules become very low, they can be considered as ideal gases; and therefore, kinetic theory of gases can be applied to calculate the amount of latent heat (Q_{vap}) taken away per unit of time from a heated surface of area A_h, by the molecules.

From the kinetic theory of gases, the number of molecules colliding with a surface of unit area per unit time is given by

$$\frac{dN}{dt} = \frac{1}{4} n v_{rms} \tag{6}$$

where,

$$n = \frac{P}{kT} \tag{7}$$

$$v_{rms} = \sqrt{\frac{3kT}{M}} \tag{8}$$

n is the number of molecules per unit volume and v_{rms} is the root means square velocity of molecules of mass M at temperature T. k is Boltzmann's constant (1.38×10^{-23} JK^{-1}). P is the pressure which, for a dilute gas, is given by the product of partial pressure P_p and fractional concentration C,

$$P = P_p C \tag{9}$$

Finally, the latent heat taken away due to the vaporization of condensed VOC molecules from a heated surface of area A_h per unit time is given by

$$Q_{vap} = K_{vap}\left(A_h \frac{dN}{dt}\, M\right) \frac{\Delta H_{vap}}{N_A} \tag{10}$$

where, ΔH_{vap} = molar latent heat of evaporation, N_A= Avogadro's number (6.023×10^{23} molecules/mol), K_{vap} is an empirical fitting parameter that is determined from experimental results. The term in the parenthesis in (10) gives the total mass of VOC molecules interacting with the heated surface. After substituting the parameters in (10) from (6)-(9), the final expression for Q_{vap} is found out to be

$$Q_{vap} = \frac{1}{4} K_{vap} A_h P_p C \frac{\Delta H_{vap}}{N_A} \sqrt{\frac{3M}{kT}} \tag{11}$$

The empirical parameter K_{vap} is required to match the response of a device to a particular VOC of a certain concentration. It is in general a function of the dipole moment and concentration of an analyte, applied bias across the device and the physical dimensions and nature of the device surface.

Chapter 4

Results and Discussions

4.1 Electrical Characterization Results

The I-V characteristics of the SC-TMH are shown in Figure 4.1 where a linear low bias and a non-linear high bias region can be clearly identified. Because of the significant self-heating of the device, current is generally observed to decrease at higher biases (> 5.5 V) as tip resistance increases rapidly with rise in temperature. Figure 4.2 shows >400% change in resistance (from 13 to 67 kΩ) as the bias changes from 0 to 15 V, with a power dissipation of 3 mW at 15 V.

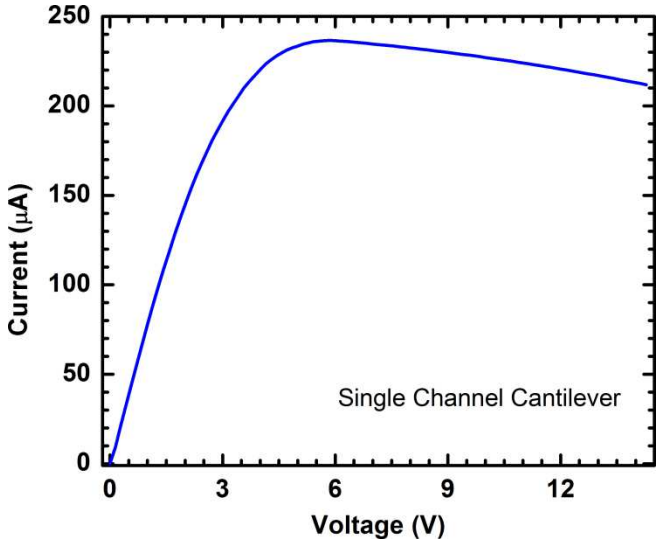

Figure 4.1 I-V characteristics for a SC-TMH device.

TLM is used to determine the quality and characteristics of the metal-semiconductor contact. The metal contacts must supply the required device current. It

should also have a voltage drop across the contact that is small compared to the voltage drop across the active device region. The metal contacts are either referred to as Schottky or Ohmic based on a distinctly non-linear or linear I-V characteristic, respectively where an ohmic contact is desirable. The TLM test measures different electrical parameters including the contact resistance, transfer length and sheet resistance. Figure 4.3 shows a portion of the TLM pattern before and after the Rapid Thermal Annealing (RTA). The separation of the pads were 5, 10, 15, 20, 25 and 30 µm and the dimension was 150 µm by 300 µm. As seen from Figure 4.4 the total resistance has a fairly linear relationship with the contact distance. Generally the resistance versus contact distance has a linear relation in the form,

$$R = \frac{R_{sheet}}{Z} d + 2R_C \tag{12}$$

where, R is the total resistance between two adjacent contacts, R_{sheet} is the sheet resistance of the channel, and R_C is the total contact resistance of each contact. Applying a linear fit for the graph in Figure 4.4 we get the parameters given in Table 4.1.

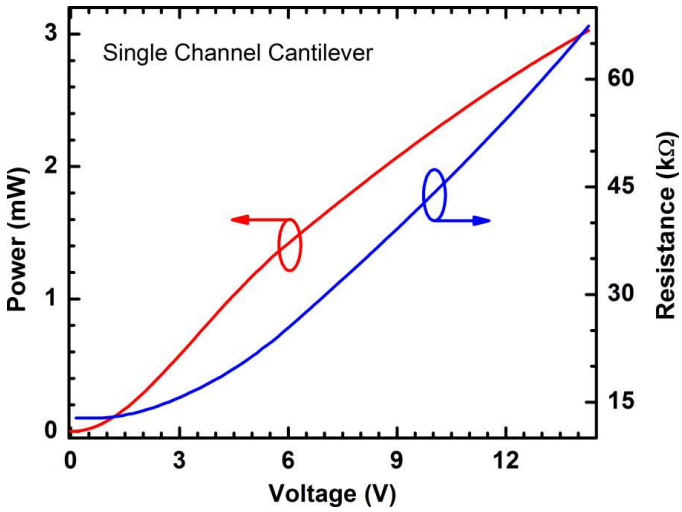

Figure 4.2 I-V characteristics for a SC-TMH device.

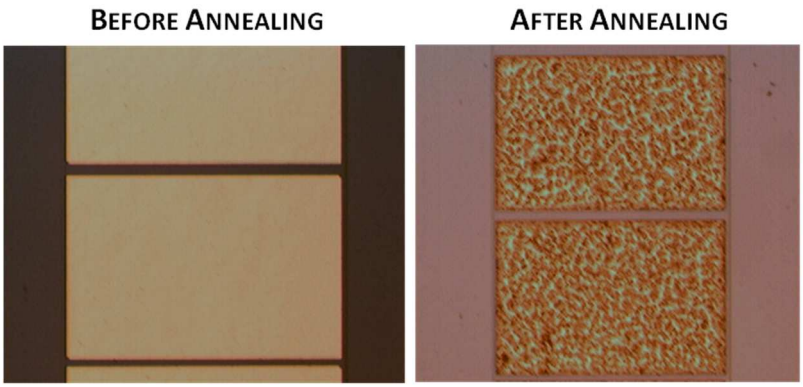

Figure 4.3 TLM contact pads, before annealing and after annealing

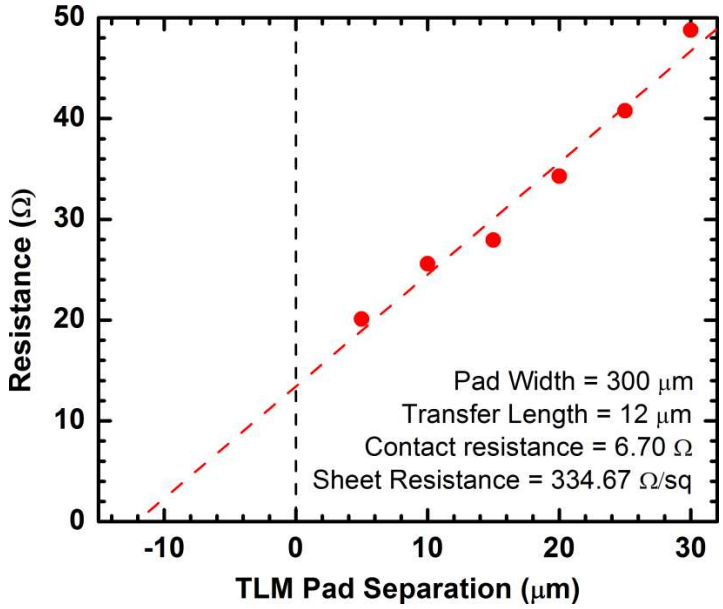

Figure 4.4 The total resistance between contacts as a function of distance

Table 4.1 Calculated parameters from the TLM test

Width, W (μm)	Contact resistance, Rc (Ω)	Sheet resistance, Rsh (Ω/□)	Transfer length, L_T (μm)	Contact resistivity, ρc (Ω-cm^2)
300	6.70	334.67	12	4.82E-04

As shown in Figure 4.4 x-axis intercept is $2L_T$ where L_T is the transfer length. Transfer length is the distance below the contact where the applied voltage gets attenuated by $1/e$ factor (e = 2.718). Moreover, the specific contact resistivity, ρ_c can be expressed as,

$$\rho_c = L_T^2 R_{sheet} \tag{13}$$

All the calculated value found out from our TLM test is shown in Table 4.1. As observed from the calculated values the contact resistivity is low which shows that the contacts in these TLM patterns are ohmic.

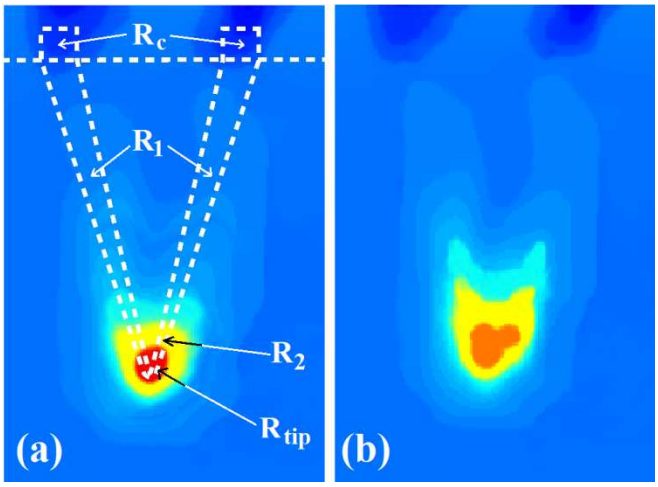

Figure 4.5 IR microscopy image of a first generation SC-TMH device with 50 V dc bias. (a) In air; (b) In 2000 ppm isopropanol vapor.

4.2 Sensing and Thermal Characterization Results

4.2.1 Thermal Characterization of SC-TMH

In, temperature profile along the length of a first generation SC-TMH is shown using infrared (IR) thermal microscopy Figure 4.5. It should be noted that, most of the reslts shown in work are from the second generation of devices, which were more

sensitive and energy-efficient. The first generation devices had lower conductivity, hence up to 50 V dc bias had to be applied for various sensing experiments. However, certain measurements could only be done on the first generation devices only; therefore in very few cases those results are presented. Here, the tapered shape of the cantilever gives rise to a sharp temperature variation along the arms, especially near the tip, as observed from the infrared (IR) image of the cantilever. To determine the impact of analyte flow on the temperature profile of the cantilever arms, IR images of the cantilever with and without the presence of isopropanol were recorded. In Figure 4.5(a), the cantilever (dashed line) is shown at 50 V bias without any analyte flow, the red region at the tip is the hottest spot with a temperature of about 330 ºC. Figure 4.5(b) shows the cantilever image with 2000 ppm molar concentration of isopropanol vapor under the same 50 V bias.

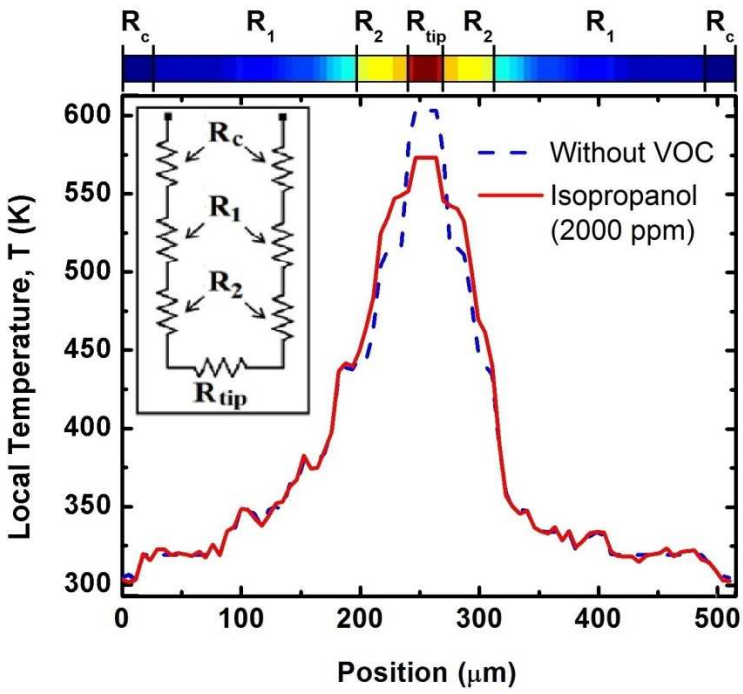

Figure 4.6 Line scan along the cantilever arm shown in the IR microscopy image of a first generation SC-TMH device with 50 V dc bias in Figure 4.5. Inset shows an equivalent circuit model of the cantilever.

Figure 4.6 shows a line scan depicting average temperature variation along the arms of the cantilever. Here we see that the peak temperature at the tip is reduced by ~30 ºC in presence of 2000 ppm of isopropanol vapor, while the temperature profile becomes wider. Interestingly, the side arms adjacent to the tip area exhibit an increase in temperature by ~20 ºC. It is interesting to note that the current in our TMH sensor increased, i.e. the overall resistance decreased, in presence of isopropanol vapor. Thus, any exothermic reaction between the VOC and air can be ruled out in contrast with hot bead pellistors.[3]

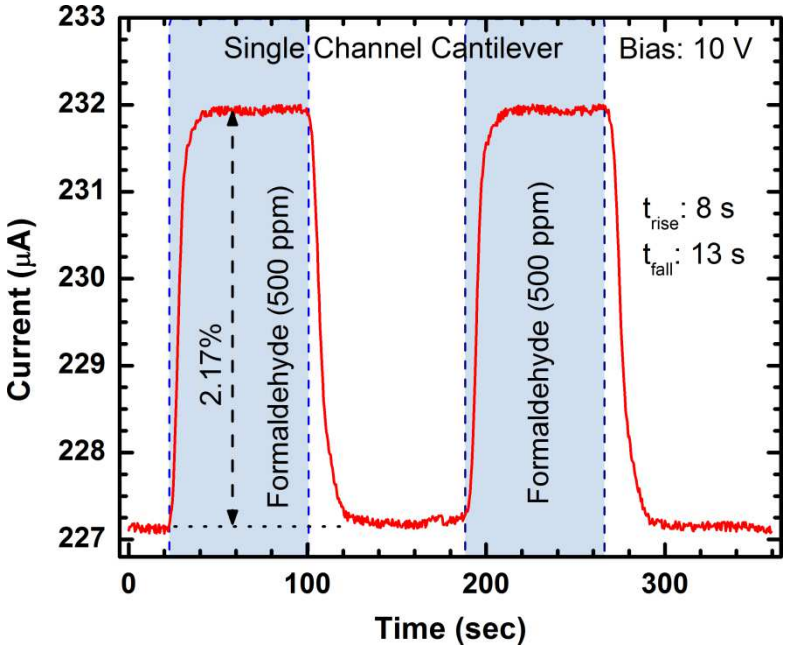

Figure 4.7 Response of a SC- TMH sensor to 500 ppm of formaldehyde at 10 V dc bias. Current magnitude changed by 2.17% with rise time and fall time of 8 s and 13 s respectively. Two sensing cycles are shown here to demonstrate repeatability.

4.2.2 **VOC Sensing Using SC-TMH**

The response of a second generation SC-TMH upon exposure to 500 ppm molar concentration of formaldehyde vapor is shown in Figure 4.7, where the current changes from 227.1 to 231.9 μA (2.17% change) in about 10 s, at a device bias of 10 V. Two

consecutive cycles to demonstrate complete recovery and repeatability of the device. The rise time, defined by the time taken by the current to go from 10% to 90% of the steady state value, is found to be ~8 s. The fall time (defined as the time for the maximum signal to decay from 90% to 10% of its value) was found to be ~13 s. Comparable rise and fall times were observed for other analytes as well. No change in current was observed for water vapor, up to 5 V of bias.

Considering the temperature profiles shown in Figure 4.6, we propose a model explaining the response of the TMH sensor in presence of organic vapors. To facilitate our model description, we assume the overall cantilever resistance to consist of several lumped resistors connected in series, each describing the resistance of a specific zone along the arms of the cantilever. These resistances are shown in Figure 4.5(a) and Figure 4.6 as R_c (contact resistance), R_1 (side arm resistance), R_2 (resistance near the tip) and R_{tip} (resistance of the tip region). At lower biases (< 1 V), the device exhibits an I-V with almost constant resistance [Figure 4.1], indicating the absence of any significant self-heating. At higher biases (> 1 V), I^2R loss increases, causing the tip temperature and resistance R_{tip} to go up. However, the temperatures of R_c and R_1 do not increase as much as R_{tip} with an increase in bias voltage, therefore, these resistances do not change significantly. If a volatile vapor is injected into the test chamber, the vapor molecules will initially tend to condense in close proximity of the cantilever, but the heated tip region will cause their immediate evaporation. This results in a net loss of thermal energy from this region (defined by resistance R_{tip}) causing its temperature to become lower. The regions of the side arms away from the tip (defined by resistances R_2 and R_1) do not participate in rapid evaporation of analyte molecules, so the thermal energy loss due to

the evaporation of VOCs is not significant there. Since the whole device is under a constant voltage bias, reduction in R_{tip} will cause an increase in voltage drop across R_1 and R_2 (R_c is likely to be much smaller and the voltage drop across it can be neglected). Since R_2 can be expected to be larger than R_1 at high temperature, the voltage drop across it is more significant, resulting in a higher temperature rise in that region and consequently larger increase in resistance. Therefore, the total resistance between the arms of the cantilever is affected by the opposite changes in R_{tip} and R_2, in agreement with the IR image line scan shown in Figure 4.6 under isopropanol flow.

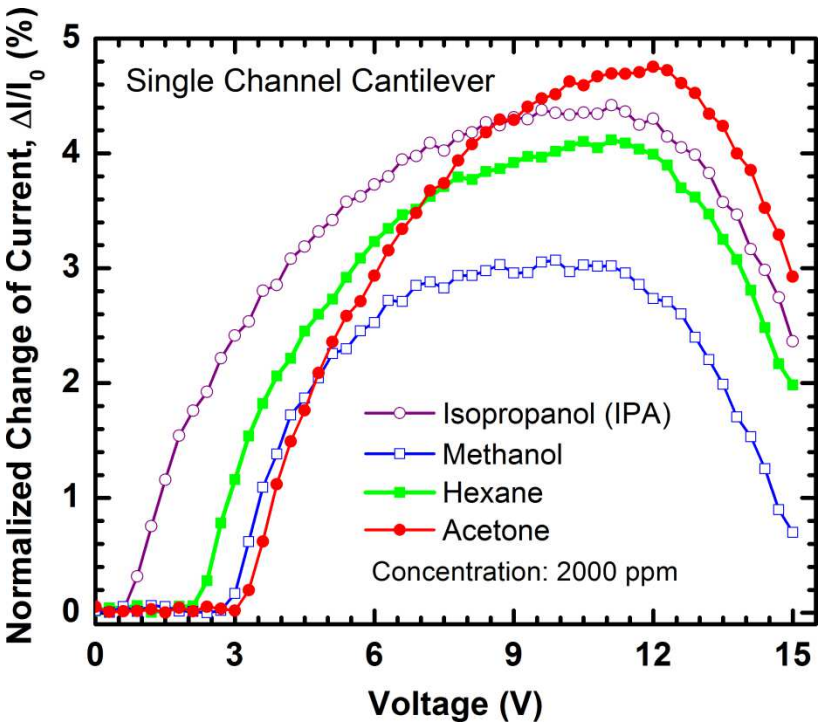

Figure 4.8 Normalized change of current (%) for the SC-TMH device at different dc biases and with analyte concentration of 2000 ppm.

At a moderate bias voltage, i.e. ~0.5-0.8 V, even if a VOC vapor actually causes a reduction in R_{tip} (by reducing temperature), the increase in R_2 (due to increase in temperature) can compensate for it, since the overall rise in temperature is still low at that

bias. Thus, the current can remain unchanged even in presence of a VOC vapor at lower biases. However, as the bias voltage is increased for a given VOC flow, depending on the extent of the temperature drop of R_{tip} region (which correlates with the molar latent heat of evaporation, ΔH_{vap} of the VOC), a threshold voltage bias can be reached where the reduction in R_{tip} would be more than the increase in R_2, thus an increase in current would be observed. Existence of such a threshold voltage, and its dependence on ΔH_{vap}, has been experimentally observed, and are shown in Figure 4.8.

Table 4.2 Dipole Moment (μ) and Latent Heat of Evaporation (H_{vap}) of VOCs

Analyte	μ (D)	H_{vap} (kJ/mol)
Hexane	0.08	31.5
Toluene	0.43	32.3
Isopropanol	1.66	45.4
Ethanol	1.69	38.6
Methanol	1.7	35.3
Acetone	2.85	30.5
Diethyl Ether	1.30	27.3
Trichloroethylene	0.81	34.6
Formaldehyde	2.33	24.3
Dimethylformamide	3.86	32.1

Figure 4.8 shows the percentage change in current caused by dilute vapor (2000 ppm molar concentration) of four different VOCs: isopropanol (IPA), methanol, hexane and acetone, as the applied voltage bias was varied from 0 to 15 V. Five readings were

averaged at each bias point and a 7-points moving average filtering was performed to ensure better consistency and noise reduction. Here we clearly see the existence of such threshold voltages. Also after 11 V, sensor response drops sharply due to two main reasons – (1) Convection flow at high temperature prevents analyte molecules from approaching the device surface, (2) Other means of heat transfer dominates over the heat loss due to VOC evaporation, reducing its effect on the device response.

From the measured data points, the approximate uncertainty in the threshold voltage was estimated to be ±0.05 V. As can be seen from Figure 4.8, each analyte corresponds to a distinct threshold voltage (V_{th}) below which it does not cause any noticeable change in current. In the present work, V_{th} is arbitrarily defined using a current magnitude change of 0.06% or higher (considering our noise level of 0.022% and a signal to noise ratio of >2.5) in presence of an analyte; however, for a low noise environment, it can be defined at a lower value as well. To determine the V_{th} from our measurements we use the following methodology; if within a voltage range of 0.1 V the change in current is at least 0.06% (in presence of an analyte vapor), then the mid-value of that voltage range is defined as V_{th}. The current response at V_{th} (also known as threshold response) is given by,

$$\frac{\Delta I_{th}}{I_0} = \frac{(I_{vap} - I_0)\big|_{V_{th}+0.1} - (I_{vap} - I_0)\big|_{V_{th}}}{I_0\big|_{V_{th}+0.1} - I_0\big|_{V_{th}}} \tag{14}$$

For any other voltage $V>V_{th}$, current response is given by,

$$\frac{\Delta I}{I_0} = \frac{(I_{vap} - I_0)\big|_V}{I_0\big|_V} \tag{15}$$

Here, I_{vap} and I_0 are the currents measured with and without analyte vapor, respectively. The same is also done for dry UHP N_2 instead of analyte to obtain the background response for the carrier gas (dry UHP N_2) and the noise signal, which was found to be within 0.022% over the entire bias range (0 to 15 V).

The threshold voltage for each analyte was observed to be very consistent over multiple sets of experiments performed in a period of more than six month utilizing several identical devices. To verify if a generic correlation indeed exists between ΔH_{vap} and V_{th}, as predicted by our model, threshold voltages of ten different analytes with latent heat varying over a wide range were determined (Table 4.2). The plot of V_{th} versus ΔH_{vap} is shown in Figure 4.9, where an excellent linear correlation is observed. This is in agreement with our proposed model (please refer to the explanation of Figure 4.6, where a correlation between V_{th} and ΔH_{vap} was predicted), and clearly indicates that such a well-defined correlation can be utilized to perform selective detection of VOC vapors from their unique threshold voltages. It should be noted here that the temperature of the tip (measured using the IR camera) at the threshold voltage was always lower than the auto-ignition temperature for all the ten VOCs studied, ruling out any combustion related effects. Also, as mentioned above, no effect of water vapor of similar molar concentration (2000 ppm) was observed even up to a bias of 5 V, which is much higher than the expected V_{th} of water (< 2 V) based on its ΔH_{vap} of 40 kJ/mol. This, therefore, rules out any interference from water vapor in realistic sensing environments.

To investigate any dependence of the V_{th} on analyte concentration, detection was performed with much diluted (down to ~50 ppm concentration) vapor of some of the VOCs. The V_{th} values were found to increase only by ~0.5 V as the vapor concentrations

were reduced 40 fold from 2000 to 50 ppm. As the analyte concentration is decreased, fewer molecules are able to interact with the cantilever, thus causing the V_{th} to increase. Although, the relatively small magnitude of change in V_{th} is unclear to us at this point, nonetheless, V_{th} is obviously an important parameter that can be utilized in a practical sensor to uniquely identify different VOCs over a specified range of concentration, especially in indoor environments.[28]

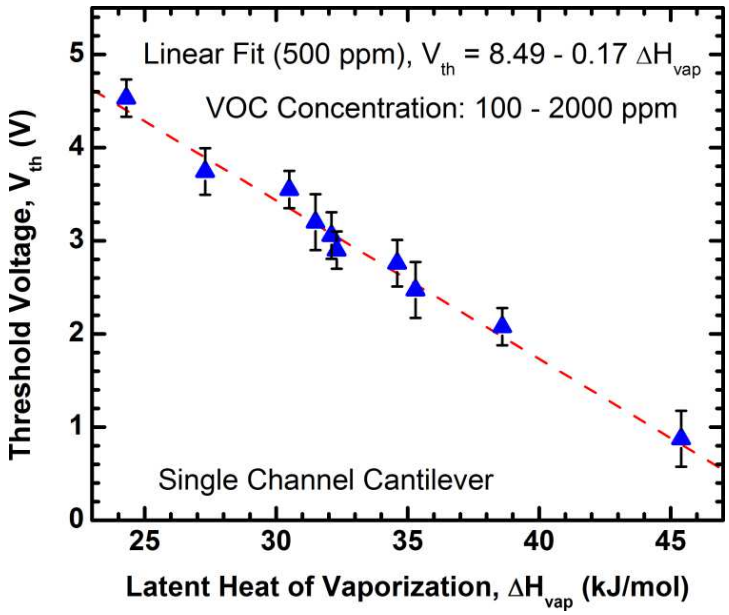

Figure 4.9 Dependence of threshold voltage of detection on latent heat of evaporation of VOCs. The error bars indicate the range of values recorded for different concentrations within a range of 100-2000 ppm. All threshold voltages are below 5 V.

In order to identify the threshold voltage, it is also important to observe the dependence of current magnitude change at the threshold voltage. In the post-threshold biasing region, more and more analyte molecules can interact with the heated cantilever tip as the effective area of the hot zone (corresponding to R_{tip}) increases with bias voltage. Increased temperature also increases the convection flow, creating a low pressure region in the vicinity of the heated tip of the cantilever. This causes faster circulation of analyte vapor around the cantilever tip resulting in more molecules to

interact with the tip per unit time. Therefore, just above the threshold voltage, for the same analyte concentration, current is mostly governed by the effective area of the heated tip region as shown in Figure 4.10, where the analyte with the lowest threshold voltage has the lowest threshold response because of the smaller effective area of hot zone at that voltage. Extrapolating all the curves towards low concentration gives a noise limited resolution of ~1.5 ppm. The threshold response is defined in (15).

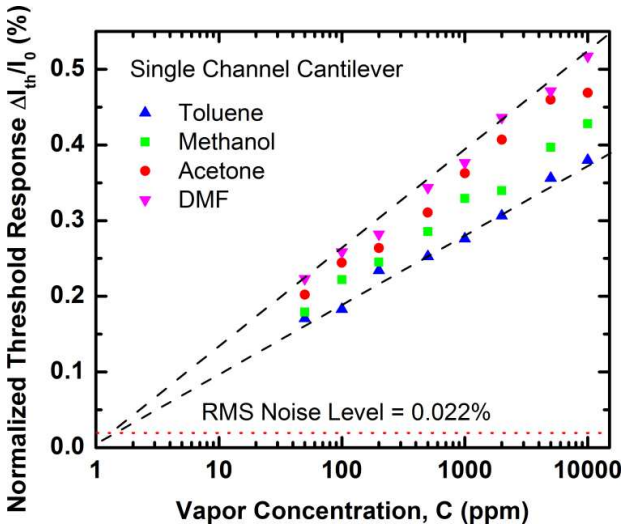

Figure 4.10 Detectability of threshold voltage at low concentration. The response at threshold voltage is determined using the equation given below. Extrapolating the threshold response vs. concentration curves, we find the noise limited resolution to be around 1.5 ppm with 0.022% being the rms noise magnitude.

Above the threshold voltage, percentage change of current in presence of a particular VOC depends on the concentration of analyte vapor. We define sensitivity of the sensor as the percent change in current for one decade change in analyte concentration; change in current is calculated at threshold voltage using (16). We denote this sensitivity by S, which is calculated using the following expression,

$$S = \frac{\left.\frac{\Delta I_{th}}{I_0}\right|_{C_2} - \left.\frac{\Delta I_{th}}{I_0}\right|_{C_1}}{\log\left(\frac{C_2}{C_1}\right)} \tag{16}$$

where C_2 and C_1 are the vapor concentrations ($C_2 > C_1$).

Table 4.3 Sensitivity, rise time and fall time for different analytes at threshold voltage.

Analyte	V_{th} (V)	Sensitivity, S (%/dec)	Rise Time (s)			Fall Time (s)		
			1000 ppm	500 ppm	50 ppm	1000 ppm	500 ppm	50 ppm
Toluene	2.9	0.0921	5.1	8.2	19.8	12.2	14.3	18.3
Methanol	2.5	0.0756	5.6	8.9	21.0	11.7	15.1	17.6
Acetone	3.6	0.1429	5.3	8.5	19.6	11.9	14.8	19.4
DMF	3.1	0.1297	5.2	8.4	20.4	12.4	15.3	18.7

Table 4.3 shows the sensitivity, rise and fall times of the SC-TMH sensor for 1000, 500 and 50 ppm concentrations of toluene, methanol, acetone and DMF vapors. We find that an analyte with a higher threshold voltage leads to higher detection sensitivity, which is also evident in Figure 4.10, where the slope of the fitted line is higher for such an analyte. Table 4.3 also lists the rise and fall times of the sensor for different analytes. It is observed that the rise/fall times are similar for all four analytes.

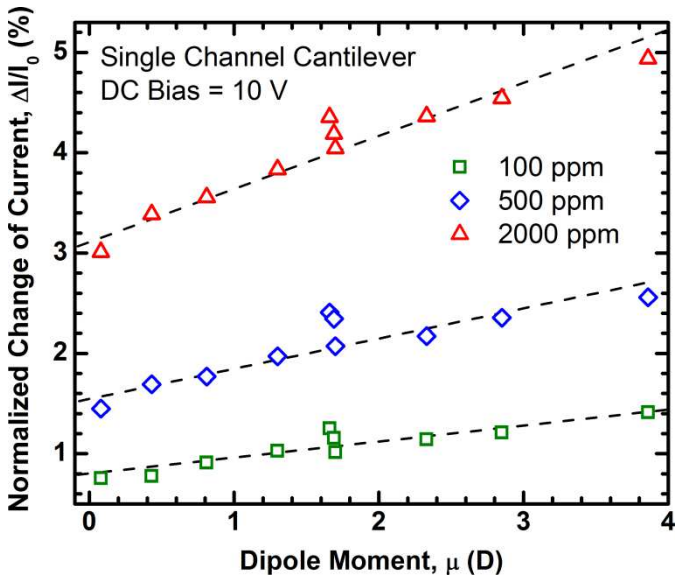

Figure 4.11 Normalized change of Current for three different concentrations, shown as a function of dipole moment.

4.2.3 **Effect of Polarization on VOC Sensing**

Since III-Nitrides have strong polarization properties, it is interesting to explore possible correlations between the magnitude of the molecular dipole moment of the analyte VOC and the magnitude of current change caused at a fixed applied bias. Figure 4.11 shows the percentage change in current for ten VOCs (measured at a constant bias of 10 V) plotted against their dipole moment. We find that as the dipole moment of the analyte VOC increases, the response magnitude also increases, which is expected since the molecules with higher dipole moment are expected to have stronger interaction with the highly polar AlGaN surface.[29] This would cause a larger change in tip temperature and hence in the overall magnitude of the current change. Although the physical mechanism of molecular interaction is unclear to us at present, it is possible that the polar AlGaN surface is responsible for attracting the polar VOC molecules toward it, (which is dependent on the dipole moment) and allowing them to condense to a certain extent. When the condensed molecules evaporate, the latent heat taken away (and hence the response magnitude) is therefore also proportional to the molecular dipole moment. For example, acetone, in spite of having a rather low ΔH_{vap}, still caused the largest change in current at 10 V, since its dipole moment is the highest among all the analytes studied. If multiple analytes have very similar dipole moments, the change in current depends on their latent heat of evaporation, which is clearly evident from Figure 4.11 with respect to isopropanol, ethanol and methanol. Here all three have similar dipole moments (in the range 1.6 – 1.7 D), so the one with highest latent heat of evaporation (isopropanol) caused the largest change in current. We would like to point out here that the effect of polarization is clearly observed only at high bias voltages. At low bias voltages, closer to

the V_{th} for a particular analyte, the response is primarily controlled by the temperature distribution of the tip (please refer to earlier discussions). Although polarization effect is also present for this bias range, it is insignificant compared to the other effects. However, at high bias voltages (i.e. over 8-9 V, which is much higher than the V_{th} of analytes considered here), effective surface area of the hot zone near the tip tends to saturate (temperature still keeps increasing though), allowing the surface polarization to play a dominant role in controlling the heat transfer to the analyte molecules, and consequently the device response.

At lower concentrations, results shown in Figure 4.11 is not suitable to pin-point an analyte as the slope of the fitted line becomes smaller; bringing all data points closer along the Y-axis. However, this can be used to estimate the concentration of the analyte as the curves are separated by a detectable margin for different concentrations.

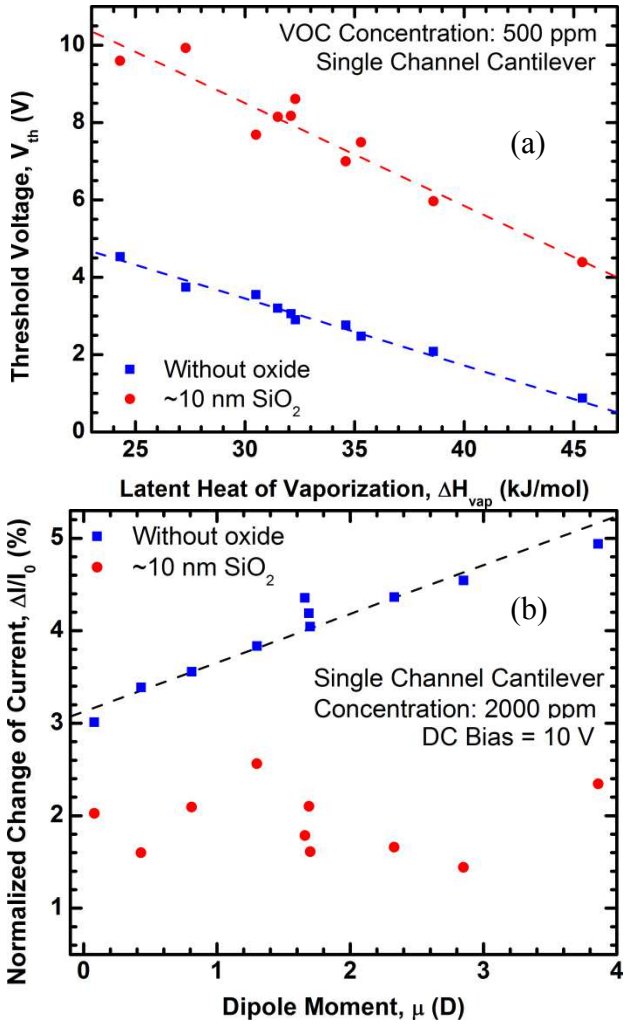

Figure 4.12 Effect of polarization on sensor response evident using a SC-TMH sensor covered with 10 nm thick PECVD SiO_2: (a) V_{th} vs ΔH_{vap} shows an upward shift in V_{th}; (b) No correlation with response magnitude with dipole moment.

Figure 4.12 shows the effect of polarization on sensor response even more clearly. We repeated our experiment using a SC-TMH sensor which was coated with about 10 nm thick PECVD SiO_2. As a result, we saw that threshold voltage increased by 3-6 V, the change was more severe for analytes with low latent heat of evaporation. In Figure 4.12(b), there is no correlation with normalized change of current and dipole moment of the analyte at a constant bias if the device is coated with SiO_2. Also the response is less in

magnitude than the one obtained from a regular SC-TMH device with no oxide coating. These two observations indicate that the polarized surface of AlGaN enhances the sensor response so that it can be observed at a lower V_{th} in a more predictable manner.

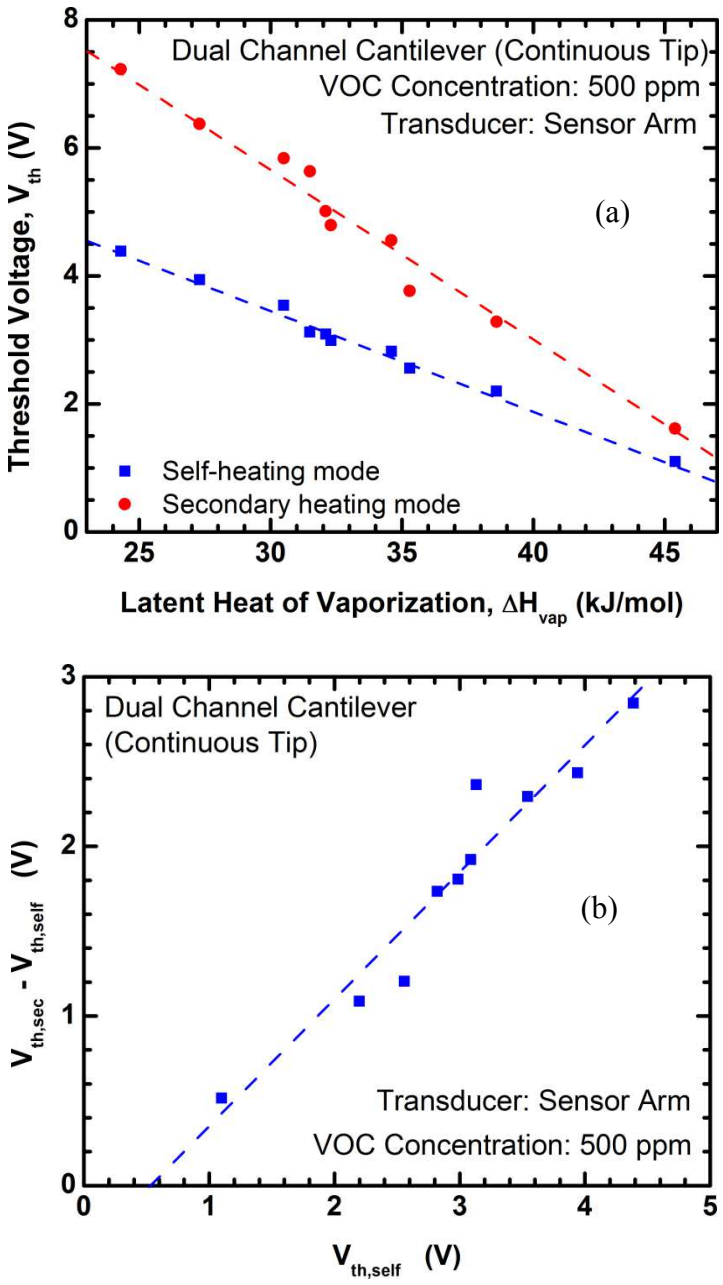

Figure 4.13 Response of continuous tip DC-TMH at (a) self-heating and secondary heating mode; (b) difference between the V_{th} values obtained in both modes as a function of self-heating V_{th}.

4.2.4 **Sensing Using DC-TMH**

For continuous tip DC-TMH sensor, there are two modes of operation as explained earlier (Section 3.1.3, page 46). For self-heating mode, the sensor arm had a variable dc bias and the heater arm had a 0.5 V fixed dc bias. But for secondary heating mode, the heater arm had a variable dc bias and the sensor arm had a 0.5 V fixed dc bias. For both modes response was recorded only from the sensor arm, but that response was correlated with the variable bias. Figure 4.13 shows the difference in these two modes in terms of V_{th} for the same set of analytes. Figure 4.13(a) shows that Vth for self-heating mode is very similar to a SC-TMH device, which is also a self-heating device with similar dimensions and conductivity. However, the slope of V_{th} is higher for secondary heating mode. Figure 4.13(b) shows the difference of V_{th} values obtained in self-heating and secondary heating mode as a function self-heating V_{th} ($V_{th,self}$). This shows that fitted line intersects X-axis at around 0.5 V. This signifies that if there existed a VOC which would register a $V_{th,self}$ of 0.5 V, for that VOC both self-heating and secondary heating modes would give the same V_{th}; as $V_{th,self}$ increases above 0.5 V, the deviation increases as well. It should be noted that in secondary heating mode, the sensor arm was biased at 0.5 V which matches with this X-axis intercept. While the exact explanation for this observation is still unclear, we believe it happens due to the difference in electric field at the tip of the sensor arm in these modes. For self-heating mode, this electric field keeps increasing as the bias is increased, and so does the temperature. But in secondary heating mode, while the temperature increases due to the secondary heating, sensor arm observes the same electric field due to the constant dc bias. If the sensitivity of the device is a function of electric field as well, then this difference should indeed affect the response. When both arms are biased at 0.5 V (in either mode), the electric field and temperature

become consistent with each other and the difference in response diminishes. That is why, the difference in V_{th} becomes zero at 0.5 V bias.

Unlike the continuous tip DC-TMH, split tip DC-TMH has an air gap between the tip regions of the two channels. Characterization in self-heating and secondary heating modes are possible; self-heating mode being analogous to the steady-state mode of SC-TMH. However, secondary heating mode is much more complicated, as heat conduction takes place through a gaseous medium involving analyte molecules. This results in a more complicated picture, where thermal conductivity of the analyte plays an important role in addition to all other existing factors such as latent heat of evaporation, dipole moment, local electric field variation, etc. Coating the device with SiO_2 can reduce or nullify the effect of one or more factor, making the contribution of thermal conductivity more dominant. The detailed study of this type of device is beyond the scope of the current work and will be addressed in a future account.

4.3 Simulation Results

The simulation model described in section 3.3 (page 50) provides us some insight into the thermal characteristics of the device that could not be measured experimentally. Using the model described above, calculated temperature profiles are obtained and shown in Figure 4.14, for 10 V dc bias, with and without 1% of isopropanol vapor flow. For simplicity, we assumed a Gaussian distribution of vapor concentration centering at the middle point of the tip with a magnitude matching the theoretical calculation laid out in (11). The full width half maxima (FWHM) of that Gaussian profile was matched with the FWHM of the line scan profile of temperature obtained in Figure 4.14, which is shown in Figure 4.15. Therefore, the solution is iterative, where analyte distribution (the Gaussian

plot), joule heating (i.e. temperature), non-linear heat transfer (conduction, convection and radiation) and temperature dependent resistivity – all where determined self-consistently through an iterative solver. Figure 4.15 also shows the lowering of tip temperature in presence of VOC, as well as broadening of the temperature profile.

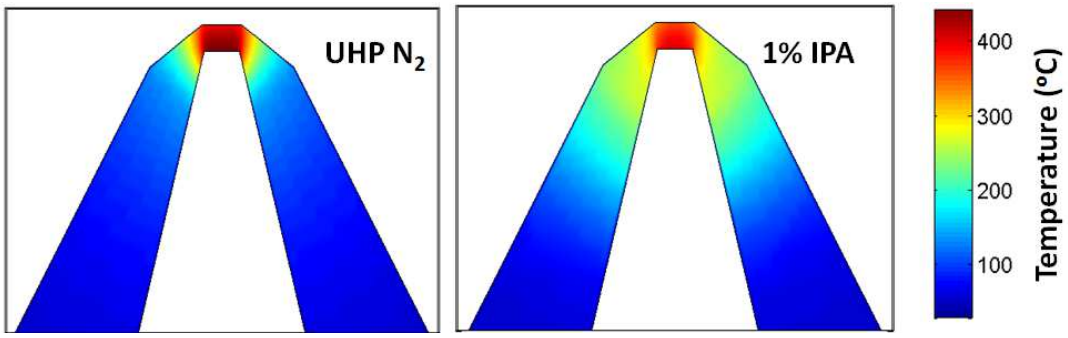

Figure 4.14 Simulated temperature profile for SC-TMH under 10 V dc bias, in UHP N_2 and 1% isopropanol.

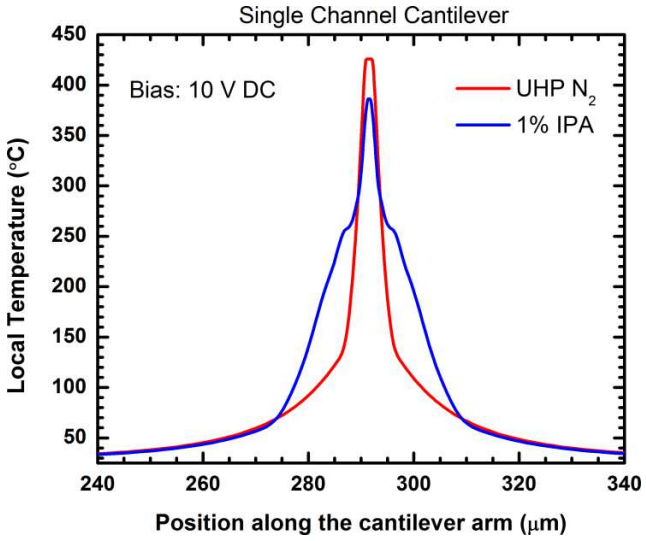

Figure 4.15 Temperature profile line scan along the length of the SC-TMH, extracted from Figure 4.14.

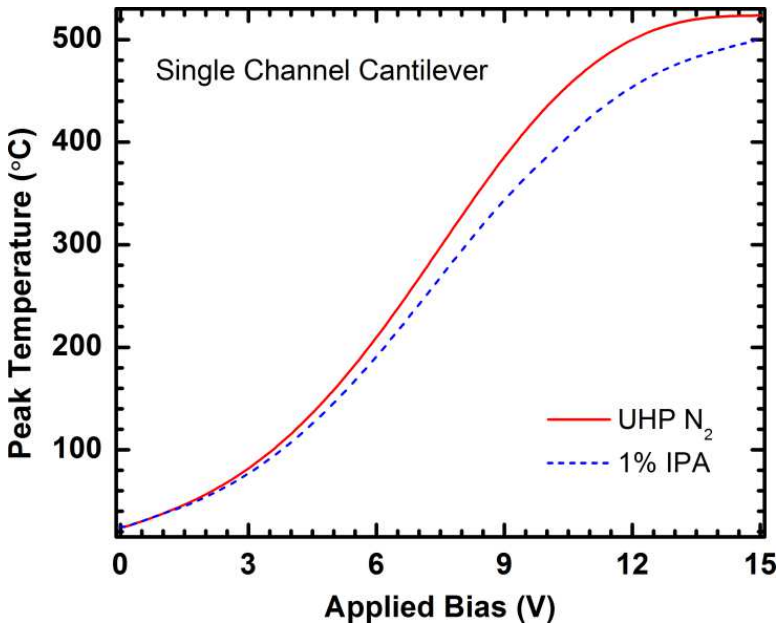

Figure 4.16 Simulated peak temperature of SC-TMH as a function of applied bias with or without analyte vapor flow (1% isopropanol).

Figure 4.16 shows the simulated peak temperature of a SC-TMH under different bias conditions. We can see that, in UHP N_2 environment, the peak temperature almost saturates after 13 V due to significant self-heating. However, the temperature profile in 1% isopropanol starts to vary from very low voltage (~1 V, close to the V_{th} of isopropanol) and starts to deviate more as bias voltage increases. However, at high bias (> 11 V) this curve starts to approach the reference curve (for UHP N_2) instead of saturating. This happens due to the lowering contribution of VOC-induced heat transfer (which is assumed not to be a strong function of temperature) at high bias, where other modes of heat transfer dominate more. Asymptotically these two curves would come very close to each other if a higher is applied. This is consistent with the observation in Figure 4.8, where we saw response of SC-TMH going down at high bias.

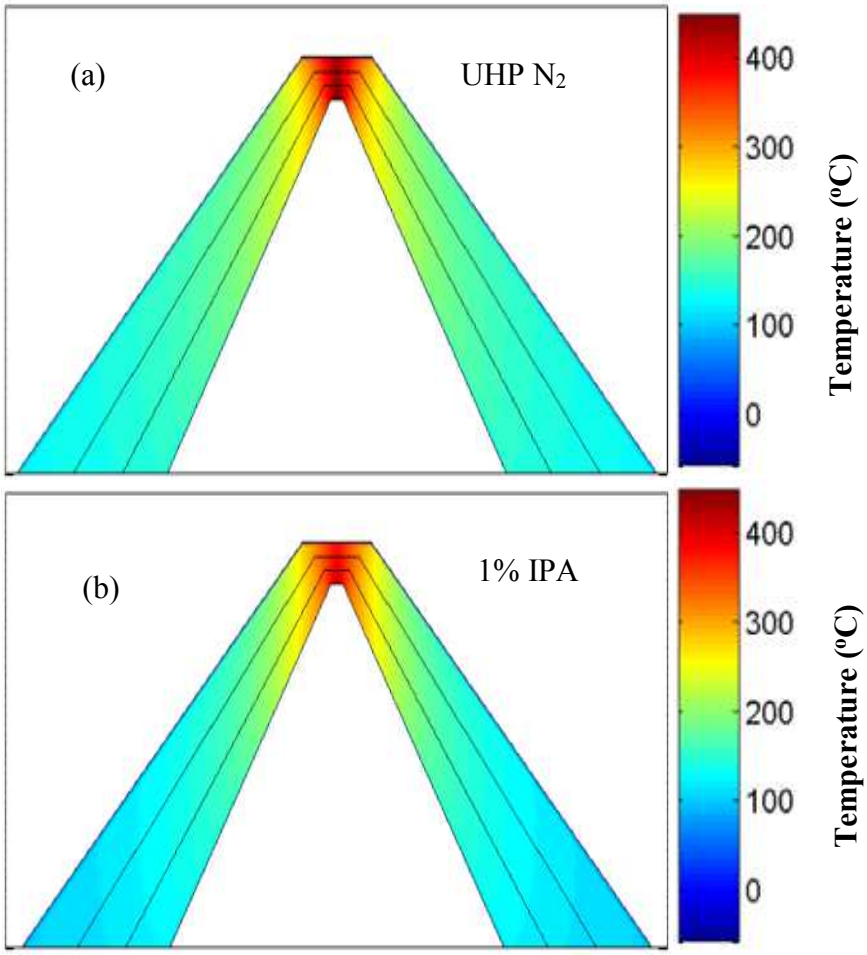

Figure 4.17 Simulated temperature profile for continuous tip DC-TMH under 10 V dc bias, in (a) UHP N_2 and (b) 1% isopropanol.

Figure 4.17 and Figure 4.18 show the simulated temperature profile for a continuous tip DC-TMH device in secondary heating mode. Here heating arm is biased at 12 V dc and sensing arm is biased at 0.5 dc bias. Figure 4.18 shows that the peak temperature for both channels are significantly close, which happens due to the high thermal conductivity of GaN. In presence of VOC (1% IPA), peak temperature goes down for both channels. Broadening of the profile is also visible here for both channels, but not as much as the SC-TMH due to the wider tip region of the DC-TMH cantilever that spreads out the heat distribution, making localized changes less pronounced.

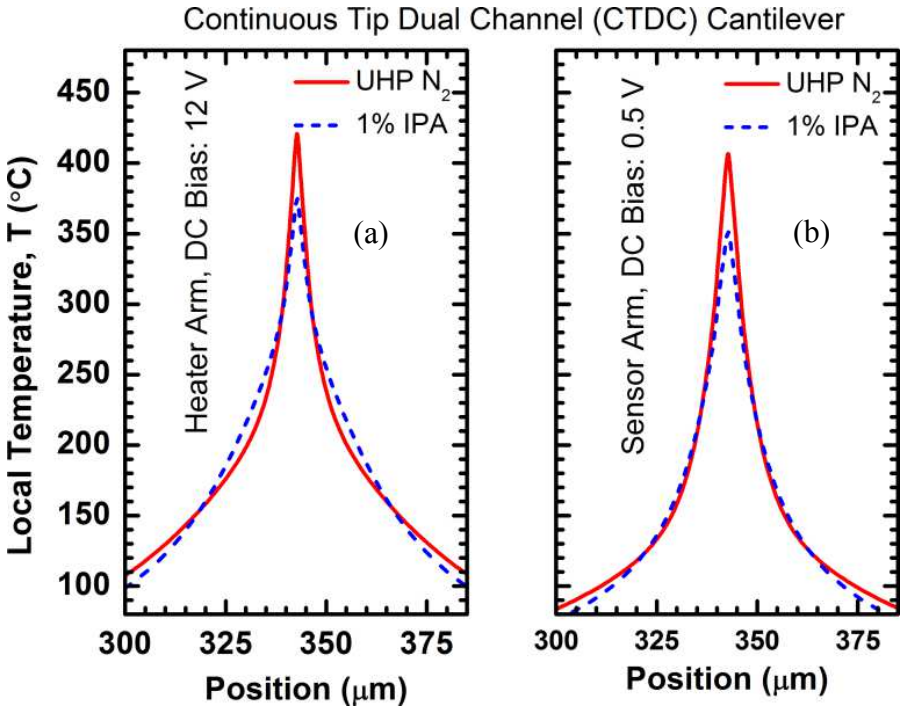

Figure 4.18 Simulated temperature profile (line scan along the length of the cantilever) for continuous tip DC-TMH under 10 V dc bias, in (a) UHP N_2 and (b) 1% isopropanol.

Figure 4.19 and Figure 4.20 show the simulated temperature profile for a split tip DC-TMH device in secondary heating mode. Here heating arm is biased at 12 V dc and sensing arm is biased at 0.5 dc bias. Figure 4.20 shows that the peak temperature for both channels are very different due to the air gap. In presence of VOC (1% IPA), peak temperature goes down for both channels. Broadening of the profile is more pronounced on the heater arm, since the air gap makes is almost thermally isolated from the sensor arm, making it analogous to SC-TMH. However conductivity of IPA vapor is lower than air, therefore in presence of 1% IPA, the sensor arm gets even lower heat from the heater arm due to the low conductivity as well as the other effects (e.g. latent heat, etc) all lowering the temperature even more. This makes the temperature change on the sensor arm in presence of IPA more significant.

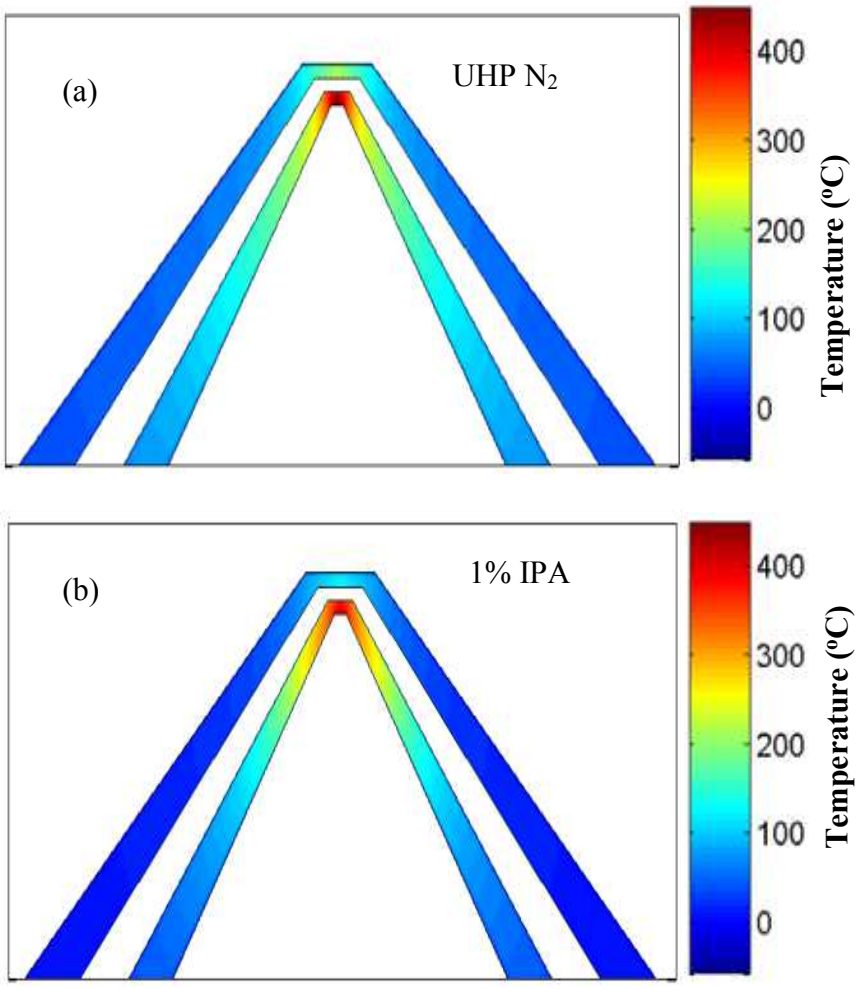

Figure 4.19 Simulated temperature profile for split tip DC-TMH under 10 V dc bias, in (a) UHP N_2 and (b) 1% isopropanol.

Finally, Figure 4.21 shows the timing diagram for all types of devices simulated in this work. It shows the transient response of the devices ignoring all electrical transient and sensing transients - both bias voltage and analyte concentration were assumed to follow an ideal step profile. This is only to show the thermal transient associated with the device, and should not be confused with the rise and fall times obtained experimentally. This also shows that rise and fall times are limited by the time required by the analyte

flow to establish an equilibrium concentration, as thermal response time is several order magnitude lower than actual device response time.

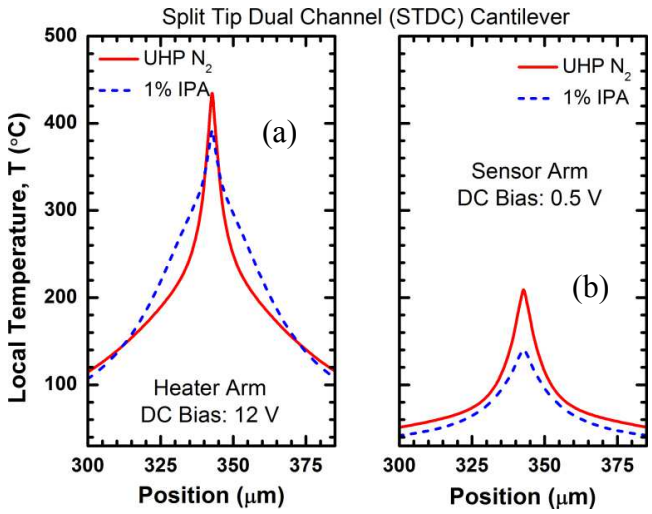

Figure 4.20 Simulated temperature profile (line scan along the length of the cantilever) for split tip DC-TMH under 10 V dc bias, in (a) UHP N_2 and (b) 1% isopropanol.

Table 4.4 Calculated peak temperature, FWHM of temperature profile and heating/sensing time constants.

Cantilever Type	Peak Temperature, ^oC (UHP N_2)	FWHM (μm) (UHP N_2)	Peak Temperature, ^oC (1% IPA)	FWHM (μm) (1% IPA)	Time constant, (μs) Heating in UHP N_2	Time constant, (μs) sensing in 1% IPA
SC-TMH	425.89	5.68	386.17	15.56	47	66
CTDC-TMH, heater arm	420.79	17.77	374.99	30.29	75	94
CTDC-TMH, sensor arm	406.53	14.39	351.60	19.59	112	143
STDC-TMH, heater arm	434.55	19.12	392.19	38.20	53	74
STDC-TMH, sensor arm	208.96	14.04	140.55	21.06	89	119

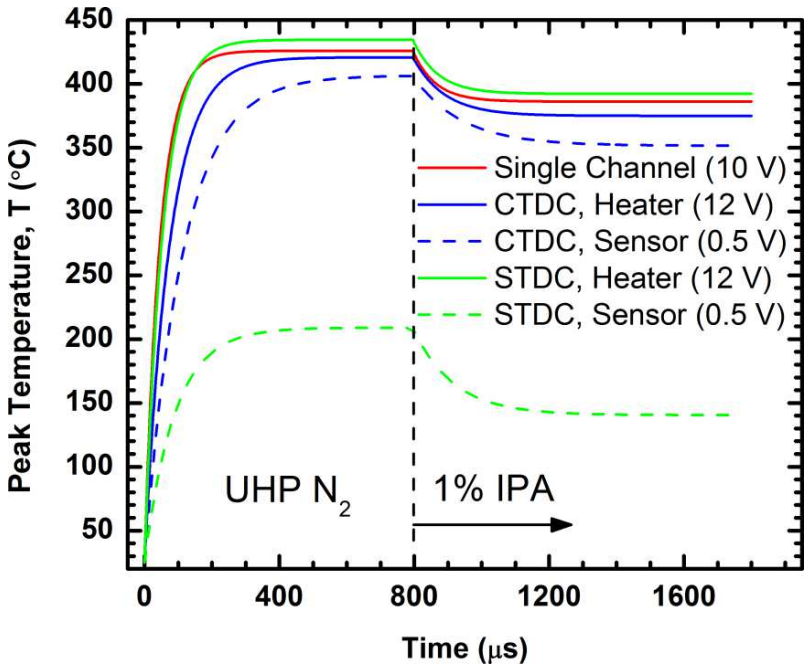

Figure 4.21 Simulated transient response of various TMH devices showing thermal rise and fall times. Electrical transient is neglected here, as well as the delay associated with analyte flow (abrupt change in analyte concentration is assumed).

Table 4.4 summarizes all the results shown in Figure 4.14 through Figure 4.21. Here we see the thermal response time during heating (in UHP N_2) and sensing (in 1% IPA) phases, peak temperature values for UHP N_2 and 1% IPA as well as their associated FWHM.

Chapter 5

Conclusion

In conclusion, we have demonstrated novel AlGaN/GaN heterostructure based triangular microcantilever heaters for environmental sensing. A robust fabrication process has been developed and a variety of simple and complex structures are fabricated. It has been shown that these devices can be used as multi-modal volatile organic compound (VOC) detectors with exceptional reliability and repeatability. Many of the devices used in this work were studied over a period of two years, both in open air and in a closed chamber; and were subjected to much higher applied biases (up to ~90 V). However, no noticeable change in device characteristics was observed in this time frame, which underscores high measurement reliability as well as thermal and chemical stability of these sensors.

These triangular microcantilever heaters are highly sensitive to VOCs without the need for any complicated functionalization technique, characterization techniques are also simpler (mostly dc characterization) and not at all bulky. The sensing makes use of simple physical phenomena such as evaporation of agglomerated analyte molecules off a heated surface. However, the novelty of the work lies in the use of AlGaN/GaN heterostructure as the building block, which not only has high temperature stability and chemical inertness, but also significant polarization charge on the surface, that is found out to be largely enhancing the sensing response.

These devices are predicted to have a noise limited resolution down to 1.5 ppm and proper system design can likely pull it down to high ppb values. Since sensing responses could be correlated with easily available physical parameters such as latent heat of evaporation, molecular dipole moment and thermal conductivity in vapour phase, calibration of this device is also easy and straight forward.

Finally an all-inclusive coupled heat transfer-Joule heating-molecular interaction simulation has been performed to explain many observations and also to predict the behaviour of the device is unknown conditions.

While there is still room for further investigation with the dual channel TMH devices with continuous and split tips, the current study provides sufficient evidence to establish the novelty and promising future of this technology.

References

[1] H. Guo, S. C. Lee, L. Y. Chan, and W. M. Li, Risk assessment of exposure to volatile organic compounds in different indoor environments, Environ. Res. 94 (1), 57-66 (2004)

[2] H. Singh, Y. Chen, A. Staudt, D. Jacob, D. Blake, B. Heikes, and J. Snow, Evidence from the Pacific troposphere for large global sources of oxygenated organic compounds, Nature 410 (6832), 1078-1081 (2001)

[3] M. Gall The Si-planar-pellistor array, a detection unit for combustible gases, Sens. Actuators B 16 (1), 260-264 (1993)

[4] M.-T. Ke, M.-T. Lee, C.-Y. Lee, and L.-M. Fu, A MEMS-based benzene gas sensor with a self-heating WO_3 sensing layer, Sensors 9, 2895-2906 (2009)

[5] C. J. Martinez, B. Hockey, C. B. Montgomery, and S. Semancik, Porous tin oxide nanostructured microspheres for sensor applications, Langmuir, 21 (17), 7937-7944 (2005)

[6] K. D. Benkstein, and S. Semancik, Mesoporous nanoparticle TiO_2 thin films for conductometric gas sensing on microhotplate platforms, Sens. Actuators B 113(1), 445-453 (2006)

[7] R. Artzi-Gerlitz, K. D. Benkstein, D. L. Lahr, J. L. Hertz, C. B. Montgomery, J. E. Bonevich, S. Semancik, and M. J. Tarlov, Fabrication and gas sensing performance of parallel assemblies of metal oxide nanotubes supported by porous aluminum oxide membranes, Sens. Actuators B 136 (1), 257-264 (2009).

[8] M. Qazi, G. Koley, S. Park, T. Vogt, NO_2 detection by adsorption induced work function changes in In_2O_3 thin films, Appl. Phys. Lett. 91 (4), 043113 (2007)

[9] M. Qazi and G. Koley, NO_2 detection using microcantilever based potentiometry, Sensors 8, 7144 (2008)

[10] G. Koley, M. G. Spencer, H. R. Bhangale, Cantilever effects on the measurement of electrostatic potentials by scanning Kelvin probe microscopy, Appl. Phys. Lett. 79 (4) , 545-547 (2001)

[11] M. Qazi, N. DeRoller, A. Talukdar, G. Koley, III-V Nitride based piezoresistive microcantilever for sensing applications, Appl. Phys. Lett. 99 (19), 193508 (2011)

[12] Y. J. Tang, J. Fang, X. H. Xu, H. F. Ji, G. M. Brown, and T. Thundat, Detection of femtomolar concentrations of HF using an SiO_2 microcantilever, Anal. Chem. 76, 2478 (2004)

[13] G. Koley, M. Qazi , L. Lakshmanan, and T. G. Thundat, Gas sensing using electrostatic force potentiometry, Appl. Phys. Lett. 90 (17), 173105 (2007)

[14] L.A Pinnaduwage, T Thundat, J.E Hawk, D.L Hedden, P.F Britt, E.J Houser, S Stepnowski, R.A McGill, D Bubb, Detection of 2,4-dinitrotoluene using microcantilever sensors, Sens. Actuators B 99 (2–3), 223-229 (2004)

[15] Z. Hu, T. Thundat, and R. J. Warmack, Investigation of adsorption and absorption-induced stresses using microcantilever sensors, J. Appl. Phys. 90 (1), 427-431 (2001)

[16] C. Canetta and A. Narayanaswamy, Sub-picowatt resolution calorimetry with a bi-material microcantilever sensor, Appl. Phys. Lett. 102 (10), 103112 (2013)

[17] J. O. Liu, S. Somnath, and W. P. King, Heated atomic force microscope cantilever with high resistivity for improved temperature sensitivity, Sens. Actuators A 201, 141-147 (2013)

[18] J. Lee, T. L. Wright, M. R. Abel, E. O. Sunden, A. Marchenkov, S. Graham, and W. P. King, Thermal conduction from microcantilever heaters in partial vacuum, J. Appl. Phys. 101(1), 014906 (2007)

[19] J. Lee and W. P. King, Microcantilever hotplates: Design, fabrication, and characterization, Sens. Actuators A 136, 291–298 (2007)

[20] J. Lee, T. Beechem, T. L. Wright, B. A. Nelson, S. Graham, and W. P. King, Electrical, thermal, and mechanical characterization of silicon microcantilever heaters, J. Microelectromech. Syst. 15(6), (2006)

[21] L. A. Pinnaduwage, V. Boiadjiev, J. E. Hawk, and T. Thundat, Sensitive detection of plastic explosives with self-assembled monolayer-coated microcantilevers,

Appl. Phys. Lett. 83 (7), 1471-1473 (2003)

[22] A. Loui, D. J. Sirbuly, S. Elhadj, S. K. McCall, B. R. Hart, and T. V. Ratto, Detection and discrimination of pure gases and binary mixtures using a dual-modality microcantilever sensor, Sens. Actuators A 159(1), 58-63 (2010)

[23] S. Tétin, B. Caillard, F. Ménil, H. Debéda, C. Lucat, C. Pellet, and I. Dufour, Modeling and performance of uncoated microcantilever-based chemical sensors, Sens. Actuators B 143(2), 555-560 (2010)

[24] G. Koley, M. G. Spencer, Surface potential measurements on GaN and AlGaN/GaN heterostructures by scanning Kelvin probe microscopy, J. Appl. Phys. 90 (1), 337-344 (2001)

[25] A. Talukdar, M. Qazi, and G. Koley, High frequency dynamic bending response of piezoresistive GaN microcantilevers, Appl. Phys. Lett. 101 (25), 252102 (2012)

[26] Talukdar, and G. Koley, Impact of biasing conditions on displacement transduction by III-Nitride microcantilevers, IEEE Elec. Dev. Lett. 35 (12), 1299-1301 (2014)

[27] F. P. Incropera and D. P. DeWitt, Fundamentals of Heat and Mass Transfer, 4th ed, John Wiley & Sons, New York, 1996.

[28] S. K. Brown, M. R. Sim, M. J. Abramson, and C. N. Gray, Concentrations of volatile organic compounds in indoor air–a review, Indoor Air 4(2), 123-134 (1994)

[29] R. Neuberger, G. Müller, O. Ambacher, and M. Stutzmann, High-electron-mobility AlGaN/GaN transistors (HEMTs) for fluid monitoring applications, Phys. Status Solidi A 185(1), 85-89 (2001)

[30] R. J. Wilfinge, P. H. Bardell, and D. S. Chhabra, "The Resonistor: A Frequency Selective Device Utilizing the Mechanical Resonance of a Silicon Substrate," *IBM J. Res. Dev.* **12**, 113 (1968).

[31] T. M. S. Heng, "Trimming of Microstrip Circuits Utilizing Microcantilever Air Gaps " *IEEE Trans. Microw. Theory Tech.* **MT19**, 652 (1971).

[32] K. E. Petersen, "Micromechanical Membrane Switches on Silicon," *IBM J. Res. Dev.* **23**, 376 (1979).

[33] G. Binnig, C. F. Quate, and C. Gerber, "Atomic Force Microscope," *Phys. Rev. Lett.* **56**, 930 (1986).

[34] T. Itoh, and T. Suga, "Force sensing microcantilever using sputtered zinc oxide thin film," *Appl. Phys. Lett.* **64**, 37 (1994).

[35] J. P. Cleveland, S. Manne, D. Bocek, and P. K. Hansma, "A nondestructive method for determining the spring constant of cantilevers for scanning force microscopy," *Rev. Sci. Instrum.* **64**, 403 (1993).

[36] J. K. Gimzewski, C. Gerber, E. Meyer, and R. R. Schlittler, "Observation of a chemical reaction using a micromechanical sensor," *Chem. Phys. Lett.* **217**, 589 (1994).

[37] H. P. Lang, and C. Gerber, "Microcantilever sensors", In *Stm and Afm Studies On*, pp 1, Springer-Verlag Berlin, Berlin (2008).

[38] T. Thundat, R. J. Warmack, G. Y. Chen, and D. P. Allison, "Thermal and ambient-induced deflections of scanning force microscope cantilevers," *Appl. Phys. Lett.* **64**, 2894 (1994).

[39] T. Thundat, G. Y. Chen, R. J. Warmack, D. P. Allison, and E. A. Wachter, "Vapor Detection Using Resonating Microcantilevers," *Analytical Chemistry* **67**, 519 (1995).

[40] T. Thundat, E. A. Wachter, S. L. Sharp, and R. J. Warmack, "Detection of mercury vapor using resonating microcantilevers," *Appl. Phys. Lett.* **66**, 1695 (1995).

[41] G. Y. Chen, T. Thundat, E. A. Wachter, and R. J. Warmack, "Adsorption-induced surface stress and its effects on resonance frequency of microcantilevers," *Journal of Applied Physics* **77**, 3618 (1995).

[42] P. I. Oden, P. G. Datskos, T. Thundat, and R. J. Warmack, "Uncooled thermal imaging using a piezoresistive microcantilever," *Appl. Phys. Lett.* **69**, 3277 (1996).

[43] P. G. Datskos, P. I. Oden, T. Thundat, E. A. Wachter, R. J. Warmack, and S. R. Hunter, "Remote infrared radiation detection using piezoresistive microcantilevers," *Appl. Phys. Lett.* **69**, 2986 (1996).

[44] E. A. Wachter, T. Thundat, P. I. Oden, R. J. Warmack, P. G. Datskos, and S. L. Sharp, "Remote optical detection using microcantilevers," *Rev. Sci. Instrum.* **67**, 3434 (1996).

[45] L. A. Pinnaduwage, V. Boiadjiev, J. E. Hawk, and T. Thundat, "Sensitive detection of plastic explosives with self-assembled monolayer-coated microcantilevers," *Appl. Phys. Lett.* **83**, 1471 (2003).

[46] L. A. Pinnaduwage, A. Gehl, D. L. Hedden, G. Muralidharan, T. Thundat, R. T. Lareau, T. Sulchek, L. Manning, B. Rogers, M. Jones, and J. D. Adams, "A microsensor for trinitrotoluene vapour," *Nature* **425**, 474 (2003).

[47] L. A. Pinnaduwage, T. Thundat, J. E. Hawk, D. L. Hedden, R. Britt, E. J. Houser, S. Stepnowski, R. A. McGill, and D. Bubb, "Detection of 2,4-dinitrotoluene using microcantilever sensors," *Sensors and Actuators B-Chemical* **99**, 223 (2004).

[48] K. M. Hansen, H. F. Ji, G. H. Wu, R. Datar, R. Cote, A. Majumdar, and T. Thundat, "Cantilever-based optical deflection assay for discrimination of DNA

single-nucleotide mismatches," *Analytical Chemistry* **73**, 1567 (2001).

[49] G. H. Wu, R. H. Datar, K. M. Hansen, T. Thundat, R. J. Cote, and A. Majumdar, "Bioassay of prostate-specific antigen (PSA) using microcantilevers," *Nature Biotechnology* **19**, 856 (2001).

[50] G. H. Wu, H. F. Ji, K. Hansen, T. Thundat, R. Datar, R. Cote, M. F. Hagan, A. K. Chakraborty, and A. Majumdar, "Origin of nanomechanical cantilever motion generated from biomolecular interactions," *Proceedings of the National Academy of Sciences of the United States of America* **98**, 1560 (2001).

[51] J. Mertens, E. Finot, M. H. Nadal, V. Eyraud, O. Heintz, and E. Bourillot, "Detection of gas trace of hydrofluoric acid using microcantilever," *Sensors and Actuators B-Chemical* **99**, 58 (2004).

[52] Y. J. Tang, J. Fang, X. H. Xu, H. F. Ji, G. M. Brown, and T. Thundat, "Detection of femtomolar concentrations of HF using an SiO2 microcantilever," *Analytical Chemistry* **76**, 2478 (2004).

[53] D. R. Baselt, B. Fruhberger, E. Klaassen, S. Cemalovic, C. L. Britton, S. V. Patel, T. E. Mlsna, D. McCorkle, and B. Warmack, "Design and performance of a microcantilever-based hydrogen sensor," *Sensors and Actuators B-Chemical* **88**, 120 (2003).

[54] F. M. Battiston, J. P. Ramseyer, H. P. Lang, M. K. Baller, C. Gerber, J. K. Gimzewski, E. Meyer, and H. J. Guntherodt, "A chemical sensor based on a microfabricated cantilever array with simultaneous resonance-frequency and bending readout," *Sensors and Actuators B-Chemical* **77**, 122 (2001).

[55] D. Lange, C. Hagleitner, A. Hierlemann, O. Brand, and H. Baltes,

"Complementary metal oxide semiconductor cantilever arrays on a single chip: Mass-sensitive detection of volatile organic compounds," *Analytical Chemistry* **74**, 3084 (2002).

[56] H. Jensenius, J. Thaysen, A. A. Rasmussen, L. H. Veje, O. Hansen, and A. Boisen, "A microcantilever-based alcohol vapor sensor-application and response model," *Appl. Phys. Lett.* **76**, 2615 (2000).

[57] J. Thaysen, A. Boisen, O. Hansen, and S. Bouwstra, "Atomic force microscopy probe with piezoresistive read-out and a highly symmetrical Wheatstone bridge arrangement," *Sens. Actuator A-Phys.* **83**, 47 (2000).

[58] Y. M. Yang, H. F. Ji, and T. Thundat, "Nerve agents detection using a Cu2+/L-cysteine bilayer-coated microcantilever," *J. Am. Chem. Soc.* **125**, 1124 (2003).

[59] R. L. Gunter, W. G. Delinger, K. Manygoats, A. Kooser, and T. L. Porter, "Viral detection using an embedded piezoresistive microcantilever sensor," *Sens. Actuator A-Phys.* **107**, 219 (2003).

[60] K. Y. Gfeller, N. Nugaeva, and M. Hegner, "Micromechanical oscillators as rapid biosensor for the detection of active growth of Escherichia coli," *Biosens. Bioelectron.* **21**, 528 (2005).

[61] S. Cherian, R. K. Gupta, B. C. Mullin, and T. Thundat, "Detection of heavy metal ions using protein-functionalized microcantilever sensors," *Biosens. Bioelectron.* **19**, 411 (2003).

[62] W. Y. Shih, X. P. Li, H. M. Gu, W. H. Shih, and I. A. Aksay, "Simultaneous liquid viscosity and density determination with piezoelectric unimorph cantilevers," *Journal of Applied Physics* **89**, 1497 (2001).

[63] R. Bashir, J. Z. Hilt, O. Elibol, A. Gupta, and N. A. Peppas, "Micromechanical cantilever as an ultrasensitive pH microsensor," *Appl. Phys. Lett.* **81**, 3091 (2002).

[64] J. H. Lee, T. S. Kim, and K. H. Yoon, "Effect of mass and stress on resonant frequency shift of functionalized Pb(Zr0.52Ti0.48)O3 thin film microcantilever for the detection of C-reactive protein," *Appl. Phys. Lett.* **84**, 3187 (2004).

[65] I. Voiculescu, M. E. Zaghloul, R. A. McGill, E. J. Houser, and G. K. Fedder, "Electrostatically actuated resonant microcantilever beam in CMOS technology for the detection of chemical weapons," *IEEE Sens. J.* **5**, 641 (2005).

[66] S. Q. Li, L. Orona, Z. M. Li, and Z. Y. Cheng, "Biosensor based on magnetostrictive microcantilever," *Appl. Phys. Lett.* **88**, 073507 (2006).

[67] J. D. Adams, G. Parrott, C. Bauer, T. Sant, L. Manning, M. Jones, B. Rogers, D. McCorkle, and T. L. Ferrell, "Nanowatt chemical vapor detection with a self-sensing, piezoelectric microcantilever array," *Appl. Phys. Lett.* **83**, 3428 (2003).

[68] N. V. Lavrik, and P. G. Datskos, "Femtogram mass detection using photothermally actuated nanomechanical resonators," *Appl. Phys. Lett.* **82**, 2697 (2003).

[69] B. Ilic, H. G. Craighead, S. Krylov, W. Senaratne, C. Ober, and P. Neuzil, "Attogram detection using nanoelectromechanical oscillators," *Journal of Applied Physics* **95**, 3694 (2004).

[70] T. P. Burg, M. Godin, S. M. Knudsen, W. Shen, G. Carlson, J. S. Foster, K. Babcock, and S. R. Manalis, "Weighing of biomolecules, single cells and single nanoparticles in fluid," *Nature* **446**, 1066 (2007).

[71] S. M. Han, H. Benaroya, and T. Wei, "Dynamics of transversely vibrating beams

using four engineering theories," *J. Sound Vibr.* **225**, 935 (1999).

[72] S. P. Timoshenko, "On the correction factor for shear of the differential equation for transverse vibrations of bars of uniform cross-section," *Philosophical Magazine* **41** (1921).

[73] S. P. Timoshenko, "On the transverse vibrations of bars of uniform cross-section," *Philosophical Magazine* **43** (1922).

[74] R. W. Traillnash, and A. R. Collar, "The effects of shear flexibility and rotatory inertia on the bending vibrations of beams," *Quarterly Journal of Mechanics and Applied Mathematics* **6**, 186 (1953).

[75] C. L. Dolph, "On the Timoshenko theory of transverse beam vibrations," *Q. Appl. Math.* **12**, 175 (1954).

[76] N. A. Burnham, X. Chen, C. S. Hodges, G. A. Matei, E. J. Thoreson, C. J. Roberts, M. C. Davies, and S. J. B. Tendler, "Comparison of calibration methods for atomic-force microscopy cantilevers," *Nanotechnology* **14**, 1 (2003).

[77] A. W. McFarland, "PhD Thesis," In *Mechanical Engineering*, Georgia Institute of Technology, Atlanta (2005).

[78] S. D. Senturia, *Microsystem Design*, Kluwer Academic Publishers (2001).

[79] R. R. Archer, N. H. Cook, S. H. Crandall, N. C. Dahl, T. J. Lardner, F. A. McClintock, E. Rabinowicz, and G. S. Reichenback, *An Introduction to the Mechanics of Solids*, 2nd ed., McGraw-Hill, New York (1972).

[80] Z. Y. Hu, T. Thundat, and R. J. Warmack, "Investigation of adsorption and absorption-induced stresses using microcantilever sensors," *Journal of Applied Physics* **90**, 427 (2001).

[81] M. Godin, V. Tabard-Cossa, Y. Miyahara, T. Monga, P. J. Williams, L. Y. Beaulieu, R. B. Lennox, and P. Grutter, "Cantilever-based sensing: the origin of surface stress and optimization strategies," *Nanotechnology* **21**, 075501 (2010).

[82] M. Godin, V. Tabard-Cossa, P. Grutter, and P. Williams, "Quantitative surface stress measurements using a microcantilever," *Appl. Phys. Lett.* **79**, 551 (2001).

[83] G. G. Stoney, "The tension of metallic films deposited by electrolysis," *Proceedings of the Royal Society of London Series a-Containing Papers of a Mathematical and Physical Character* **82**, 172 (1909).

[84] C. W. Baek, Y. K. Kim, Y. Ahn, and Y. H. Kim, "Measurement of the mechanical properties of electroplated gold thin films using micromachined beam structures," *Sens. Actuator A-Phys.* **117**, 17 (2005).

[85] D. R. Evans, and V. S. J. Craig, "Sensing cantilever beam bending by the optical lever technique and its application to surface stress," *J. Phys. Chem. B* **110**, 5450 (2006).

[86] Y. Zhang, Q. Ren, and Y. P. Zhao, "Modelling analysis of surface stress on a rectangular cantilever beam," *J. Phys. D-Appl. Phys.* **37**, 2140 (2004).

[87] E. Finot, A. Passian, and T. Thundat, "Measurement of mechanical properties of cantilever shaped materials," *Sensors* **8**, 3497 (2008).

[88] J. E. Sader, "Surface stress induced deflections of cantilever plates with applications to the atomic force microscope: Rectangular plates," *Journal of Applied Physics* **89**, 2911 (2001).

[89] D. W. Dareing, and T. Thundat, "Simulation of adsorption-induced stress of a microcantilever sensor," *Journal of Applied Physics* **97**, 043526 (2005).

[90] R. Shuttleworth, "The Surface Tension of Solids," *Proceedings of the Physical Society of London Section A* **63**, 444 (1950).

[91] M. F. Hagan, A. Majumdar, and A. K. Chakraborty, "Nanomechanical forces generated by surface grafted DNA," *J. Phys. Chem. B* **106**, 10163 (2002).

[92] F. Liu, Y. Zhang, and Z. C. Ou-Yang, "Flexoelectric origin of nanomechanic deflection in DNA-microcantilever system," *Biosens. Bioelectron.* **18**, 655 (2003).

[93] J. Q. Zhang, S. W. Yu, X. Q. Feng, and G. F. Wang, "Theoretical analysis of adsorption-induced microcantilever bending," *Journal of Applied Physics* **103** (2008).

[94] R. Berger, E. Delamarche, H. P. Lang, C. Gerber, J. K. Gimzewski, E. Meyer, and H. J. Guntherodt, "Surface stress in the self-assembly of alkanethiols on gold," *Science* **276**, 2021 (1997).

[95] J. Fritz, M. K. Baller, H. P. Lang, H. Rothuizen, P. Vettiger, E. Meyer, H. J. Guntherodt, C. Gerber, and J. K. Gimzewski, "Translating biomolecular recognition into nanomechanics," *Science* **288**, 316 (2000).

[96] H. Ibach, "The role of surface stress in reconstruction, epitaxial growth and stabilization of mesoscopic structures," *Surf. Sci. Rep.* **29**, 195 (1997).

[97] D. Sander, and H. Ibach, "Experimental determination of adsorbate-induced surface stress: Oxygen on Si(111) and Si(100)," *Phys. Rev. B* **43**, 4263 (1991).

[98] G. Y. Huang, W. Gao, and S. W. Yu, "Model for the adsorption-induced change in resonance frequency of a cantilever," *Appl. Phys. Lett.* **89**, 043506 (2006).

[99] B. Ilic, D. Czaplewski, M. Zalalutdinov, H. G. Craighead, P. Neuzil, C. Campagnolo, and C. Batt, "Single cell detection with micromechanical

oscillators," *J. Vac. Sci. Technol. B* **19**, 2825 (2001).

[100] N. V. Lavrik, M. J. Sepaniak, and P. G. Datskos, "Cantilever transducers as a platform for chemical and biological sensors," *Rev. Sci. Instrum.* **75**, 2229 (2004).

[101] A. W. McFarland, M. A. Poggi, M. J. Doyle, L. A. Bottomley, and J. S. Colton, "Influence of surface stress on the resonance behavior of microcantilevers," *Appl. Phys. Lett.* **87** (2005).

[102] N. Sasaki, and M. Tsukada, "The relation between resonance curves and tip-surface interaction potential in noncontact atomic-force microscopy," *Jpn. J. Appl. Phys. Part 2 - Lett.* **37**, L533 (1998).

[103] K. M. Goeders, J. S. Colton, and L. A. Bottomley, "Microcantilevers: Sensing chemical interactions via mechanical motion," *Chem. Rev.* **108**, 522 (2008).

[104] G. Meyer, and N. M. Amer, "Novel optical approach to atomic force microscopy," *Appl. Phys. Lett.* **53**, 1045 (1988).

[105] N. Blanc, J. Brugger, N. F. deRooij, and U. Durig, "Scanning force microscopy in the dynamic mode using microfabricated capacitive sensors," *J. Vac. Sci. Technol. B* **14**, 901 (1996).

[106] J. Amirola, A. Rodriguez, L. Castaner, J. P. Santos, J. Gutierrez, and M. C. Horrillo, "Micromachined silicon microcantilevers for gas sensing applications with capacitive read-out," *Sensors and Actuators B-Chemical* **111**, 247 (2005).

[107] G. Shekhawat, S. H. Tark, and V. P. Dravid, "MOSFET-embedded microcantilevers for measuring deflection in biomolecular sensors," *Science* **311**, 1592 (2006).

[108] Y. Kanda, "Piezoresistance effect of silicon," *Sens. Actuator A-Phys.* **28**, 83

(1991). 246

[109] A. Dehe, K. Fricke, K. Mutamba, and H. L. Hartnagel, "A piezoresistive GaAs pressure sensor with GaAs/AlGaAs membrane technology," *J. Micromech. Microeng.* **5**, 139 (1995).

[110] G. Tosolini, G. Villanueva, F. Perez-Murano, and J. Bausells, "Silicon microcantilevers with MOSFET detection," *Microelectronic Engineering* **87**, 1245 (2010).

[111] S. Mostafa, I. Lee, S. K. Islam, S. A. Eliza, G. Shekhawat, V. P. Dravid, and F. S. Tulip, "Integrated MOSFET-Embedded-Cantilever-Based Biosensor Characteristic for Detection of Anthrax Simulant," *Ieee Electron Device Letters* **32**, 408 (2011).

[112] C. G. Hill, Jr., *An Introduction to Chemical Engineering Kinetics & Reaction Design*, John Wiley and Sons. Inc., New York City (1977).

[113] I. Langmuir, "The constitution and fundamental properties of solids and liquids Part I Solids," *J. Am. Chem. Soc.* **38**, 2221 (1916).

[114] T. Sahm, A. Gurlo, N. Barsan, and U. Weimar, "Basics of oxygen and SnO2 interaction; work function change and conductivity measurements," *Sensors and Actuators B-Chemical* **118**, 78 (2006).

[115] S. Cesaro-Tadic, G. Dernick, D. Juncker, G. Buurman, H. Kropshofer, B. Michel, C. Fattinger, and E. Delamarche, "High-sensitivity miniaturized immunoassays for tumor necrosis factor a using microfluidic systems," *Lab on a Chip* **4**, 563 (2004).

[116] A. Bietsch, J. Y. Zhang, M. Hegner, H. P. Lang, and C. Gerber, "Rapid

functionalization of cantilever array sensors by inkjet printing," *Nanotechnology* **15**, 873 (2004).

[117] L. Kelvin, *Philosophical Magazine* **46**, 82 (1898).

[118] W. A. Zisman, "A new method of measuring contact potential differences in metals," *Rev. Sci. Instrum.* **3**, 367 (1932).

[119] J. M. R. Weaver, and D. W. Abraham, "High resolution atomic force microscopy potentiometry," *J. Vac. Sci. Technol. B* **9**, 1559 (1991).

[120] M. Nonnenmacher, M. P. Oboyle, and H. K. Wickramasinghe, "Kelvin probe force microscopy," *Appl. Phys. Lett.* **58**, 2921 (1991).

[121] G. Koley, and M. G. Spencer, "Kelvin Probe Technique for Nanotechnology," In *Encyclopedia of Nanoscience and Nanotechnology*, 327 (2004).

[122] G. Koley, and M. G. Spencer, "Surface potential measurements on GaN and AlGaN/GaN heterostructures by scanning Kelvin probe microscopy," *Journal of Applied Physics* **90**, 337 (2001). 248

[123] P. M. Bridger, Z. Z. Bandic, E. C. Piquette, and T. C. McGill, "Measurement of induced surface charges, contact potentials, and surface states in GaN by electric force microscopy," *Appl. Phys. Lett.* **74**, 3522 (1999).

[124] J. R. Macdonald, and C. A. Barlow, "Work function change on monolayer adsorption," *Journal of Chemical Physics* **39**, 412 (1963).

[125] H. Geistlinger, I. Eisele, B. Flietner, and R. Winter, "Dipole- and charge transfer contributions to the work function change of semiconducting thin films: Experiment and theory," *Sensors and Actuators B-Chemical* **34**, 499 (1996).

[126] G. Koley, M. Qazi, L. Lakshmanan, and T. Thundat, "Gas sensing using

electrostatic force potentiometry," *Appl. Phys. Lett.* **90** (2007).

[127] M. Napoli, R. Baskaran, K. Turner, and B. Bamieh, "Understanding Mechanical Domain Parametric Resonance in Microcantilevers," In *16th IEEE Annual Int, Conf. On Micro Electro Mechanical Systems*, Kyoto, Japan (2003).

[128] M. Qazi, T. Vogt, and G. Koley, "Two-dimensional signatures for molecular identification," *Appl. Phys. Lett.* **92**, 103120 (2008).

[129] M. Qazi, T. Vogt, and G. Koley, "Trace gas detection using nanostructured graphite layers," *Appl. Phys. Lett.* **91**, 233101 (2007).

[130] H. M. Cheng, Q. H. Yang, and C. Liu, "Hydrogen storage in carbon nanotubes," *Carbon* **39**, 1447 (2001).

[131] F. Dimeo, I. S. Chen, P. Chen, J. Neuner, A. Roerhl, and J. Welch, "MEMS-based hydrogen gas sensors," *Sensors and Actuators B-Chemical* **117**, 10 (2006).

[132] T. N. Veziroglu, and F. Barbir, "Hydrogen: the Wonder Fuel," *International Journal of Hydrogen Energy* **17**, 391 (1992).

[133] Langmuir, "The adsorption of gases on plane surfaces of glass, mica and platinum," *J. Am. Chem. Soc.* **40**, 1361 (1918).

[134] K. Kim, J. H. Lee, S. M. Choi, I. H. Noh, H. R. Kim, N. I. Cho, C. Hong, and G. E. Jang, "Pd- and Pt-SiC Schottky diodes for detection of H2 and CH4 at high temperature," *Sensors and Actuators B-Chemical* **77**, 455 (2001).

[135] C. Cheng, Y. Y. Tsai, K. W. Lin, H. I. Chen, C. T. Lu, and W. C. Liu, "Hydrogen sensing characteristics of a Pt-oxide-Al0.3Ga0.7As MOS Schottky diode," *Sensors and Actuators B-Chemical* **99**, 425 (2004).

[136] Kim, F. Ren, B. P. Gila, C. R. Abernathy, and S. J. Pearton, "Reversible barrier

height changes in hydrogen-sensitive Pd/GaN and Pt/GaN diodes," *Appl. Phys. Lett.* **82**, 739 (2003).

[137] Lipkowski, and P. N. Ross, *Electrocatalysis*, Wiley-VCH, New York (1998).

[138] Souteyrand, D. Nicolas, and J. R. Martin, "Semiconductor/metal/gas behaviour through surface-potential change," *Sensors and Actuators B-Chemical* **25**, 871 (1995).

[139] Lundstrom, M. S. Shivaraman, and C. Svensson, "Chemical reactions on palladium surfaces studied with Pd-MOS structures," *Surf. Sci.* **64**, 497 (1977).

[140] N. Yamamoto, S. Tonomura, T. Matsuoka, and H. Tsubomura, "Effect of various substrates on the hydrogen sensitivity of palladium-semiconductor diodes," *Journal of Applied Physics* **52**, 6227 (1981).

[141] Z. Y. Fan, and J. G. Lu, "Gate-refreshable nanowire chemical sensors," *Appl. Phys. Lett.* **86**, 123510 (2005).

[142] A. Gurlo, N. Barsan, M. Ivanovskaya, U. Weimar, and W. Gopel, "In2O3 and MoO3-In2O3 thin film semiconductor sensors: interaction with NO2 and O3," *Sensors and Actuators B-Chemical* **47**, 92 (1998).

[143] G. Eranna, B. C. Joshi, D. P. Runthala, and R. P. Gupta, "Oxide materials for development of integrated gas sensors - A comprehensive review," *Crit. Rev. Solid State Mat. Sci.* **29**, 111 (2004).

[144] H. Zhang, Z. Q. Liu, C. Li, T. Tang, X. L. Liu, S. Han, B. Lei, and C. W. Zhou, "Detection of NO2 down to ppb levels using individual and multiple In2O3 nanowire devices," *Nano Lett.* **4**, 1919 (2004).

[145] O. Leenaerts, B. Partoens, and F. M. Peeters, "Adsorption of H2O, NH3, CO,

NO2, and NO on graphene: A first-principles study," *Phys. Rev. B* **77** (2008).

[146] N. Barsan, and U. Weimar, "Conduction model of metal oxide gas sensors," *Journal of Electroceramics* **7**, 143 (2001).

[147] S. Park, E. DiMasi, Y. I. Kim, W. Q. Han, P. M. Woodward, and T. Vogt, "The preparation and characterization of photocatalytically active TiO2 thin films and nanoparticles using Successive-Ionic-Layer-Adsorption-and-Reaction," *Thin Solid Films* **515**, 1250 (2006).

[148] R. J. Chen, N. R. Franklin, J. Kong, J. Cao, T. W. Tombler, Y. G. Zhang, and H. J. Dai, "Molecular photodesorption from single-walled carbon nanotubes," *Appl. Phys. Lett.* **79**, 2258 (2001).

[149] Koley, H. Y. Cha, C. I. Thomas, and M. G. Spencer, "Laser-induced surface potential transients observed in III-nitride heterostructures," *Appl. Phys. Lett.* **81**, 2282 (2002).

[150] Qazi, and G. Koley, "NO2 Detection Using Microcantilever Based Potentiometry," *Sensors* **8**, 7144 (2008).

[151] S. M. Sze, *Physics of Semiconductor Devices*, 2nd ed., Wiley, New York (1981).

[152] Kronik, and Y. Shapira, "Surface photovoltage phenomena: theory, experiment, and applications," *Surf. Sci. Rep.* **37**, 1 (1999). 250 L. Francioso, A. Forleo, S. Capone, M. Epifani, A. M. Taurino, and P. Siciliano, "Nanostructured In2O3-SnO2 sol-gel thin film as material for NO2 detection," *Sensors and Actuators B-Chemical* **114**, 646 (2006).

[153] Bender, N. Katsarakis, E. Gagaoudakis, E. Hourdakis, E. Douloufakis, V. Cimalla, and G. Kiriakidis, "Dependence of the photoreduction and oxidation

behavior of indium oxide films on substrate temperature and film thickness," *Journal of Applied Physics* **90**, 5382 (2001).

[154] T. Becker, S. Muhlberger, C. Bosch-von Braunmuhl, G. Muller, T. Ziemann, and K. V. Hechtenberg, "Air pollution monitoring using tin-oxide-based microreactor systems," *Sensors and Actuators B-Chemical* **69**, 108 (2000).

Appendix A

PROCESS FLOW FOR CANTILEVER FABRICATION

Details of device fabrication has been described in Chapter 3. This appendix gives more detail about process flow, steps required and associated parameters. First part will detail about process flow and the second part will give the description.

Step 1: MESA Isolation		
Step	Description	Process Details
1.1	SiO_2 mask deposition	Equipment: Uniaxis Plasma Enhanced Chemical Vapor Deposition (PECVD) 200 nm SiO_2 deposition (300 °C, SiH_4 = 400 sccm, N_2O = 900 sccm, 900 mtorr, RF = 25 W. Deposition rate is ~ 50 nm/min).
1.2	Lithography	Photoresist: Microposit SC1827 Spin: 3000 rpm at 750 rpm/sec for 30 secs (thickness: ~3 µm) Soft Bake: 115°C for 5 mins on hotplate (7-8 mins if put on a carrier wafer or glass slide) Exposure: λ = 405 nm, UV density = 450 mJ/cm^2 Developer: MF 319 for 1:15-2:00 min Hard Bake: 80°C for 5 mins on hotplate (before ICP etc)
1.3	SiO_2 etch in ICP	Equipment: Plasma Therm ICP with C_4F_8 Plasma Sample mount on 4" SiO_2/Si wafer with cool grease. SiO_2 etch for 1:30 mins (C_4F_8 = 15 sccm, CO_2 = 28 sccm, Ar = 5 sccm, 5 mtorr, RF1 = 40 W, RF2 = 800W, DC=158 V. Etch rate is ~ 180-200 nm/min). ▪ Etch time depends upon etch rate, 1:30 min should be sufficient to etch down 200 nm SiO_2. ▪ Clean process is run between SiO_2 etch and GaN etch
1.4	AlGaN/GaN etch in ICP	Equipment: Plasma Therm ICP with Cl_2/BCl_3 Plasma Sample mount on 4" SiO_2/Si wafer with cool grease. GaN etch for 25 secs (Cl_2 = 32 sccm, BCl_3 = 8 sccm, Ar = 5 sccm, 5 mtorr, RF1 = 70 W, RF2 = 500W, DC=225 V. Etch rate is ~ 350 nm/min). ▪ Etch time depends upon etch rate, etching down AlGaN is enough, however further GaN etching needed to ensure total mesa isolation and visibility of the etched pattern for subsequent processing, in this case 25 sec etching was performed which confirms 150 nm etching
1.5	PR removal	Clean with Microposit 1165 resist remover, acetone, methanol, and

		isopropanol. Then put in 120 °C H_2SO_4 (96%) for 3 min and/or 2 min O_2 plasma descum Equipment: Plasma Therm RIE with O_2 Plasma (50 sccm O_2, RF power 300 W)
Step 2: Top Cantilever outline		
2.1	SiO_2 mask deposition	Equipment: Uniaxis Plasma Enhanced Chemical Vapor Deposition (PECVD) 1 µm SiO_2 deposition (300 °C, SiH_4 = 400 sccm, N_2O = 900 sccm, 900 mtorr, RF = 25 W. Deposition rate is ~ 50 nm/min).
2.2	Lithography	Photoresist: Futurrex NR71-3000P Spin: 3000 rpm at 750 rpm/sec for 40 secs (thickness: ~4 µm) Soft Bake: 150°C for 5 min in oven (on glass slide or Si wafer) Exposure: λ = 365 nm, UV density = 280 mJ/cm^2, Post Exposure Bake: 100°C for 5 min in oven (on glass slide or Si wafer) Developer: RD6 for 35~45 secs
2.3	O_2 plasma descum	Equipment: Plasma Therm RIE with O_2 Plasma for 30 secs 50 sccm O_2, RF power 300 W
2.4	SiO_2 etch in ICP	Equipment: Plasma Therm ICP with C_4F_8 Plasma Sample mount on 4" SiO_2/Si wafer with cool grease. SiO_2 etch for 10 mins (C_4F_8 = 15 sccm, CO_2 = 28 sccm, Ar = 5 sccm, 5 mtorr, RF1 = 40 W, RF2 = 800W, DC=158 V. Etch rate is ~ 200 nm/min). ▪ Etch time depends upon etch rate, 10 min should be sufficient to etch down 1 µm SiO_2.
2.5	GaN etch in ICP PR removal	Equipment: Plasma Therm ICP with Cl_2/BCl_3 Plasma Sample mount on 4" SiO_2/Si wafer with cool grease. GaN etch for 7 mins (Cl_2 = 32 sccm, BCl_3 = 8 sccm, Ar = 5 sccm, 5 mtorr, RF1 = 70 W, RF2 = 500W, DC=225 V. Etch rate is ~ 350 nm/min). ▪ Etch time depends upon etch rate, with GaN etch rate of 350 nm/min, it should take 7 min to etch the remaining GaN
2.6	PR removal	Clean with Futurrex RR41 resist remover, acetone, methanol, and isopropanol. Then put in 120 °C H_2SO_4 (96%) for 3 min and/or 2 min O_2 plasma descum Equipment: Plasma Therm RIE with O_2 Plasma (50 sccm

		O_2, RF power 300 W)
2.6	Removal of SiO_2	Removal of remaining SiO_2 with Buffered Oxide Etch (BOE) for 20 mins
Step 3: Ohmic contacts		
3.1	Lithography	Same as step 2.2
3.2	Metal depostion	Equipment: CVC E-beam metal evaporator Deposition of following metal stack at pressure below 2×10^{-6} torr Titanium (Ti) : 20 nm, Aluminum (Al): 100 nm, Titanium (Ti): 45 nm, Gold (Au): 55nm
3.3	Metal liftoff	Metal liftoff in warm (80 ºC) RR41 resist remover and rubbing by RR41 soaked foam swab; rinse in warm acetone; squirted at by acetone, methanol, isopropanol; blow dried by N_2
3.4	RTP	Equipment: SSI Rapid Thermal Annealer (RTP) Purge: 8 SLPM N_2 Anneal (no N_2): ramp to 525 ºC at 55 ºC/sec, hold 20 sec, ramp to 825 ºC at 60 ºuntil Ramp down: 8 SLPM N_2 until 250 ºC Overshoot: 25 ºC, Limit: 900 ºC
Step 4: Schottky contacts		
4.1	Lithography	Same as step 2.3
4.2	Metal deposition	Equipment: CVC E-beam metal evaporator Deposition of following metal stack at pressure below 2×10^{-6} torr Nickel (Ni) : 50 nm Gold (Au): 200 nm
4.3	Metal liftoff	Same as step 3.3
Step 5: Probe contact pads		
5.1	Lithography	Same as step 2.3
5.2	O_2 plasma descum	Equipment: Plasma Therm RIE with O_2 Plasma for 30 secs 50 sccm O_2, RF power 300 W
5.3	Metal deposition	Equipment: CVC E-beam metal evaporator Deposition of following metal stack at pressure below 2×10^{-6} torr Titanium (Ti): 20 nm

		Gold (Au): 250 nm
5.3	Metal liftoff	Same as step 3.3
Step 6: Through wafer Si etch from backside		
6.1	Thick SiO_2 mask deposition (backside)	Equipment: Uniaxis Plasma Enhanced Chemical Vapor Deposition (PECVD) 10 µm SiO_2 deposition (300 °C, SiH_4 = 400 sccm, N_2O = 900 sccm, 900 mtorr, RF = 25 W. Deposition rate is ~ 50 nm/min).
6.2	Lithography (backside)	Photoresist: Futurrex NR71-3000P Spin: 3000 rpm at 1000 rpm/sec for 40 secs (thickness: ~4 µm) Soft Bake: 150°C for 1 min on hotplate Backside alignment Same as step 2.1
6.3	SiO_2 wet etch (backside)	SiO_2 etch with Buffered Oxide Etch (BOE) for 25 mins
6.4	Through wafer Si etch (backside)	Equipment: STS ICP (Bosch Process) Sample mount on 4" SiO_2/Si wafer with cool grease. Carrier wafer should have at least 9 µm PECVD oxide. Thermally grown oxide can be of lesser thickness. Si etch for as many cycles as needed, typically 1200 cycles for 625 µm Si substrate. Etch cycle: 10 sec (SF_6 = 130 sccm, O_2 = 13 sccm, 94 mtorr, RF1 = 10 W, RF2 = 600W, Passivation cycle: 8 sec (C_4F_8 = 100 sccm, 94 mtorr, RF1 = 0 W, RF2 = 600W.